Doctoral Thesis

Analyses on Nonlinear Dynamics with Multiple Time-Scales in the Brain

(脳における多重時間スケールを有する
非線形ダイナミクスの解析)

Takumi Sase
(佐瀬 巧)

Supervisor: Professor Kazuyuki Aihara (合原 一幸 教授)

December 4, 2015

Department of Mathematical Informatics
Graduate School of Information Science and Technology
the University of Tokyo

To my beloved families

Abstract

We analyzed nonlinear dynamics with the multiple time-scales structure emergent from the brain, and mainly focused on the three distinctive time-scales: deterministic slow, deterministic fast, and stochastic fast oscillations, with the aim at understanding the dynamics generating macroscopic oscillatory phenomena, often observed as electroencephalographic (EEG) signals—which reflect huge information of cell assemblies in the brain and accordingly would involve higher brain functions such as consciousness.

First, we developed a novel nonlinear time series analysis method called time series dimension (TSD), which was derived from the conventional fractal dimension through a key approximation. Owing to this approximation, the TSD was a function of the level of dynamical noise behind time series, where the dynamical noise was defined in the sense of the Gaussian white noise so that this noise was the origin of the stochastic fast oscillations. Based on such a functional TSD, we succeeded in detecting the level of dynamical noise included in unknown dynamics behind time series, so as to analyze any signal composed of both the deterministic oscillations and the stochastic fast oscillations. Via applying the TSD to EEG signals, we revealed that the visual inputs can control the level of dynamical noise in the frontal lobe; this result suggests that temporal changes of the extracted dynamical noise level contribute to characterizing nonlinear oscillatory phenomena.

Second, we developed an extended discrete-time neural network model, comprising excitatory and inhibitory stochastic neurons with dynamic synapses, so as to analyze signals composed of the deterministic slow oscillations and the deterministic fast oscillations. Owing to the mean field approximation, a set of variables representing neurons was converted to a macroscopic variable resembling an EEG signal, and furthermore the stochastic model was transformed into a discrete-time dynamical system. Via the bifurcation analysis, we revealed that the interactions between the above two different networks can generate the two subtypes of phase-amplitude cross-frequency coupling phenomena, which were separated by the cyclic saddle-node bifurcation of a one-dimensional torus in a map, named MT1SNC bifurcation; this result suggests that the underlying dynamics of cross-frequency coupling phenomena effectively switches between the two submodes, depending on external environmental changes.

We believe that the aforementioned two mathematical analyses, namely nonlinear time series analysis and bifurcation analysis will help us approach the comprehensive elucidation of complex dynamics in the brain.

Keywords: deterministic and stochastic oscillations, slow and fast oscillations, EEG, nonlinear time series analysis, mathematical modelling, bifurcation analysis, dynamical noise level, time series dimension (TSD), discrete-time neural network model, mean field approximation, cyclic saddle-node bifurcation of one-dimensional torus in map (MT1SNC), phase-amplitude cross-frequency coupling

Contents

Chapter 1

Introduction

1.1 Motivation

Our most interest—which would be among many neuroscientists, and should be solved urgently—is to know the property of 'macroscopic' neural oscillations, occurring in huge complex neural networks in the brain. Fortunately, we can now easily observe or measure one realization of the macroscopic oscillations, as an electroencephalographic (EEG) signal with the high temporal-resolution. Analyzing the EEG signals may help us know, e.g. "what the consciousness is" [2]; this theme is a big problem for us beyond this thesis. Actually, many neuroscientists have believed that, the EEG signals reflect key properties concerned with consciousness, because the signals are formed from a collection of cell assemblies (neural networks) such that the signals involve macroscopic rich information. Furthermore, the EEG signals result from the interaction among various types of neurons; this interaction may be one origin of the process of consciousness generation. Thus, we have suggested that only one neuron does not include the component of consciousness, but neural networks involve it.

To address how to reveal higher brain functions such as consciousness, probably contained in EEG signals, we firstly have to analyze the EEG signals effectively, by using the time series analysis. The waveform of an EEG signal is characterized by oscillations, so that until now almost neuroscientists especially have focused on the frequency and the phase, both of which directly connect to the form of oscillations. This 'linear' time series analysis, based on the Fourier series, seems to be natural to analyze oscillations, but misses 'nonlinearity'.

In particular from the viewpoint of nonlinearity, a band-pass filter is a good example breaking dynamics underlying oscillations, although almost neuroscientists have used it as preprocessing to extract well-known delta, theta, alpha, beta, or gamma waves, because each of them has frequency-specific functional roles in the brain [3]. For several decades, the linear time series analysis has revealed little by little, that how the external information is coded in the frequency and the phase in EEG signals and accordingly, discussions given by this analysis naturally have been concerned with synchronized phenomena [4]; this

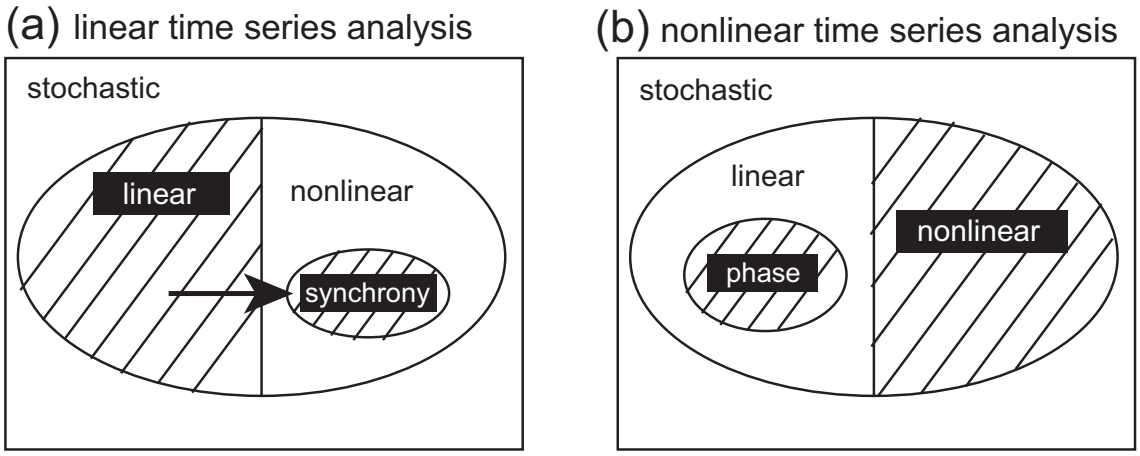

Figure 1.1. Relationship between the linear/nonlinear time series analysis and the extractable phenomena. (a) A case of the linear time series analysis. This analysis can extract a universal set of linear phenomena associated with the frequency or phase, but can view only synchronized phenomena through phases, where this phenomenon is a subset of nonlinear phenomena. (b) A case of the nonlinear time series analysis. This analysis can extract a universal set of nonlinear phenomena, but with the phase, which is a subset of linear phenomena, because even if a time series is embedded on a high-dimensional state space, the state space still involves phase information.

conventional linear analysis seems to be awkward because synchronization is actually a nonlinear phenomenon. If original EEG signals are separated into several frequency bands, nonlinearity will be also reduced, so that a question, whether the linear time series analysis can approach nonlinear dynamics which would reflect consciousness, occurs [Fig. 1.1(a)]. It seems that this conventional analysis can view only synchronization, not other nonlinear phenomena such as chaos, i.e., this approach implicitly has assumed that, consciousness is involved in synchronized phenomena. Perhaps this assumption has been out of mind for neuroscientists, but one should note that the linear time series analysis would be far from the elucidation of consciousness, because synchronization is very small subset of nonlinear phenomena [see Fig. 1.1(a)].

Besides there exists another linear aspect to analyze EEG signals, that is the averaging filter over multiple trials; this linear time series analysis aims at extracting very miniature components, called evoked potentials (EPs), in common contained in multiple EEG signals [5]. Typically EPs occur at the same timing over multiple trials, so that the averaging filter works well, but at the same time, this filter clearly reduces nonlinearity by considering it as background noise as well as the aforementioned band-pass filter, and therefore this type of linear time series analyses also views only synchronized phenomena; note that this synchrony comes from one electrode on the scalp, whereas the aforementioned synchrony comes from between more than two electrodes. Thus, the linear time series analysis, which we explained two cases, is restricted to extractions of only synchronized phenomena [Fig.

1.1(a)], so that a new type of time series analyses will be needed to bring us new insights in the neuroscience field and to approach the answer to a question: what the consciousness is.

The 'nonlinear' time series analysis based on Takens' embedding theorem [6] has been dramatically studied, especially in physics field, and has a possibility to answer the above question because this type of time series analyses can reconstruct high-dimensional nonlinear dynamics only from time series. This analysis assumes that, a nonlinear dynamics exists behind a time series, so that purely stochastic time series such as colored noise (fractional Brownian motions) are out of the analysis [see Fig. 1.1(b)], but our interest in this thesis is of oscillatory phenomena, consisting of a variety of nonlinearity, and therefore such an assumption can be ignored. Here noise, in the sense of the Gaussian white noise, is usually contained in a time series even if its origin is a deterministic dynamical system, but the amount of actual noise is relatively less than deterministic components so that the reconstruction of dynamics can be achieved. In addition, the reconstructed dynamics includes rich information concerned with many nonlinear phenomena such as chaos and off course reflects synchronized phenomena [see Fig. 1.1(b)], and therefore this dynamics would also involves consciousness. However, commonly the dynamics is on a very-high-dimensional state space, so that it seems that it is difficult to extract brain functions such as consciousness. Actually, the Lyapunov exponents [7], the correlation dimension [8], or the causality [9] can be estimated from the reconstructed dynamics, but still these several quantities have not directly been connected to brain functions.

To overcome this issue, recurrence plots (RPs) [10] have been developed to visualize high-dimensional attractors, where a two-dimensional plane we can easily observe is produced. Although RPs are only 2-dimensional and composed of a set of only binaries, surprisingly almost information are included in RPs [11], so that brain functions would be also reflected in a pattern composed of black (one) and white (zero) colors. This pattern may characterize each of brain functions, but this approach has not been applied to EEG signals well, because RPs effectively work if and only if the reconstructed dynamics and its original dynamics are one-to-one. Clearly methods using RPs make the nonlinear time series analysis easier for neuroscientists, than methods using other techniques, but the existence of noise, especially dynamical noise is a big problem to reconstructing dynamics, where noise, hereinafter, is naturally supposed to the Gaussian white noise.

Commonly, noise is divided into two types from the viewpoint of dynamical systems, namely observational noise and dynamical noise; the former is added to signals observed from devices so that this noise does not affect a trajectory moving on an attractor behind the signals; the latter affects system's dynamics directly so that the time evolution of the system depends not only on a dynamical rule but also on dynamical noise. In the real world, both types of noise would influence systems, and therefore the aforementioned nonlinear time series analysis may not be suitable for such systems, called stochastic dynamical systems. If a trajectory changes with noise, nonlinear quantities such as the Lyapunov

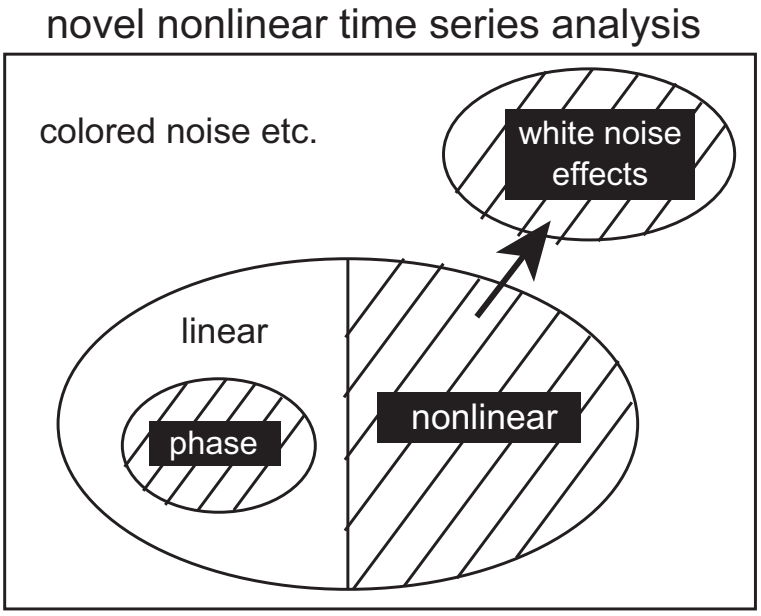

Figure 1.2. Relationship between a novel nonlinear time series analysis and the extractable phenomena. This analysis is an extended version of the conventional nonlinear time series analysis so that it can stll extract a universal set of nonlinear phenomena and a subset of linear phenomena, namely phase. In addition to such sets, the novel analysis can extract a subset of stochastic phenomena, called Gaussian white noise (dynamical noise) effects, where this noise drives variables constituting nonlinear dynamics so that the trajectory can change stochastically.

exponents cannot be estimated accurately. Off course we can assume that the level of dynamical noise is relatively less than that of deterministic components so that we can reconstruct dynamics, but in the brain, neurons themselves would generate noise, which will play a role of dynamical noise, and furthermore the resulting noise level possibly be very high so that the temporal evolution of EEG dynamics is dominantly stochastic. Thus, effective novel methods for analyzing dynamical noise behind time series should be developed urgently, because almost real-world systems are influenced by dynamical noise as mentioned above [see Fig. 1.2].

Actually, only the nonlinear time series analysis, which is one technology of our major called mathematical engineering, is not enough to understand nonlinear dynamics underlying EEG signals, because this analysis cannot reconstruct a mathematical model generating a phenomenon, rather, it mainly aims at characterizing unknown dynamics (models). Fortunately, another complementary technology is involved in mathematical engineering, namely mathematical modelling, which is to mathematically reconstruct dynamical models behind time series [Fig. 1.3], herein EEG signals. Perhaps, one may think that the combination between the nonlinear time series analysis and the mathematical modelling is enough to research EEG dynamics, i.e. experimental knowledge are not needed well,

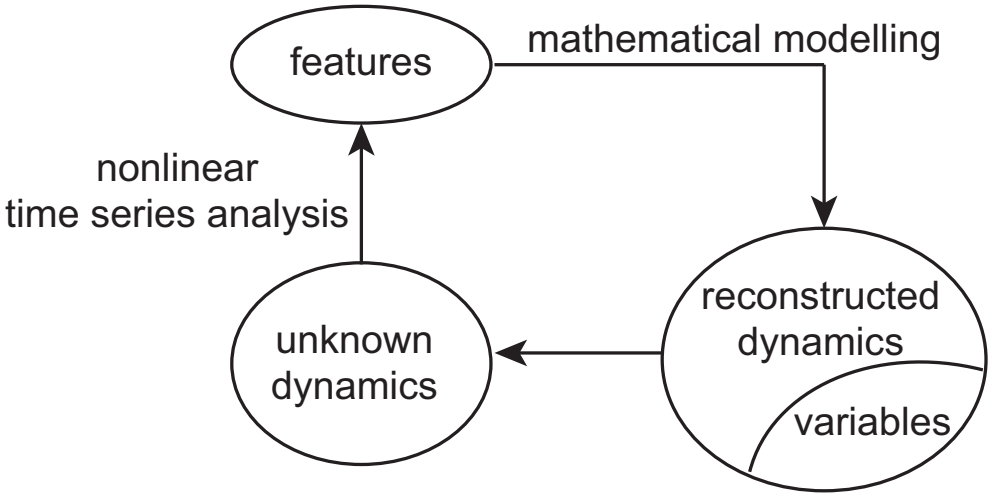

Figure 1.3. A complementary study using the following two technologies: (1) nonlinear time series analysis and (2) mathematical modelling. Technology (1) is to extract features characterizing 'unknown' dynamics behind time series, whereas technology (2) is to 'reconstruct' dynamics using the prior knowledge (features), where note that the reconstructed dynamics includes variables associated with the features. Until the properties of the variables and those of the features will be one-to-one, a cycle consisting of technologies (1) and (2) is repeated along the three arrows so that the reconstructed model can predict unknown phenomena perfectly.

because the former technology, nonlinear time series analysis, can characterize unknown models behind time series and therefore, someday it will be able to extract components of consciousness, while the latter technology, mathematical modelling, can reconstruct the dynamics—imagine here that a 'perfect' model is provided, i.e. a phenomenon originating from the model and the corresponding observed phenomenon are one-to-one. Based on this reconstruction, we can clearly predict various unknown phenomena by effectively changing parameters included in the model and accordingly, someday variables concerned with consciousness will be able to be included in the model depending on the prior knowledge, that are components of consciousness extracted by the nonlinear time series analysis described above [see Fig. 1.3].

Therefore, it seems that because the aforementioned combinational methodology is closed in the field of mathematical engineering, this field does not need any feedback from EEG experimental knowledge, as long as the model is created once according to a prior experimental result. However, the model as mentioned above has been assumed to be pure, but actual models include some kinds of errors arising from discrepancies between the models and the corresponding actual dynamics so that a perfect prediction using such models cannot be achieved. Thus, interactive studies between mathematical engineers and experimental neuroscientists cannot be avoided, and hence the following four steps will be mainly recommended [see Fig. 1.4]:

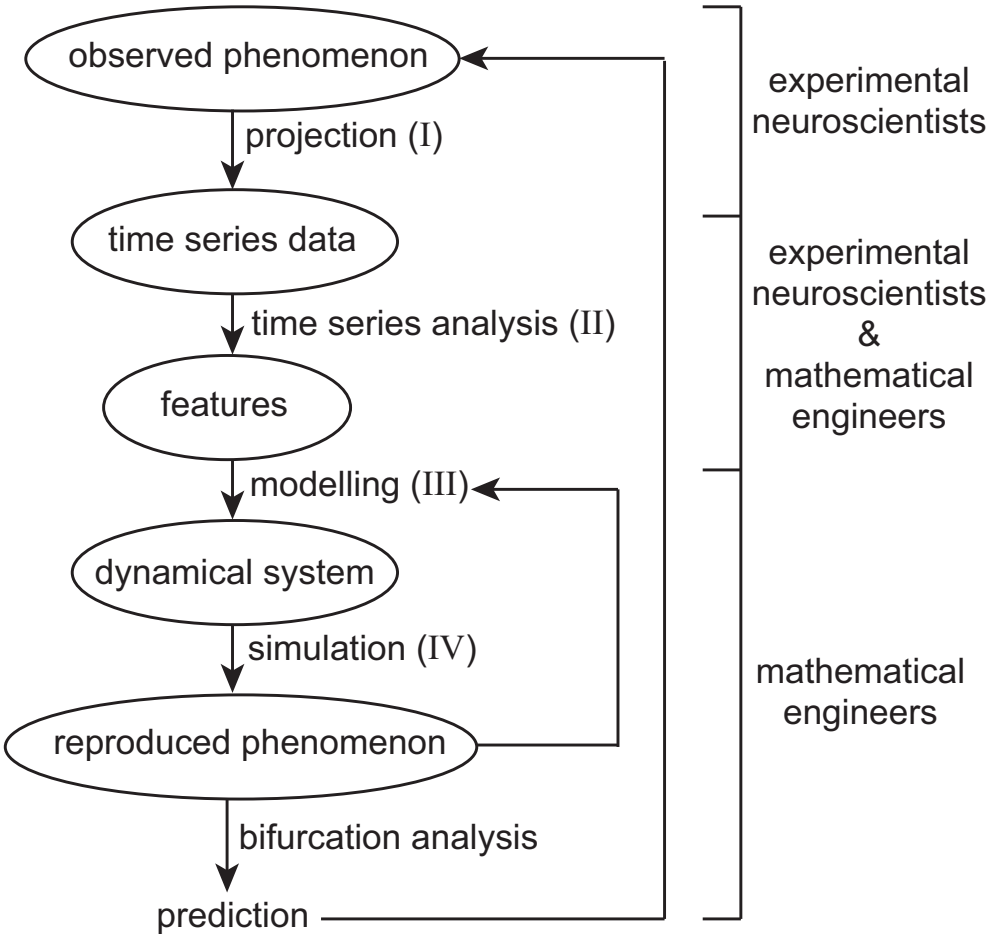

Figure 1.4. A flow from an observation to a prediction. The flow consists of the following four steps: (1) projection of the observation on time series data, (2) time series analysis for extracting features, (3) modelling a dynamical system based on the features, and (4) simulation for validation whether the observed phenomenon and reproduced one are one-to-one. After the validation at step (4) finishes, the bifurcation analysis may be performed to predict an unobserved phenomenon, and accordingly another validation whether such a predicted phenomenon can be observed in the real system is conducted. The study consisting of this flow will be achieved by a collaboration between experimental scientists and mathematical engineers.

(I) First, an experimenter observes a phenomenon as a time series, under a certain condition by using a controlled device, where a high-dimensional dynamics behind the phenomenon is converted to a one-dimensional signal, and furthermore the signal is formed as a time series with a certain sampling time. Perhaps, this time series may be a multivariate time series, especially for EEG recordings.
(II) Second, the experimenter characterizes the phenomenon with quantities such as frequencies characterizing EEG signals, where skills concerned with the time series analysis would be needed even for the experimenter, because if he has several techniques using not only the linear time series analysis but also the nonlinear time series analysis, the phenomenon can be quantified by many kinds of features comprising a variety of aspects, namely linearity and nonlinearity. These aspects provide us, for example not only the fundamental frequency, the power, or the phase locking value between two EEG signals, but also the Lyapunov exponents or the correlation dimension connected to chaos, or the causality between two signals. Furthermore, recently information flow using the technique called transfer entropy (TE) [12] has been becoming a key element little by little—this new type of techniques, TE, is actually out of linear or nonlinear time series analyses, because the TE is based on the Shannon entropy, the field of the information theory, not the time series analysis, but this new technology has been gradually approaching the time series analysis because information flow is similar to the causality; in addition, the quantification of information flow among several brain regions would be a remarkable feature towards modelling [13].
(III) Third, a modeler gets the above experimental condition including some parameters and a set of features characterized by the experimenter, where these parameters are used to model, but note that the experimenter cannot observe overall parameters such as the coupling strength between two EEG signals. Therefore, a given set of parameters would be a very small subset in a universal parameter set, controlling the phenomenon perfectly. Based on given parameters (condition), the modeler creates a model approximating the observed dynamics, where the model is commonly composed of some variables, parameters, and functions connecting the variables; such functions are either linear or nonlinear. Perhaps, a known model may be used for modelling in some situations, where only parameters will be tuned, but such a model would not be able to reproduce the desired phenomenon because the known model had been before used for reproducing another phenomenon.
(IV) Fourth, the modeler simulates the model on a computer and observes a time series, not a continuous signal because in the numerical simulation, differential equations are discretized for example by the Runge-Kutta method with a certain small sampling time so that we can get observation values with high accuracy, but a given observation value actually includes an error from a real value and furthermore, along the time evolution the error will expand—we have implicitly assumed here that modelling is achieved by differential equations, namely flow, because EEG signals we are interested in might be continuous signals. Based on the simulation, the modeler confirms whether a phenomenon emergent

from the model is qualitatively consistent with the actual phenomenon, by adapting features characterized by the experimenter. If these phenomena given by the experimenter and by the modeler are consistent, an integrated research—in which actual phenomena can be explained by mathematics—will be achieved. However, only one iteration from steps (I) to (IV) would not enough to finish this project, where the following two causes might hide: (i) validity of features characterizing phenomena and (ii) validity of models.
(i) Regarding the first cause, many experimental neuroscientists aim at finding new unobserved phenomena, so that the experimental skills are mainly needed rather than time series analysis techniques, and thus overcoming this cause seems to be very difficult, especially for the nonlinear time series analysis, which possibly be out of their minds. Fortunately, they are interested in the linear time series analysis, namely the frequency and the phase of EEG signals because it has been believed that the frequency characterizing e.g. alpha waves concerns brain functions, while the phase relates to information coding in the brain. Therefore, interactions between mathematical engineers and experimental neuroscientists are strongly needed even for a stage of the extraction of features characterizing phenomena, namely at step (II).
(ii) Regarding the second cause, recently a tendency can be seen, that is, models are created abstractly so that the bifurcation analysis—which is to reveal how a phenomenon changes to another one—can be easily conducted, and therefore if the bifurcation type between several phenomena becomes clear and if the control parameter inducing the bifurcation is identified, then we can facilitate or prevent to bifurcate systems. Thus, abstract models are useful to analyze the models themselves in detail, but some assumptions are commonly included in the models, for example concerned with coupling connections among neurons, where uniform connections have been often used recently, mainly towards the mean field theory. Thus, a probability that such abstract models can reproduce phenomena observed in experiment is very low, so that we have to turn from step (IV) to (III), and another model should be created towards an achievement of certain modelling.

Then, as well as the time series analysis, modelling also includes a problem whether the model is linear or nonlinear, where surprisingly even a 'perfect' linear model, namely the harmonic oscillator system can exhibit a waveform such as an EEG signal, owing to the effect of noise (Gaussian white noise). Note, however, that generating the waveform similar to real-world phenomena is not of our main focus, because even if such a 'linear' waveform can be given by a simulation, the underlying nonlinear phenomena such as chaos or even synchronization cannot be revealed. Nevertheless, several neuroscientists, especially experimental neuroscientists tend to not care how to model, i.e. they only care the similarity between the waveforms generated from a model and from the corresponding real phenomenon. Actually this notion is considerable from the viewpoint of the following proposition: "any phenomenon can be explained by mathematics", but only this thought might be very cheap for mathematical engineers, who aim at understanding the underlying phenomena of given time series through the bifurcation analysis in addition to the above

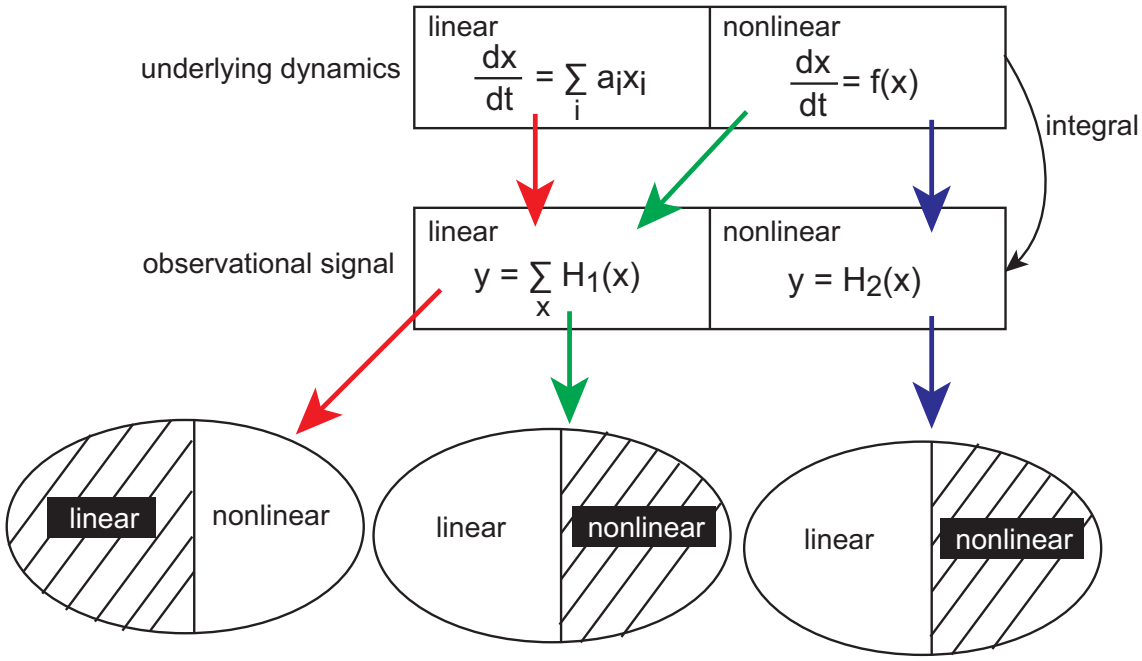

Figure 1.5. Relationship between modelling and the reproducible phenomena. Modelling includes the following two layers: (1) modelling an observational signal and (2) modelling the underlying dynamics, where each layer is constituted by either linearity or nonlinearity. The properties of linearity (nonlinearity) arising from layers (1) and (2) differ with each other and are connected via the integral. Towards modelling the following three cases are considerable: (a) If both layers are linear (red arrows), the reproducible phenomena show also linearity as a form of the harmonic oscillator system. (b) If layer (1) is linear but layer (2) is nonlinear (green arrows), the reproducible phenomena show nonlinearity owing to layer (2), where one can suppose that x and $f(x)$ are a phase and the Kuramoto model, respectively, while $H_1(x)$ is $\sin(x)$ so that this modelling exhibits an oscillator-based EEG model. (c) If both layers are nonlinear (blue arrows), the reproducible phenomena show also nonlinearity. Perhaps this case is more suitable to model than case (b) because modelling layer (1) in case (c) is constituted by only one element.

proposition. Therefore models should be created based on the prior knowledge given by real-world dynamics.

To return the topic that modelling also includes a problem whether a model is linear or nonlinear as well as a problem on the time series analysis, but modelling is more sensitive to linearity than the time series analysis, because if a 'linear' model is created, a phenomenon emergent from the model becomes also linear [see the red arrows in Fig. 1.5], whereas in the filed of the time series analysis, synchronized phenomena can be observed even if the analysis is perfectly linear [see Fig. 1.1(a)]. Furthermore, we should note that linearity arising from modelling is actually different from that arising from the time series analysis, because the former is a case on a differential equation, where a linear model means that the dynamical rule describing a dynamics is linear, but the latter is a case on a signal observed from a device (observation function) converting high-dimensional variables to a

one-dimensional variable. Thus, we have to clearly understand such a discrepancy come from between the modelling and the time series analysis, to precisely discuss the necessity of nonlinearity based on both the modelling and the time series analysis; otherwise, perhaps one may discuss the nonlinearity of them on a common level, although nonlinearity arising from modelling occurs on a dynamical rule (differential equation), whereas that arising from the time series analysis occurs on the integral of the dynamical rule [see Fig. 1.5].

Now we focus on the modelling in terms of nonlinearity, but especially towards EEG dynamics modelling, a middle level actually exists, where this level of modelling is composed of both aspects of linearity and nonlinearity [see the green arrows in Fig. 1.5]. First, we shall introduce an example model, where an EEG signal is represented by a collection of many EEG oscillators such as delta, theta, alpha, beta, and gamma oscillators, as components of the EEG signal, and furthermore each EEG oscillator is described as the Kuramoto model [15]. Thus, this EEG model comprises both components of linearity and nonlinearity, i.e., the following two assumptions exist: one is that the model can be separated linearly into several frequency oscillators; another is that each oscillator is the Kuramoto phase oscillator. Here note that the Kuramoto model involves the Hopf bifurcation originating from nonlinearity of the coupling term so that there exist the following two dynamically distinctive regimes: one regime is the non-synchronized state, where the phases among respective oscillators are incoherent; another regime is the synchronized state, where the phases are definitely coherent. Because it has been strongly believed that an EEG signal might possess frequency-specific brain functions and that the amplitude of the signal would reflect the synchronization among EEG oscillators, the aforementioned two assumptions may be validated towards modelling. Furthermore, it is well known that modified versions [16, 17] of the Kuramoto model show a variety of nonlinear phenomena including chaos. However, the EEG model based on the Kuramoto model has explicitly comprised a concept of oscillations, as an aggregation of the frequencies so that a generation mechanism of such oscillations cannot be revealed.

Off course, we can model an EEG signal as a form of a more microscopic level rather than EEG oscillators, namely in terms of local field potentials (LFPs), where an LFP has been assumed to be the Kuramoto phase oscillator. However, the model based on LFP oscillators might be very similar to the above EEG model so that a problem how the oscillations appear still remains to be explored.

Besides, a phenomenological EEG model has been proposed, called neural mass model (NMM) [18] which is a 'perfect' nonlinear model [see the blue arrows in Fig. 1.5], that is, it has not been assumed that an EEG signal is a collection of EEG/LFP oscillators and furthermore, the dynamics of the NMM is described by several nonlinear terms so that we can answer the above problem: how the oscillations appear. In fact, the NMM can show a variety of oscillatory phenomena including alpha waves, where the mechanism of such phenomena indeed underlies the limit cycle attractor, generated due to nonlinearity involved in the NMM. By tuning parameters effectively, a diverse limit cycle oscillator with

the various velocities emerges so that key parameters switching among several frequency bands can be identified. This NMM or the modified NMMs [19, 20] have been widely used in the neuroscience community because the dynamics within the models have been naturally expressed from the viewpoint of actual EEG dynamics. However, such models are very abstract, and therefore it seems to us that the process of consciousness generation we are strongly interested in, will not be revealed.

Although the NMM is a perfect nonlinear model in terms of both descriptions for the underlying dynamics and for its observational process [see Fig. 1.5], expressing the components of consciousness as a variable seems to be very difficult, and therefore another essential idea should be introduced. Herein we have to mention that the state of one neuron is not involved in the NMM as a variable, whereas a cell assembly—an aggregation of the neurons—is included in it as a variable. Thus, because the model has been created from the viewpoint of the cell assembly, not the neurons, their interactions (between cell assemblies and neurons) cannot be appeared as the resulting phenomena on the model. Here, a remarkable point exists, that is, the interactions between a whole and its elements; such interactions always can occur in the real-world systems, e.g. in the humans 'system' interacting in a room, in which each human interacts with other humans by speaking or acting so that the 'driven' human behaves according to an instruction of the 'driving' human (a case of an interaction from elements to a whole) and in contrast, the behavior of each human depends not only on his own mind but also on the atmosphere of the room, generated from the moods originating from all humans' minds (a case of an interaction from a whole to its elements). This analogical example can be directly applied to the interaction between a cell assembly and each neuron, and consequently we shall put forward a hypothesis that such interactions, especially from a whole to its elements, can generate consciousness [see Fig. 1.6] [21]. Hence, the use of the mean field approximation systematized in the field called statistical mechanics, which can convert a set of microscopic variables representing neurons to only one macroscopic variable representing an EEG or LFP signal, will be a straitforward way to modelling .

1.2 Purpose

As mentioned above, the following two complementary technologies might be needed from the viewpoint of the field of mathematical engineering, namely (1) nonlinear time series analysis and (2) mathematical modelling, to analyze nonlinear dynamics generating the macroscopic oscillations such as EEG signals. In addition, the process of consciousness generation still remains to be explored. Therefore, hereafter we aim at developing the following two new tools associated with technologies (1) and (2), to approach the elucidation of consciousness:

(1) Regarding the nonlinear time series analysis, a novel tool for analyzing the dynamical noise, especially including in EEG dynamics and originating from stochastic neurons, will

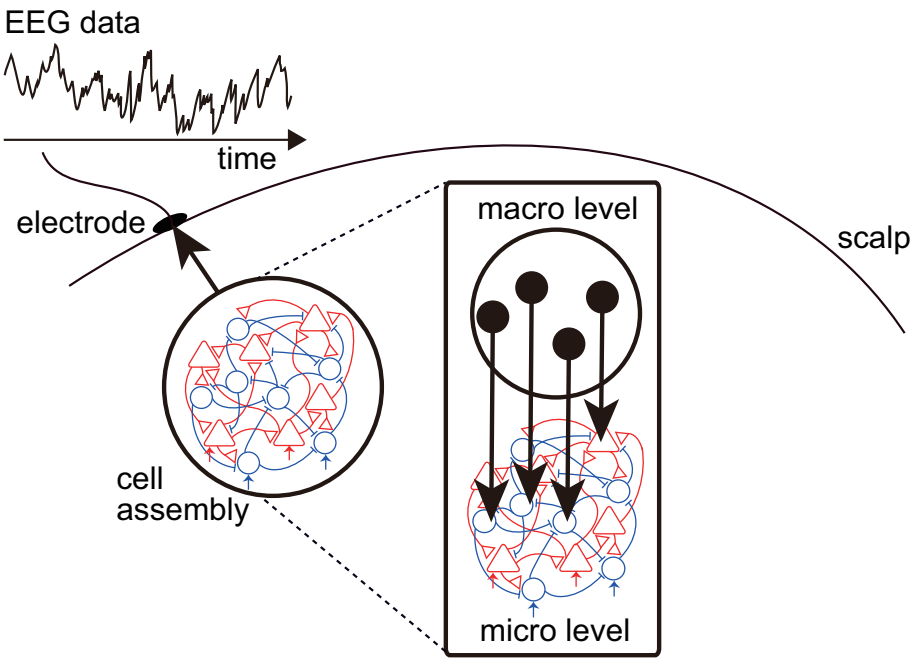

Figure 1.6. A hypothesis that the interaction between neurons (micro level) and EEG dynamics (macro level) generates higher brain functions such as consciousness and that the feedback from the macro to micro levels strongly connects to the process of consciousness generation.

be introduced in Chapter 2.
(2) Regarding the mathematical modelling, an extended stochastic neural network model will be introduced in Chapter 3, to understand the effect of the mean field approximation on the model; this model is a more realistic neural network model than the previous version [22] so that the model can reproduce a variety of macroscopic phenomena observed in EEG signals such as cross-frequency coupling phenomena, connecting between the macroscopic oscillations (EEG signals) and the microscopic neuronal firing [see the summarize of the purpose in Fig. 1.7].

Furthermore, we have to say that many kinds of nonlinear dynamics arising from this thesis will be analyzed in terms of oscillatory phenomena; this means that such dynamics comprise the multiple time-scales, from slow to fast oscillations and therefore, this study views the various nonlinear phenomena from the linearity [see Fig. 1.8]. Thus, the study sharing this viewpoint might play a key role that, someday many neuroscientists are going to be attracted to the world of the underlying nonlinear dynamics generating e.g. chaos.

1.3 Definitions of oscillations

Here we define oscillations in the sense of stochastic dynamical systems, so that oscillations emergent from the systems can be widely divided into the following two distinctive classes: (I) deterministic oscillations and (II) stochastic oscillations, both of which are

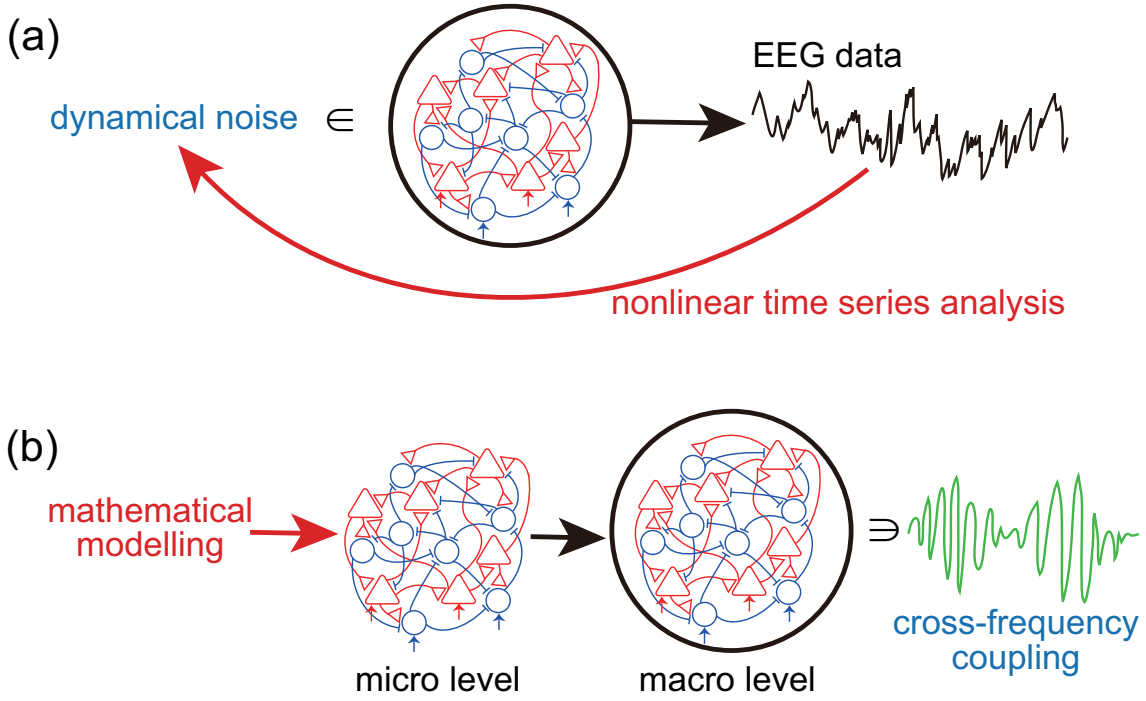

Figure 1.7. Two representative purposes arising from Chapter 2 for (a) and from Chapter 3 for (b). (a) The aim is to extract dynamical noise, driving variables constituting nonlinear dynamics, from EEG data, where a novel nonlinear time series analysis method is presented. (b) The aim is to understand the underlying dynamics of cross-frequency coupling phenomena, where an extended neural network model is presented, and furthermore the model is converted to a macroscopic model through the mean field approximation; this conversion from the micro to macro levels is possibly associated with the process of consciousness generation.

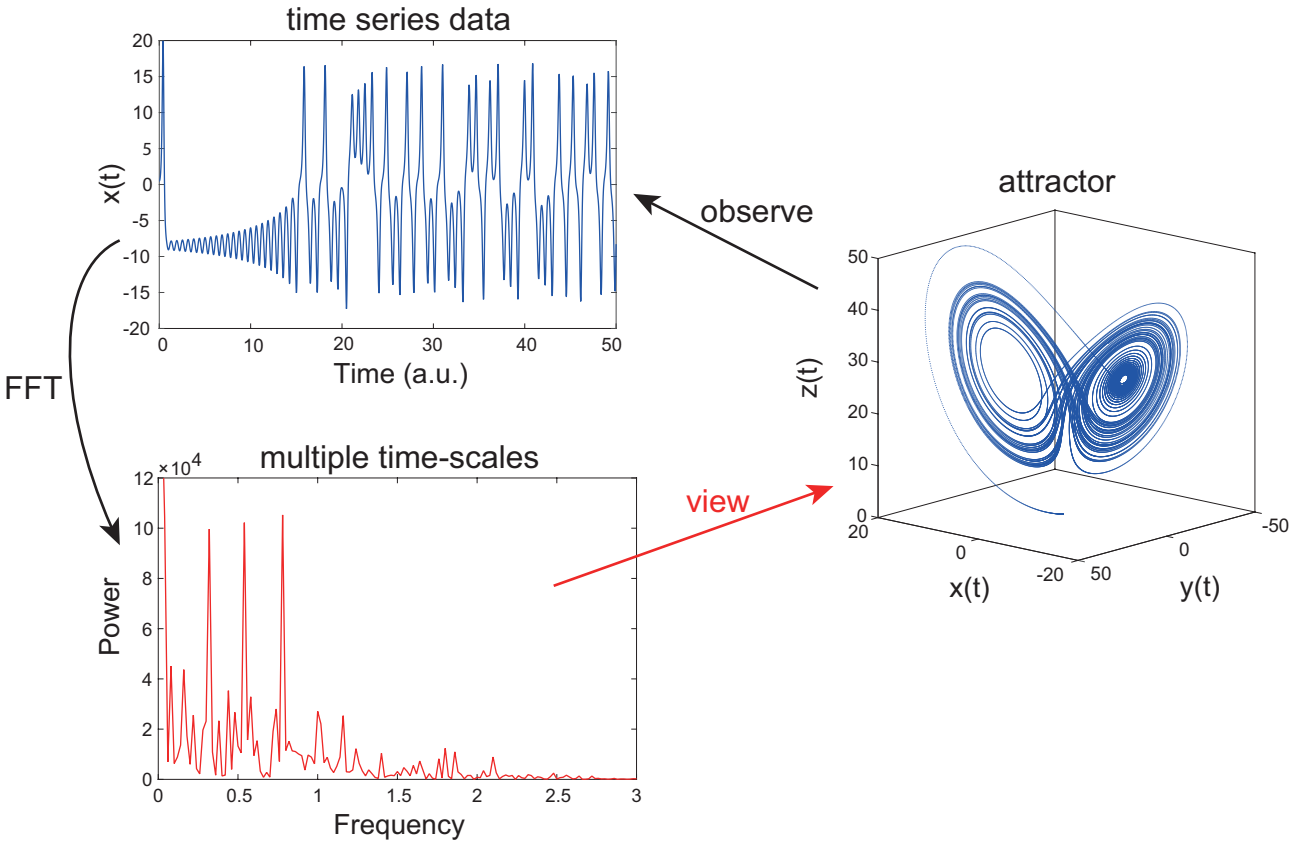

Figure 1.8. How to approach elucidating nonlinear dynamics in the brain. A variety of oscillatory phenomena is essential to form brain dynamics, so that the dynamics should be analyzed from the viewpoint of multiple time-scales the brain involves, i.e., the nonlinear dynamics generating oscillations is analyzed in terms of not only nonlinearity but also the frequency (linearity), ranged from the slow to fast oscillations and originating from the deterministic or stochastic process.

qualitatively different with each other, because class (I) originates from the drift term on systems, whereas class (II) originates from the diffusion term (dynamical noise) on systems. Furthermore, we define these classes such that the union between each class is equivalent to the original oscillations on a certain domain. Note that we do not care the existence of observational noise towards defining oscillations, because this kind of noise is out of the description of dynamics and only depends on the observational environment, mainly concerned with the property of observational devices.

We shall define the velocity of each class of oscillations relatively, in terms of stochastic dynamical systems so that the qualitative difference between classes (I) and (II) becomes clearly; the construction of this definition will be helpful to strictly define classes (I) and (II). To define the velocity, the following notion is needed, that is, because the diffusion term is generally expressed as the meaning of the Gaussian white noise, oscillations observed via the integrals of stochastic dynamical systems also reflect the property of the Gaussian white noise, more precisely that of the Wiener process, which is the integral of the Gaussian white noise. Thus, we define that the velocity of the stochastic oscillation is faster than that of the deterministic oscillation, because actually one realization of the Wiener process shows a very fast oscillation due to its definition. Off course, the drift term can make an oscillation faster, but even if the velocity of the oscillation becomes very fast owing to the formulation of the drift term, such an oscillation still contains more fast oscillatory components originating from the diffusion term, because one realization of the Wiener process contains the 'infinite' frequency. If and only if oscillatory components originating from the drift term include the infinite frequency, the velocity of the deterministic oscillation will be equivalent to that of the stochastic oscillation, but such a deterministic oscillation should be regarded as a stochastic oscillation, from the viewpoint of mathematical modelling.

Throughout this thesis, we use the term, "stochastic fast oscillation" instead of stochastic oscillation, to express more explicitly the property of this class of oscillations.

Finally, we shall introduce the definition associated with the following two subclasses: (i) deterministic slow oscillations and (ii) deterministic fast oscillations so that the union between these oscillations is equivalent to the original deterministic oscillation on a certain domain. As a simple case, we start to consider the oscillation observed from e.g. the coupled Stuart-Landau oscillators system generating the two-dimensional torus attractor—it has been assumed that this system is not affected by dynamical noise at all because now we are interested in pure deterministic oscillations. Clearly, such an oscillation involves the two representative frequency components so that it can be divided into the two subclasses (i) and (ii) on the frequency domain.

The objective towards analyses on Chapters 2 and 3 has been summarized in Fig. 1.9. In Chapter 2, signals composes of the deterministic oscillations (class (I)) and the stochastic fast oscillations (class (II)) will be analyzed, where class (I) is not divided into subclasses, i.e., the velocity of the deterministic oscillation is out of the purpose of Chapter 2. In

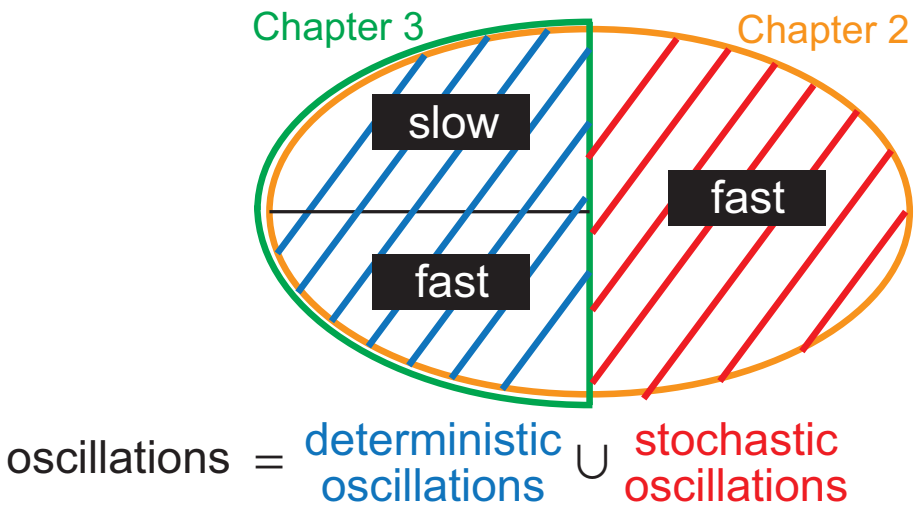

Figure 1.9. A set of oscillations is divided into the following two subsets: (1) deterministic oscillations and (2) stochastic oscillations in terms of stochastic dynamical systems. Subset (1) can be further divided into two sub-subsets: (i) deterministic slow oscillations and (ii) deterministic fast oscillations in terms of the frequency domain. In addition, subset (2) shows only the fast oscillation due to the Gaussian white noise (dynamical noise), so that we call this subset as stochastic fast oscillations. In Chapter 2, signals composed of subsets (1) and (2) are analyzed. In Chapter 3, signals composed of sub-subsets (i) and (ii) are analyzed.

contrast in Chapter 3, signals composed of the deterministic slow (class (i)) and fast (class (ii)) oscillations will be analyzed, where cross-frequency coupling phenomena emergent from the interaction between the deterministic slow and fast oscillations is observed.

1.4 Organization of the thesis

The rest of this thesis has been organized as follows:
In Chapter 2, the definition of a novel dimension is derived from that of the conventional fractal dimension, to analysis signals composed of the deterministic oscillations and the stochastic fast oscillations. Typically, it has been shown that this new type of dimensions, named after time series dimension (TSD), can detect the level of the underlying dynamical noise only from time series and can be applied to a variety of time series data, because the TSD does not require any information included in dynamics generating time series so that it can work as a model-free indicator, as we will explain in Chapter 2. Note that the TSD is one of the nonlinear time series analysis because it can characterize nonlinear dynamics driven by dynamical noise, but it dose not need embedding of a time series on a high-dimensional state space with delay coordinates, and therefore the TSD should be located in another world different from the conventional nonlinear time series analysis theory. In fact, the ability of the TSD has been demonstrated with the application of it to EEG

signals, and based on this application, a possibility whether the TSD—which works even if the dynamics behind a time series is filled with noise—can open the door where many features characterizing nonlinear phenomena strongly connected to noise are hidden, has been discussed. The contents of Chapter 2 will be published in Phys. Lett. A.

In Chapter 3, a realistic stochastic neural network model—which is suitable to be applied to the mean field theory so that the model can be transformed into a macroscopic model—is proposed to demonstrate whether the model can show cross-frequency coupling phenomena, connecting the macroscopic and the microscopic properties, through the mean field approximation. Note that this technology called mean field approximation would involve crucial roles for uncovering the process of consciousness generation if there exists the feedback from the macroscopic model to microscopic one, but the proposed model has been formulated as a feedforward model because our main purpose in Chapter 3 is to reveal the effect of the mean field approximation on the stochastic model. The proposed stochastic model has been created as a discrete-time model so that the errors arising from the numerical temporal evolution cannot appear, towards the application of the model to real-world systems, especially for EEG dynamics. Accordingly, the stochastic model has been converted to the corresponding discrete-time dynamical system, and therefore the property of deterministic oscillations has been intensively investigated through the bifurcation analysis, where the deterministic slow and fast oscillations, realized by a subnetwork composed of excitatory neurons and by that composed of inhibitory neurons, respectively, are analyzed. Furthermore, it has been assumed that only the torus attractor corresponds to real oscillatory phenomena, because the torus emergent from the proposed model can be interpreted as the limit cycle attractor or the torus attractor in the corresponding continuous-time dynamical system, but the periodic attractor perhaps corresponds to the equilibrium point, due to the failure of convergence by the Euler method. The contents of Chapter 3 was submitted to Frontiers in Computational Neuroscience.

Finally in Chapter 4, this thesis will be briefly concluded, in terms of nonlinear dynamics with multiple time-scales.

Chapter 2

Analysis on signals composed of deterministic and stochastic oscillations

This chapter includes major parts of the contents in Ref. [1], which will be published in the journal of Physics Letters A.

2.1 Introduction

In general, time series data—for example, biological, meteorological, and economic data—are a collection of measurements recording the dynamical behavior of a system. When the underlying dynamics of the system is stochastic, the associated time series will behave like a stochastic process. Note, however, that the time series generated from deterministic systems may also be associated with stochastic fluctuations if the measured signals have been influenced by noise.

Typically, a time series contains two basic types of noise: dynamical noise and observational noise. The former refers to the noise affecting the system's dynamics, whereas the latter describes the noise influencing the observed or measured signal of the system. The system including these two distinctive kinds of noise is defined as follows [23]:

$$\mathrm{d}x_q = f_q(\vec{x})\mathrm{d}t + \rho_q(t)\mathrm{d}W_q(t), \text{ for } q = 1, 2, ..., d, \tag{2.1}$$

$$X_{\mathrm{obs}}(t) = H(\vec{x}) + \sigma_{\mathrm{X}}\xi_{\mathrm{X}}(t), \tag{2.2}$$

where x_q denotes the state variable, $\vec{x} = [x_1, x_2, ..., x_d]^{\mathrm{T}}$ is the state vector, function $f_q(\cdot)$ is either linear or nonlinear, and the dynamical noise is described by $\rho_q(t)\mathrm{d}W_q(t)$. Here, $\mathrm{d}W_q(t)$ indicates the Wiener process, which follows a normal distribution with mean 0 and standard deviation $\sqrt{\mathrm{d}t}$. To define the dynamical noise as red noise, the process of red-noise generation should be included in $f_q(\vec{x})$. We explicitly assume that the temporal change of $\rho_q(t)$ is slow compared with the dynamics of x_q. Note that Eq. (2.1) denotes a d-dimensional stochastic dynamical system, and the corresponding observational process

of this system is described by Eq. (2.2). Furthermore, from Eq. (2.1) and Eq. (2.2), it can be seen that $\vec{x}$ is converted to a one-dimensional variable $X_{\rm obs}(t)$ through observational function $H(\cdot)$ with observational noise $\sigma_{\rm X}\xi_{\rm X}(t)$, where $\xi_{\rm X}(t)$ follows a normal distribution with mean 0 and standard deviation 1. Usually, the corresponding time series of $\{X_{\rm obs}(t)\}$ is defined as follows:

$$\{X(i)\} \quad = \quad \{X_{\rm obs}(t)|X_{\rm obs}(t) = X_{\rm obs}(i\Delta t), i{\in}\mathbb{N}\}, \tag{2.3}$$

where $\{X_{\rm obs}(t)\}$ is converted to a time series $\{X(i)\}$ with sampling time Δt.

In this study, we assume that the amount of dynamical noise can be described as a time-dependent variable, which is denoted by $\rho_q(t)$ in Eq. (2.1). For example, consider a situation in which the amount of noise in a neural system is temporally adjusted by input from other areas of the brain to improve brain functions. The amount of observational noise, denoted by $\sigma_{\rm X}$ in Eq. (2.2), is assumed to be constant. This assumption is equivalent to the assumption that the measurement environment does not change during the observational process. For a measured signal of the form $X_{\rm obs}(t) = x_q(t) + \sigma_{\rm X}\xi_{\rm X}(t)$, the dynamical and observational noise levels have been defined as $\rho_q(t)/\sigma_{{\rm dyn}x_q}(t)$ and $\sigma_{\rm X}/\sigma_{{\rm dyn}x_q}(t)$, respectively, where $\sigma_{{\rm dyn}x_q}(t)$ indicates the standard deviation of the variable x_q. The time dependency of $\sigma_{{\rm dyn}x_q}(t)$ can be attributed to the fact that, in general, the dynamical system [Eq. (2.1)] behaves as a nonstationary process.

From the system's dynamics of Eq. (2.1), it is clear that dynamical noise may influence the behavior of the dynamical system. In fact, a large dynamical noise level increases the probability of a large trajectory change. The steady state of the dynamical system may drift into different regions in the state space. Thus, knowing the dynamical noise level is a fundamental to analyzing and understanding dynamical systems [24, 25].

However, dynamical noise is more difficult to be estimated than observational noise because the former is directly added to the dynamics of time evolution. If the dynamical system is known, we can formulate algorithms for estimating the dynamical noise level [26, 27]. Nevertheless, it should be noted that actual systems in the real world are usually unknown. For these systems, few methods have been proposed to estimate the dynamical noise level. For example, according to the work of Siefert et al. [28], an interesting quantitative method for analyzing dynamical noise has been proposed. This method can estimate the amount of noise in systems with unknown dynamics by using the Kramers-Moyal coefficients [29, 30], but the method requires a 'long' time series to estimate the mean and variance of a trajectory moving on an attractor. On the other hand, Urbanowicz and Holyst [31] proposed an important noise-level estimation method that assumes observational noise. Although they have suggested that their method is valid for observational noise as well as dynamical noise, we have found that their algorithm does not necessarily work well for estimation of the dynamical noise level.

In this paper, we propose a method for estimating the level of dynamical noise, which can be applied to even 'short' time series generated from unknown dynamics. This paper

is organized as follows. First, in Section 2.2, we present some definitions that are useful for the subsequent results. Next, in Section 2.3, we recall Urbanowicz and Holyst's method [31], with the numerical verification whether their method is applicable for even short time series. Then, in Section 2.4, we introduce the proposed method and verify its effectiveness as a dynamical noise indicator. Furthermore, in Section 2.5, our method is applied to human electroencephalographic (EEG) data in order to illustrate its applicability to real-world systems. Finally, discussions of the obtained results are presented in Section 2.6, and some conclusions are provided in Section 2.7.

2.2 Preliminaries

We analytically derive some definitions for short and long time series as follows. First, we define

$$I_1(c) = \int_{t_0}^{c} \frac{\left|\mathrm{E}_{\tau+h}[\{X_{\mathrm{obs}}(t)\}] - \mathrm{E}_{\tau}[\{X_{\mathrm{obs}}(t)\}]\right|}{h} \mathrm{d}\tau, \tag{2.4}$$

$$I_2(c) = \int_{t_0}^{c} \frac{\left|\mathrm{Var}_{\tau+h}[\{X_{\mathrm{obs}}(t)\}] - \mathrm{Var}_{\tau}[\{X_{\mathrm{obs}}(t)\}]\right|}{h} \mathrm{d}\tau, \tag{2.5}$$

where $0<h\ll 1$, and operators $\mathrm{E}_{\tau}[\cdot]$ and $\mathrm{Var}_{\tau}[\cdot]$ denote the mean and variance, respectively, and are defined as follows:

$$\mathrm{E}_{\tau}[\{X_{\mathrm{obs}}(t)\}] = \frac{1}{h'} \int_{\tau}^{\tau+h'} X_{\mathrm{obs}}(t) \mathrm{d}t, \tag{2.6}$$

$$\mathrm{Var}_{\tau}[\{X_{\mathrm{obs}}(t)\}] = \frac{1}{h'} \int_{\tau}^{\tau+h'} \left(X_{\mathrm{obs}}(t) - \mathrm{E}_{\tau}[\{X_{\mathrm{obs}}(t)\}]\right)^2 \mathrm{d}t, \tag{2.7}$$

with $0<h'\ll 1$. The two quantities $I_1(c)$ and $I_2(c)$ indicate the sums of discrepancies $|\cdot|$ of partial observational signals $\{X_{\mathrm{obs}}(s)\}$ over $\tau\leq s\leq \tau+h$ with $0\leq t_0\leq c$ and $t_0\leq c\leq T$; t_0 and T are a starting point and an ending point of an observation, respectively. Then, if $\{X_{\mathrm{obs}}(s)\}$ behaves as a stationary process, both quantities $I_1(c)$ and $I_2(c)$ are almost equal to zero, even if c becomes large, because the mean and variance of the stationary process do not change over time. However, in this study, we analyze signals observed from a stochastic dynamical system [see Eq. (2.1)], in which variables usually behave as nonstationary processes, so that observational signals also stand for nonstationarity. In fact, each of quantities $I_1(c)$ and $I_2(c)$ represents a margin between stationarity and nonstationarity [see Fig. 2.1]. Note that in Eq. (2.4) and Eq. (2.5), if h is set to a very small value, the partial signal $\{X_{\mathrm{obs}}(s)\}$ can be considered as a 'semi-stationary' process.

Depending on whether the target signal is near stationarity, the present method works either as a universal indicator among systems or as an intrinsic indicator for each system. If the target signal is near stationarity, i.e., it is observed as a short time series, the method can universally extract the dynamical noise level for many systems; if the target signal is far from stationarity, i.e., it is observed as a long time series, the method can specifically

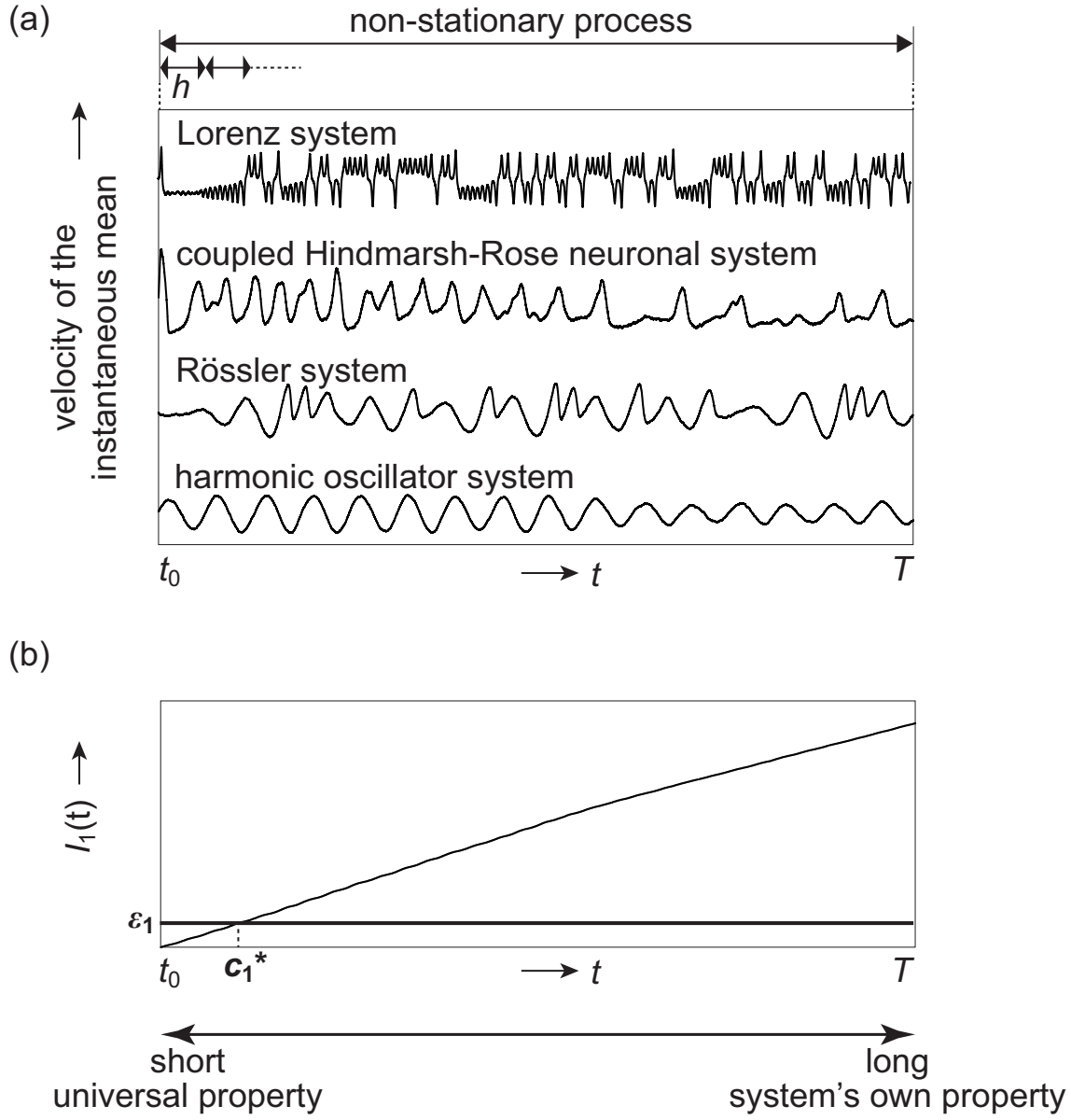

Figure 2.1. Concept of a separation between short and long time series by discrepancies introduced between stationarity and nonstationarity arising from the fact that a partial short-term signal $X_{\rm obs}(s)$ with very short length h is a semi-stationary process. (a) Four time series sorted in accordance with the velocity of the instantaneous mean value of the time series from bottom to top: the harmonic oscillator system, the Rössler system, the coupled Hindmarsh-Rose neuronal system, and the Lorenz system. The time series were obtained with $\rho_q(t)/\sigma_{{\rm dyn}x_q}(t) = 0.1$. (b) A schematic example of the accumulation $I_1(t)$ of discrepancies. An upper bound ϵ_1 determines a threshold value c_1^*. If the accumulation $I_1(t) < \epsilon_1$, we call this time series a short time series, and $I_1(t)$ reflects a more universal property among systems. If $I_1(t)$ is large, we call this time series a long time series, and $I_1(t)$ reflects a more specific property of the system because the longer the time series increases, the more its wave form differs from those of other time series.

extract the dynamical noise level for each system so that the extracted levels are not comparable among systems, but involve properties of their respective systems. Thus, it is essential to flexibly determine a boundary between short and long time series.

To choose a threshold value c^*, by which we can define whether a time series is short or long, we use Eq. (2.4) and Eq. (2.5) with two upper bounds ϵ_1 ($0<\epsilon_1$) and ϵ_2 ($0<\epsilon_2$), and compute c_1^* and c_2^* such that

$$I_1(c_1^*) = \epsilon_1, \tag{2.8}$$

$$I_2(c_2^*) = \epsilon_2. \tag{2.9}$$

Then, we define the threshold value c^* as follows:

$$c^* = \min(c_1^*, c_2^*). \tag{2.10}$$

The computation of c^* is provided in Appendix A. This threshold value c^* determines whether the length $L_{\mathrm{seg}}(t_0, \Delta t)$ of a time series $\{X(i)\}$ is short or long. If the inequality

$$L_{\mathrm{seg}}(t_0, \Delta t) \leq (c^* - t_0)/\Delta t \tag{2.11}$$

is satisfied, the time series is assumed to be short. Otherwise, the time series is referred to as a long time series. Note that Eq. (2.4) and Eq. (2.5) define $I_1(c_1^*)$ and $I_2(c_2^*)$ like differences, rather than derivatives because $\{X_{\mathrm{obs}}(t)\}$ may be a non-smooth time series. Equations (2.4) to (2.11) can be seen as a set of general definitions for the length of a time series generated from a continuous-time dynamical system. Throughout this paper, when we discuss whether a time series is short or long, we denote the length of the time series as $L_{\mathrm{seg}}(t_0, \Delta t)$, otherwise as N, which refers to the data size of the time series.

2.3 Previous method for noise-level estimation

First, we introduce the previous method for noise-level estimation, which uses coarse-grained entropy [31]. Because this algorithm assumes observational noise, it may fail when trying to estimate the level of dynamical noise.

2.3.1 Urbanowicz and Holyst's method

Suppose that a time series $\{X(i)\}$ with $i = 1, 2, ..., N$ is given. Furthermore, assume that it is influenced neither by observational noise nor by dynamical noise, i.e. assume a 'clean' time series. Then, we construct M-dimensional delay coordinates as $\vec{X}_M(i) = \{X(i), X(i+\Gamma), ..., X(i+(M-1)\Gamma)$, where M and Γ are an embedding dimension and an embedding delay, respectively. We define the correlation integral with a threshold value ε for $\vec{X}_M(i)$ as

$$C^M(\varepsilon) = \frac{1}{N^2} \sum_{i}^{N} \sum_{p \neq i}^{N} \theta(\varepsilon - \|\vec{X}_M(i) - \vec{X}_M(p)\|), \tag{2.12}$$

where $\theta(\cdot)$ is the Heaviside function, defined as

$$\theta(u) = \begin{cases} 0 & (u < 0), \\ 1 & (u \geq 0). \end{cases} \tag{2.13}$$

For simplicity, we use the maximum norm. In addition, the term $C^M(\varepsilon)$ allows to define the coarse-grained correlation entropy, denoted by $K_2(\varepsilon)$, as follows [33, 34]:

$$K_2(\varepsilon) = \lim_{\varepsilon \to 0} \lim_{M \to \infty} \ln \frac{C^M(\varepsilon)}{C^{M+1}(\varepsilon)} \approx - \frac{\mathrm{d} \ln C^M(\varepsilon)}{\mathrm{d}M}. \tag{2.14}$$

The term $K_2(\varepsilon)$ is an ideal entropy, which cannot be obtained in reality. In practice, we obtain a noisy version of this entropy, i.e. $K_{\mathrm{noisy}}(\varepsilon)$ [31] instead of $K_2(\varepsilon)$, when the Gaussian observational noise is added to $\{X(i)\}$; we call this $K_{\mathrm{noisy}}(\varepsilon)$ as the observed coarse-grained entropy defined as follows:

$$\begin{aligned} K_{\mathrm{noisy}}(\varepsilon) = & -\frac{1}{\Gamma} g\left(\frac{\varepsilon}{2\sigma}\right) \ln \varepsilon + [\kappa + b \ln(1 - \alpha\varepsilon)] \\ & \times \left(1 + \sqrt{\pi} \frac{\sqrt{\varepsilon^2/3 + 2\sigma^2} - \varepsilon/\sqrt{3}}{\varepsilon}\right), \end{aligned} \tag{2.15}$$

where σ denotes the standard deviation of the Gaussian observational noise. The term $[\kappa + b \ln(1 - \alpha\varepsilon)]$ represents the approximate form of $K_2(\varepsilon)$; κ is the correlation entropy; $b \ln(1 - \alpha\varepsilon)$ indicates the effect of the coarse graining. Here, we define $g(\cdot)$ as follows:

$$g(v) = \frac{2}{\sqrt{\pi}} \frac{v \exp(-v^2)}{\mathrm{Erf}(v)}, \tag{2.16}$$

where $\mathrm{Erf}(v)$ shows the error function defined as

$$\mathrm{Erf}(v) = \frac{2}{\sqrt{\pi}} \int_0^v \exp(-t^2) \mathrm{d}t. \tag{2.17}$$

We fit parameters κ, α, b, and σ by using Eq. (2.15) based on given time series data.

2.3.2 Examples

Here, we discuss some examples of short time series for which Urbanowicz and Holyst's method does not produce estimates that sufficiently correlate with the actual dynamical noise levels [see Figs. 2.2(a) to (d)]. In these examples, the relationship between the estimated and the actual levels of dynamical noise has been investigated numerically with the use of their method [31]. Time series data (sampled observational signals) were generated with four types of systems, each of which was influenced by dynamical noise $\rho_w \mathrm{d}W_w(t)$ ($w \in \{\mathrm{x}, \mathrm{y}, \mathrm{z}, \mathrm{x}_n, \mathrm{y}_n, \mathrm{z}_n\}$) and converted to observational signals $\{X_{\mathrm{obs}}(t)\}$:
(I) The harmonic oscillator system was simulated with

$$\mathrm{d}x = y\mathrm{d}t + \rho_{\mathrm{x}} \mathrm{d}W_{\mathrm{x}}(t), \tag{2.18}$$

$$\mathrm{d}y = -x\mathrm{d}t + \rho_{\mathrm{y}} \mathrm{d}W_{\mathrm{y}}(t), \tag{2.19}$$

$$X_{\mathrm{obs}}(t) = x(t) + \sigma_{\mathrm{X}} \xi_{\mathrm{X}}(t). \tag{2.20}$$

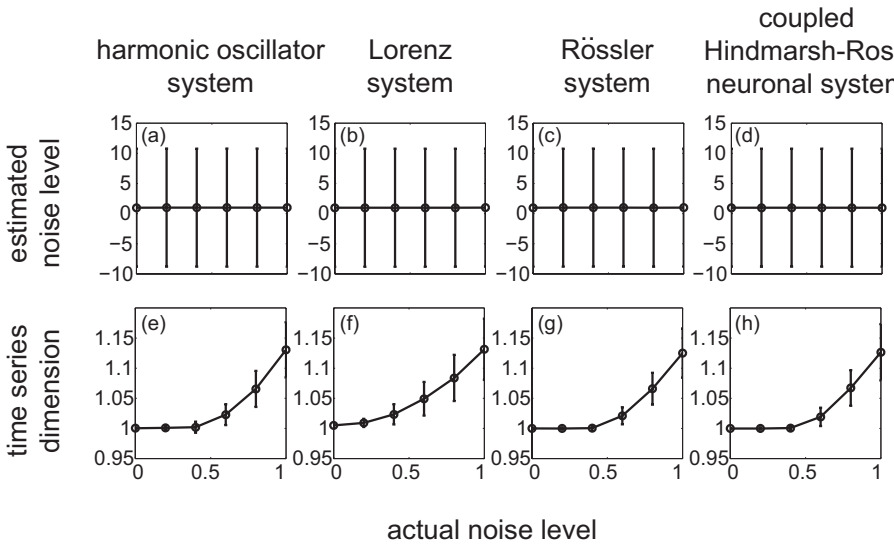

Figure 2.2. (a) to (d): Relationship between the noise level estimated with Urbanowicz and Holyst's method and the actual dynamical noise level. (e) to (h): Relationship between the time series dimension (TSD) and the actual dynamical noise level. Time series data were generated by the harmonic oscillatory system for (a) and (e), the Lorenz system for (b) and (f), the Rössler system for (c) and (g), and the coupled Hindmarsh-Rose neuronal system for (d) and (h), respectively.

(II) The Lorenz system was simulated with

$$\begin{aligned} \mathrm{d}x &= [-10x + 28y]\,\mathrm{d}t + \rho_{\mathrm{x}}\mathrm{d}W_{\mathrm{x}}(t), && (2.21)\\ \mathrm{d}y &= [-xz + 28x - y]\,\mathrm{d}t + \rho_{\mathrm{y}}\mathrm{d}W_{\mathrm{y}}(t), && (2.22)\\ \mathrm{d}z &= [xy - (8/3)z]\,\mathrm{d}t + \rho_{\mathrm{z}}\mathrm{d}W_{\mathrm{z}}(t), && (2.23)\\ X_{\mathrm{obs}}(t) &= x(t) + \sigma_{\mathrm{X}}\xi_{\mathrm{X}}(t). && (2.24) \end{aligned}$$

(III) The Rössler system was simulated with

$$\begin{aligned} \mathrm{d}x &= [-y - z]\,\mathrm{d}t + \rho_{\mathrm{x}}\mathrm{d}W_{\mathrm{x}}(t), && (2.25)\\ \mathrm{d}y &= [x + 0.36y]\,\mathrm{d}t + \rho_{\mathrm{y}}\mathrm{d}W_{\mathrm{y}}(t), && (2.26)\\ \mathrm{d}z &= [0.4 + z(x - 4.5)]\,\mathrm{d}t + \rho_{\mathrm{z}}\mathrm{d}W_{\mathrm{z}}(t), && (2.27)\\ X_{\mathrm{obs}}(t) &= x(t) + \sigma_{\mathrm{X}}\xi_{\mathrm{X}}(t). && (2.28) \end{aligned}$$

(IV) The coupled Hindmarsh-Rose neuronal system [35] with 100 neurons, the nth neuron of which was influenced by the external input I_n, was simulated with

$$\begin{aligned}
\mathrm{d}x_n &= \left[y_n - x_n^3 + 3x_n^2 - z_n + I_n + \sum_{\gamma \neq n}^{100} 0.05\theta(x_\gamma) \right] \mathrm{d}t + \rho_{\mathrm{x}_n} \mathrm{d}W_{\mathrm{x}_n}(t), \quad (2.29) \\
\mathrm{d}y_n &= \left[1 - 5x_n^2 - y_n \right] \mathrm{d}t + \rho_{\mathrm{y}_n} \mathrm{d}W_{\mathrm{y}_n}(t), \quad (2.30) \\
\mathrm{d}z_n &= \left[0.006\{4(x_n + 1.6) - z_n\} \right] \mathrm{d}t + \rho_{\mathrm{z}_n} \mathrm{d}W_{\mathrm{z}_n}(t), \quad (2.31) \\
X_{\mathrm{obs}}(t) &= \frac{1}{100} \sum_{n=1}^{100} x_n(t) + \sigma_{\mathrm{X}} \xi_{\mathrm{X}}(t), \quad (2.32)
\end{aligned}$$

see Eq. (2.13) for $\theta(\cdot)$, where the amount ρ_w of the dynamical noise was constant over time. The stochastic variable $\mathrm{d}W_w$ follows a normal distribution of mean 0 and standard deviation $\sqrt{\mathrm{d}t}$. For systems (I) through (IV), the observational signal $\{X_{\mathrm{obs}}(t)\}$ has been used to test Urbanowicz and Holyst's method, and for simplicity, we have assumed that the signal is independent of observational noise $\sigma_{\mathrm{X}}\xi_{\mathrm{X}}(t)$ by setting $\sigma_{\mathrm{X}} = 0$. Actually, in the network composed of the Hindmarsh-Rose neurons [Eqs. (2.29) to (2.32)], a synchronized chaotic oscillation appears [36]. Each value of $\{I_n\}$ has been uniformly distributed between 1 and 5. Fifty time series of $\{X_{\mathrm{obs}}(t)\}$ were simulated with respect to each noise level, which is defined as $\rho_w/\sigma_{\mathrm{dyn}w}$. Here $\sigma_{\mathrm{dyn}w}$ indicates the standard deviation of the variable w, and the initial condition of w follows the uniform distribution between 0 and 1 for each noise level. Note that $\sigma_{\mathrm{dyn}w}$ is not time-dependent because the simulation was conducted repeatedly over multiple trials. The sampling time Δt was set to 0.001, and the length $L_{\mathrm{seg}}(0, \Delta t)$ of each time series was set to 100 points, in which the transient state following the onset of the simulation was included in the tested time series, i.e., $t_0 = 0$ hereafter.

The time series with length of $L_{\mathrm{seg}}(0, \Delta t) = 100$ were identified as short time series by calculations of the quantities $I_1(c)$ and $I_2(c)$ [Eq. (2.4) and Eq. (2.5)], in which $\mathrm{E}_\tau[\cdot]$ and $\mathrm{Var}_\tau[\cdot]$ were calculated with an analysis window $h' = 0.005$. Then, h was set to 0.001 so that a partial observational signal $\{X_{\mathrm{obs}}(s)\}$ over $\tau \leq s \leq \tau + h$ can be considered as a semi-stationary process. The upper bounds ϵ_1 and ϵ_2 [see Eq. (2.8) and Eq. (2.9)] have been chosen as follows: $\epsilon_1 = 1$ and $\epsilon_2 = 0.05$. For these values, the corresponding threshold values of c^* [Eq. (2.10)] for the four systems given in Eqs. (2.18) to (2.32) were $1781\Delta t$, $101\Delta t$, $225\Delta t$, and $103\Delta t$, respectively. In the calculation of c^* for each system, we have used 100 time series of $\{X_{\mathrm{obs}}(t)\}$ with $L_{\mathrm{seg}}(0, \Delta t) = 50000$. Consequently, for each system we have obtained 100 threshold values for c^*. Finally, the average of these values has been considered as the final threshold value c^*. When we estimated c^*, each system was affected by dynamical noise with the noise level of 0.1 and simulated for different initial conditions (uniformly distributed between 0 and 1) over 100 trials.

A system with any noise level $\rho_w/\sigma_{\mathrm{dyn}w}$ was simulated in two steps: first, a clean system, without any noise, was simulated with an initial condition $\vec{x}_0$, and the resulting standard deviation $\sigma_{\mathrm{dyn}w}$ was stored in memory; next, the system including dynamical

noise was simulated using the same initial condition $\vec{x}_0$ with the clean system, and then the noise level was set to the same values over x, y, and z or over $\{x_n\}$, $\{y_n\}$, and $\{z_n\}$, where ρ_w was obtained by multiplication between the arbitrarily set noise level and the stored $\sigma_{\mathrm{dyn}w}$.

In Urbanowicz and Holyst's method, we have defined the estimated noise level as $\hat{\sigma}/\sigma_{\mathrm{dyn}w}$, where $\hat{\sigma}$ represents the fitted standard deviation of the Gaussian observational noise [see Eq. (2.15)]. Clearly, the numerical results show that Urbanowicz and Holyst's method is not necessarily suitable for estimating the level of dynamical noise in the aforementioned four systems [Eqs. (2.18) to (2.32)].

2.4 Proposed method for noise-level estimation

In this section, a novel method for detecting changes in the level of dynamical noise is presented. Here consider two types of time series: (1) A series originating from a flow generated from a continuous-time dynamical system; (2) A series originating from a map generated from a discrete-time dynamical system. The proposed method can be applied to the former time series in the real world by calculating the fractal dimension developed by Higuchi [32], even if the dynamical system is unknown. To avoid confusing the fractal dimension with the correlation dimension in the reconstructed attractor, we call the fractal dimension using the Higuchi method as the time series dimension (TSD) because the Higuchi method considers a time series to be a figure represented on a two-dimensional space, in which the horizontal and vertical axes denote time and amplitude, respectively.

Here we assume that an observational signal is sampled with the time interval $\Delta t > 0$. Then, the TSD of the resulting time series reflects both the deterministic and stochastic components of the time series, and ranges from 1 to 1.5. When the dynamical system underlying the time series contains only the deterministic component, the TSD of the time series is 1 because the series locally resembles a line. In contrast, when the dynamical system underlying the time series contains only the stochastic component that represents the Gaussian dynamical noise, the TSD of the time series is 1.5, the fractal dimension of the Wiener process [39]. Therefore, the relative dominance ratio between the deterministic and stochastic components determines the TSD.

We stress the fact that in the present study, our focus is on a system [see Eq. (2.1)], in which the deterministic and stochastic components are mixed. Furthermore, since the observed signal [Eq. (2.2)] is sampled with the certain time interval, the corresponding TSD depends not only on the amount of dynamical noise but also on the sampling time Δt. If the deterministic component does not contribute to the system [Eq. (2.1)] at all, the TSD is 1.5, independent of the amount of dynamical noise and of the sampling time, as mentioned above. Further, the TSD does not require the power law.

In Section 2.4.1, we explain how to calculate the curve length of a given time series from a stochastic dynamical system of the form [Eq. (2.1)] by introducing the Higuchi

method [32]. In Section 2.4.2, we convert the curve length directly to the TSD. The target time series is the sampled signal $\{X_{\vec{\rho}}(i\Delta t)\}$ $(i = 1, 2, ..., N)$ of the variable x_q perturbed by dynamical noise with $\vec{\rho}(t) = (\rho_1(t), \rho_2(t), ..., \rho_d(t))$, or more precisely, with $\vec{\rho}(i\Delta t)$; namely, it has been assumed that $\{X_{\vec{\rho}}(i\Delta t)\}$ is influenced by dynamical noise, not by observational noise. Hereinafter, we denote $\vec{\rho}(i\Delta t)$ as $\vec{\rho}$, for simplicity. Finally, in Section 2.4.3, we present a numerical investigation of the proposed method, in which the level of dynamical noise has been estimated.

2.4.1 Curve length of time series

The Higuchi method [32] is based on the following expression [38] for calculating the curve length,

$$L^{(q)}(\Delta t, \vec{\rho}) = \frac{\sum_{i=1}^{N-1} \left| X_{\vec{\rho}}((i+1)\Delta t) - X_{\vec{\rho}}(i\Delta t) \right|}{\Delta t}, \tag{2.33}$$

where $L^{(q)}(\Delta t, \vec{\rho})$ is an ideal definition of the curve length, but this definition does not work well when we try to get an appropriate TSD. The Higuchi method solves this problem by course-graining the time series and creating some new time series sampled with $\zeta_k = k\Delta t$, in which k is a natural number. A larger k results in a larger sampling time ζ_k.

Consequently, in the Higuchi method, the modified curve length $\tilde{L}^{(q)}$ associated to the time series $\{X_{\vec{\rho}}(i\Delta t)\}$ corresponding to the variable x_q is calculated as follows:

$$\tilde{L}^{(q)}(\zeta_k, \vec{\rho}) = \frac{1}{k} \sum_{m=1}^{k} L_m^{(q)}(\zeta_k, \vec{\rho}), \tag{2.34}$$

where

$$L_m^{(q)}(\zeta_k, \vec{\rho}) = \left\{ \left(\sum_{j=1}^{\lfloor \frac{N-m}{k} \rfloor} \left| X_{\vec{\rho}}((m+jk)\Delta t) - X_{\vec{\rho}}((m+(j-1)k)\Delta t) \right| \right) \times \frac{N-1}{\lfloor \frac{N-m}{k} \rfloor k} \right\} / \zeta_k. \tag{2.35}$$

Here, the notation $\lfloor \cdot \rfloor$ denotes the rounding down; the term $(N-1)/(\lfloor (N-m)/k \rfloor k)$ normalizes the curve length of a segment; and the variable $L_m^{(q)}(\zeta_k, \vec{\rho})$ represents the curve length of the segment with a starting point m. Namely, the process of Eq. (2.35) constructs k new segments $\{X_k^m(\vec{\rho})\}$ with $m = 1, 2, ..., k$, each segment of which is defined by

$$X_k^m(\vec{\rho}) = \left\{ X_{\vec{\rho}}(m\Delta t), X_{\vec{\rho}}((m+k)\Delta t), X_{\vec{\rho}}((m+2k)\Delta t), ..., X_{\vec{\rho}}\left(\left(m + \left\lfloor \frac{N-m}{k} \right\rfloor k \right) \Delta t \right) \right\}. \tag{2.36}$$

Note that the Higuchi method targets the time series sampled with ζ_k, so that the process of Eq. (2.35) performs division by ζ_k instead of Δt [see Eq. (2.33)]. Then, any curve length of the time series sampled with ζ_k can be calculated by coarse-graining of the time series.

2.4.2 Relationship between time series dimension and noise level

The definition of the TSD is based on the box-counting dimension [39], and is given as follows:

$$D = \lim_{\phi \to 0} \frac{\log N(\phi)}{\log (1/\phi)}, \tag{2.37}$$

where the variable $N(\phi)$ represents a minimal value of the total number of hyperspheres or the hypercubes with size ϕ needed to entirely cover a structure like a coast line. When the size ϕ and the variable $N(\phi)$ are substituted with the sampling time ζ_k and the curve length $\tilde{L}^{(q)}(\zeta_k, \vec{\rho})$ of the time series associated with the variable x_q, respectively, we get an idealized version of the TSD instead of Eq. (2.37), as follows:

$$D^{(q)} = \lim_{\Delta t \to 0} \frac{\log \tilde{L}^{(q)}(\zeta_k, \vec{\rho})}{\log (1/\zeta_k)}. \tag{2.38}$$

We show below the relationship between $D^{(q)}$ and $\vec{\rho}$ based on Eq. (2.38), where the TSD is converted to an approximate version; note that only the approximate TSD depends on $\vec{\rho}$. For simplicity, we investigate the situation in which only one variable x_q of the dynamical system [Eq. (2.1)] is observed in the observational process and furthermore, we assume that observational noise does not influence the process. The TSD is calculated in the case of $\Delta t \to 0$ as shown in Eq. (2.38), so that the TSD is approximated as follows:

$$D^{(q)} \approx \frac{\log \tilde{L}^{(q)}(\zeta_1, \vec{\rho}) - \log \tilde{L}^{(q)}(\zeta_2, \vec{\rho})}{\log 2} \equiv \tilde{D}^{(q)}(\vec{\rho}, \Delta t), \tag{2.39}$$

where this approximate version is the proposed TSD [see examples in Fig. 2.3] and becomes a function of $\vec{\rho}$ and of Δt; hereinafter, we denote this TSD as $\tilde{D}^{(q)}(\vec{\rho})$ because Δt is constant throughout this paper, i.e. $\Delta t = 0.001$ except for Fig. 2.9. Note that if Δt is small enough so that the time series $\{X_{\vec{\rho}}(i\Delta t)\}$ behaves like a flow, the difference $\log \tilde{L}^{(q)}(\zeta_1, \vec{\rho}) - \log \tilde{L}^{(q)}(\zeta_2, \vec{\rho})$ reflects almost entirely the stochastic component, thus the TSD does not depend on $\vec{\rho}$ and always indicates 1.5, except at $\vec{\rho} = \vec{0}$. However, in this study we assume that the observational signal is sampled with a certain sampling time Δt, and consequently, the TSD reflects properties of both the deterministic and stochastic components and ranges between 1 and 1.5 in a certain range of $\vec{\rho}$ [see Section 2.4.3]. Furthermore, it can be seen that despite the fact that the approximate calculation [Eq. (2.39)] uses only two points to form the power law between $\tilde{L}^{(q)}(\zeta_k, \vec{\rho})$ and ζ_k [see Fig. 2.3], these two points might be essential to construct the power law; this view seems to be equivalent to the operation of $\Delta t \to 0$ included in the ideal definition [Eq. (2.39)] of the TSD. Namely, the power law tends to converge to a slope formed by the two points as $\Delta t \to 0$ [see Fig. 2.3]. Hence, the proposed TSD becomes a more flexible version of the conventional Higuchi's fractal dimension (which handles only fractal signals) and can be applied to any system.

Using Eqs. (2.34), (2.35), and (2.39), we can calculate the TSD. If the right-hand side of Eq. (2.39) is smooth with respect to ρ_r ($r = 1, 2, ..., d$), we can compute its derivative in

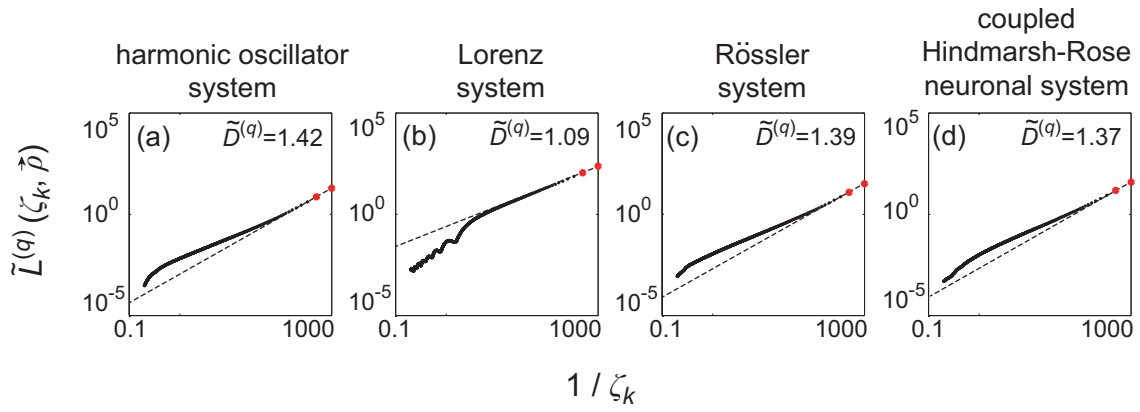

Figure 2.3. Diverse scaling property of time series data with $L_{\mathrm{seg}}(0, 0.001) = 10000$, observed through (a) the harmonic oscillatory system, (b) the Lorenz system, (c) the Rössler system, and (d) the coupled Hindmarsh-Rose neuronal system, each system of which was affected by dynamical noise with the noise level of 0.1. For each panel, both the horizontal and vertical axes are displayed by log scales, and the time series dimension (TSD) was calculated as a slope of the approximate line given by only two points $\left(1/\zeta_1, \tilde{L}^{(q)}(\zeta_1, \vec{\rho})\right)$ and $\left(1/\zeta_2, \tilde{L}^{(q)}(\zeta_2, \vec{\rho})\right)$, indicated by filled red circles.

order to reveal the monotonic relationship between the TSD and the noise level. However, when the Higuchi method is applied to the time series to calculate its curve length, the resulting TSD becomes a non-smooth function because the absolute function is contained in the curve length calculation [Eq. (2.35)] and consequently, the derivative of Eq. (2.39) does not exist at certain points. In order to circumvent this problem, we conduct piecewise differentiation, excluding the non-smooth set defined as follows:

$$\Omega_r^* = \left\{ \rho_r \;\middle|\; \lim_{\Delta\rho_r \to +0} \frac{\tilde{D}^{(q)}(\vec{\rho} + \Delta\vec{\rho}_r) - \tilde{D}^{(q)}(\vec{\rho})}{\Delta\rho_r} \neq \lim_{\Delta\rho_r \to -0} \frac{\tilde{D}^{(q)}(\vec{\rho} + \Delta\vec{\rho}_r) - \tilde{D}^{(q)}(\vec{\rho})}{\Delta\rho_r} \right\} \cup \{-\infty, \infty\}, \tag{2.40}$$

where $\Delta\vec{\rho}_r$ is a small deviation around ρ_r such that $\Delta\vec{\rho}_r = (0, 0, ..., \Delta\rho_r, ..., 0, 0)$ and implicitly depends on time. Using the following set

$$\Omega_r^{(S,E)} = \left\{ \rho_r \;\middle|\; \lim_{\Delta\rho_r \to +0} \frac{\tilde{D}^{(q)}(\vec{\rho} + \Delta\vec{\rho}_r) - \tilde{D}^{(q)}(\vec{\rho})}{\Delta\rho_r} = \lim_{\Delta\rho_r \to -0} \frac{\tilde{D}^{(q)}(\vec{\rho} + \Delta\vec{\rho}_r) - \tilde{D}^{(q)}(\vec{\rho})}{\Delta\rho_r}, \right.$$
$$\left. S < \rho_r < E, S < E, S \in \Omega_r^*, E \in \Omega_r^*, (S, E) \cap \Omega_r^* = \emptyset \right\}, \tag{2.41}$$

which sorts the differentiable domains, we can perform piecewise differentiation of Eq. (2.39) by $\rho_r \in \Omega_r^{(S,E)}$as follows:

$$\frac{\partial \tilde{D}_{\mathrm{pw}}^{(q)}(\vec{\rho})}{\partial \rho_r} = \frac{1}{\log 2} \left[\frac{1}{\tilde{L}_{\mathrm{pw}}^{(q)}(\zeta_1, \vec{\rho})} \frac{\partial \tilde{L}_{\mathrm{pw}}^{(q)}(\zeta_1, \vec{\rho})}{\partial \rho_r} - \frac{1}{\tilde{L}_{\mathrm{pw}}^{(q)}(\zeta_2, \vec{\rho})} \frac{\partial \tilde{L}_{\mathrm{pw}}^{(q)}(\zeta_2, \vec{\rho})}{\partial \rho_r} \right]. \tag{2.42}$$

Subindex "pw" indicates that the functions $\tilde{D}^{(q)}(\vec{\rho})$ and $\tilde{L}^{(q)}(\zeta_k, \vec{\rho})$ are piecewisely and sufficiently smooth over interval (S, E) for ρ_r. If $r \neq q$ [see Eq. (2.1)], the TSD $\tilde{D}^{(q)}(\vec{\rho})$ does not change with ρ_r because the dynamical noises $\{\rho_r(t)\mathrm{d}W_r(t)\}_{r\neq q}$ are integrated twice over t when they influence the variable x_q and the integrated Wiener process becomes smooth [see the propagation of dynamical noises in Appendix B]; namely, the derivative of $\tilde{D}^{(q)}_{\mathrm{pw}}(\vec{\rho})$ with respect to ρ_r is zero. Consequently, if the following inequality

$$\frac{\partial \tilde{D}^{(q)}_{\mathrm{pw}}(\vec{\rho})}{\partial \rho_q} > 0 \tag{2.43}$$

is satisfied over the concatenation of S and E, and if $\tilde{D}^{(q)}(\vec{\rho})$ is continuous with respect to ρ_q, then $\tilde{D}^{(q)}(\vec{\rho})$ increases with ρ_q, so that the noise level can be estimated by the TSD. Here, we can easily prove that the absolute function within $\tilde{L}^{(q)}(\zeta_k, \vec{\rho})$, see Eq. (2.35), is continuous with respect to ρ_q by using the (ϵ, δ)-definition of limit [40] and consequently, $\tilde{L}^{(q)}(\zeta_k, \vec{\rho})$ is a continuous function. Note that the inner operation, the increment of $X_{\vec{\rho}}(i\Delta t)$, of the absolute function is also continuous [Eq. (2.35)] because $X_{\vec{\rho}}(i\Delta t)$ continuously changes with the dynamical noise level.

Further, we analytically derive an inequality including Δt, $\vec{\rho}$, and the length $L_{\mathrm{seg}}(0, \Delta t)$ of the time series for the case of linear stochastic dynamical systems [see Appendix C]. Moreover, we summarize our analytic result in the form of a proposition related to the monotonic relationship between the TSD and the noise level [see Proposition C.1 in Appendix C]. Additionally, the monotonic relationship between $\tilde{D}^{(q)}(\vec{\rho})$ and ρ_q on the $(L_{\mathrm{seg}}(0, \Delta t), \rho_q/\sigma_{\mathrm{dyn}x_q})$-plane is numerically illustrated for the case of a harmonic oscillator.

2.4.3 Numerical investigation

In the proposed method, we can detect changes in the level of dynamical noise by using the TSD. Here, we numerically investigate the relationship between the TSD and the noise level in the harmonic oscillator system [Eqs. (2.18) to (2.20)], the Lorenz system [Eqs. (2.21) to (2.24)], the Rössler system [Eqs. (2.25) to (2.28)], and the coupled Hindmarsh-Rose neuronal system [Eqs. (2.29) to (2.32)], through which we observed short time series of $\{X_{\mathrm{obs}}(t)\}$ with the length $L_{\mathrm{seg}}(0, \Delta t) = 100$, and generated TSDs among 50 trials to create the monotonic properties, with respect to each noise level. As well as in Section 2.3.2, the transient state following the onset of the simulation was included in the tested time series and the initial condition of variables for each trial followed uniform distributions between 0 and 1. The obtained results, depicted in Figs. 2.2(e) through 2.2(h), show that the TSD increases with the noise level, which ranges from 0 to 5 [see Fig. 2.4], and further, the detailed monotonically increasing properties were similar among systems, so that there exists a possibility that the TSD can be a universal value related to the dynamical noise level [see Fig. 2.5].

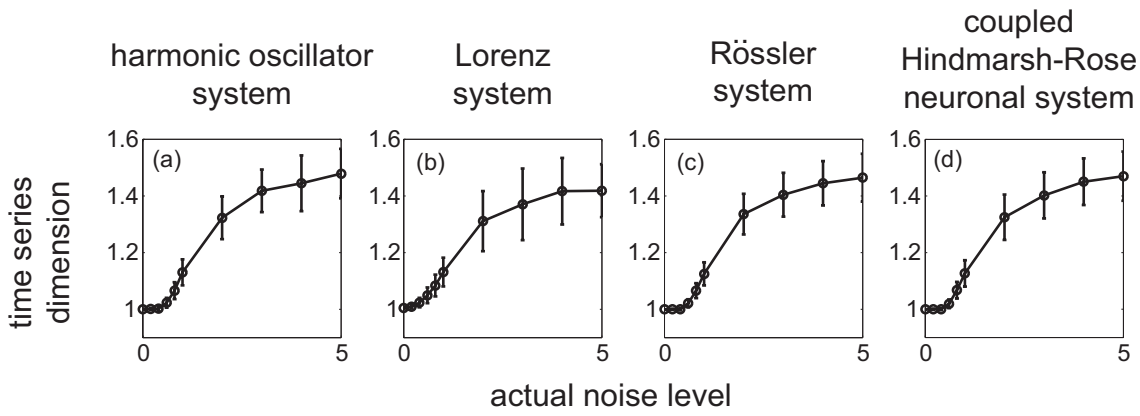

Figure 2.4. Relationship between the time series dimension (TSD) and the actual dynamical noise level, which ranges from 0 to 5. Time series data were generated by (a) the harmonic oscillator system, (b) the Lorenz system, (c) the Rössler system, and (d) the coupled Hindmarsh-Rose neuronal system, respectively, over 100 trials for each noise level.

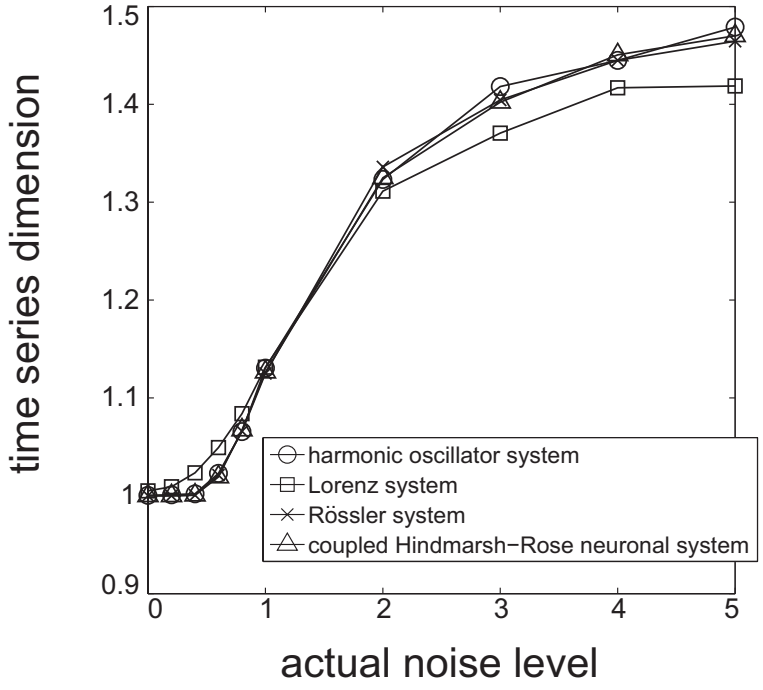

Figure 2.5. An illustrative comparison among systems' monotonic properties of the time series dimension (TSD) with respect to the actual dynamical noise level of short time series, observed through four types of systems: the harmonic oscillator system, the Lorenz system, the Rössler system, and the coupled Hindmarsh-Rose neuronal system. Time series data used here were the same with Fig. 2.4.

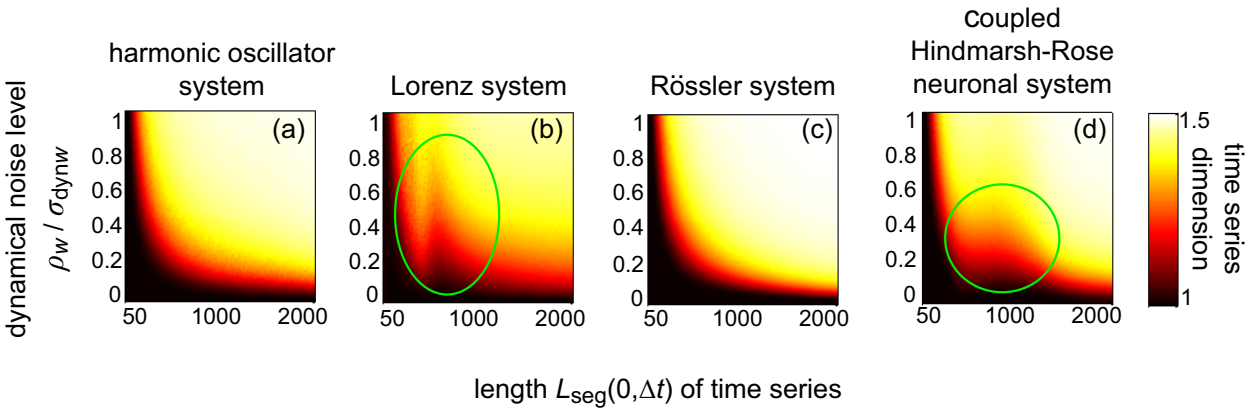

Figure 2.6. The effect of the length of time series and the dynamical noise level on the monotonic properties among systems: (a) the harmonic oscillatory system, (b) the Lorenz system, (c) the Rössler system, and (d) the coupled Hindmarsh-Rose neuronal system. A larger time series dimension (TSD) is indicated by a lighter color. The effect resulting from the length differs among systems, as shown in areas indicated by open green circles, due to a reflection of systems' own properties to the TSD.

However, if the length of the time series increases to include properties of the respective system, the monotonic behavior differs among systems, as shown in Fig. 2.6. Actually, we displayed the $(L_{\mathrm{seg}}(0,\Delta t), \rho_w/\sigma_{\mathrm{dyn}w})$ diagrams to reveal the effect of the length of time series on the monotonic behavior for the four systems. Each parameter point on the $(L_{\mathrm{seg}}(0,\Delta t), \rho_w/\sigma_{\mathrm{dyn}w})$ diagram indicates the average value of 100 TSDs calculated from time series generated from the corresponding system; namely, for each point in the $(L_{\mathrm{seg}}(0,\Delta t), \rho_w/\sigma_{\mathrm{dyn}w})$-plane, we generated TSDs among 100 trials as well as Fig. 2.4, where each simulation was conducted for initial conditions following the uniform distribution between 0 and 1. In particular, the diagrams for the Lorenz system and for the coupled Hindmarsh-Rose neuronal system showed specific monotonic behavior, which is different from the other systems [see Figs. 2.6(b) and 2.6(d)]. Note, however, that the TSD can still estimate the noise level for each system. In conclusion, the TSD can estimate the level of dynamical noise for a system on the basis of a monotonic relation.

2.5 Application to EEG data

We applied the proposed method to human EEG data [see Fig. 2.7]. Two healthy subjects gave written informed consent prior to participation in the experiment. The EEG study was approved by the ethics committees of RIKEN and the University of Tokyo. EEG signals from 63 electrodes were obtained during eyes-open and eyes-closed resting periods. We ran the experiment in a sound-proof, dimly lit room. A cycle of the measurement consists of the eyes-open and eyes-closed periods, each of length 35 s. The cycle of 70 s

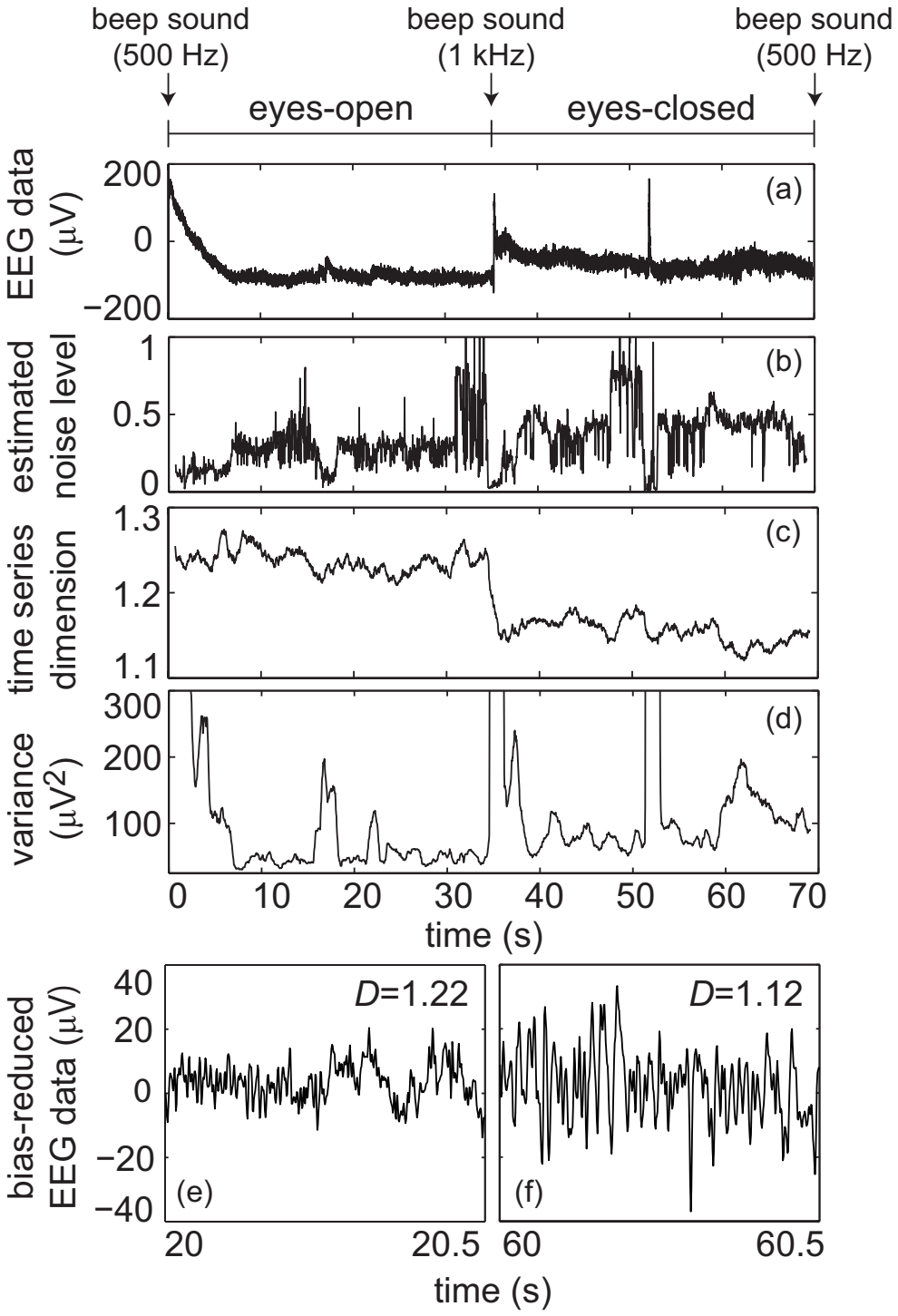

Figure 2.7. (a) A representative EEG signal obtained from electrode Fp2 during the eyes-open and eyes-closed resting periods. (b) The estimated noise level with Urbanowicz and Holyst's method. (c) The time series dimension (TSD), and (d) the variance. The arrows indicate the onset of the eyes-open or eyes-closed state. (e) A typical time series of the eyes-open state, the TSD of which was 1.22. (f) A typical time series of the eyes-closed state, the TSD of which was 1.12.

was repeated 10 times for two subjects. Sound stimuli (500 Hz or 1 kHz beep) were used to ask subjects to open or close their eyes. Subjects were required to be fixated on a white cross on a black background on a CRT display in the eyes-open condition. The reference electrodes were placed on both the left and right earlobes, and the sampling frequency was set to 1 kHz. Then, the frequencies of the low- and high-pass filters were set to 250 Hz and 0.016 Hz, respectively.

When we applied Urbanowicz and Holyst's method and our proposed method to the EEG signals, we used an analysis window with 1500 points, shifting along the time axis every 30 points [see Figs. 2.7(b) and 2.7(c)]. No preprocessing was performed.

By applying the proposed method, we found that the difference between the eyes-open and eyes-closed brain states becomes evident [see Fig. 2.7(c)]. Analysis of the 63 time series of the EEG signals showed that the TSD of electrode Fp2 can be used to robustly discriminate between the eyes-open and eyes-closed states [please see detailed TSD analysis results in Appendix D]. With respect to each subject, the Wilcoxon rank sum test was applied to two datasets: TSDs (11400 points) of the eyes-open period and TSDs (11400 points) of the eyes-closed period, both of which include 10 trials; 1140 TSDs were calculated in the eyes-open or eyes-closed periods for each trial. The results showed that the median of the eyes-open dataset was significantly greater than that of the eyes-closed dataset ($P < 0.0001$ for two subjects); medians of the eyes-open and eyes-closed datasets were 1.24 and 1.18 for subject 1 and 1.19 and 1.16 for subject 2, respectively. The TSD is less influenced by disturbances such as eye movement [see Fig. 2.7(c)] so that the TSD of each state of the eyes-open and eyes-closed is temporally stable, i.e., if we set an appropriate threshold value, each state can be definitely distinguished. In contrast, Urbanowicz and Holyst's method did not clearly discriminate between the eyes-open and eyes-closed states [see Fig. 2.7(b)]. The variance of the time series also differed between the eyes-open and eyes-closed states [see Fig. 2.7(d)], where an analysis window similar to those applied to Figs. 2.7(b) and 2.7(c), was used for dynamically obtaining the variance, but the difference between the states was smaller than that using the TSD [see Fig. 2.7(c)]. Moreover, the variance is very sensitive to disturbances so that the time series of the variance fluctuates over a wide range of amplitudes. Thus, the proposed method can estimate the level of the dynamical noise more reliably and distinguish the eyes-open and eyes-closed states robustly.

2.6 Discussions

A novel dimension called TSD, for estimating the level of dynamical noise perturbing in time series, observed through stochastic dynamical systems has been proposed. We have defined the dynamical noise in the sense of the Wiener process, and based on this definition, it has been validated whether a monotonic relationship between the TSD and the dynamical noise level is achieved among four specific systems [see Section 2.4.3]. The TSD may be a

well-defined dimension because it has been derived directly from the scaling property [see Fig. 2.3] of the conventional Higuchi's fractal dimension so that the TSD does not require the power law and is applicable to non-fractal signals. Furthermore, the applicability of the TSD to real time-series data has been demonstrated with the application of the proposed method to human EEG signals. The obtained results have shown that the estimated TSD temporally changes due to visual inputs [see Fig. 2.7(c)].

Possibly due to the noise-induced order [41], the variance of the eyes-opened period was low compared to that of the eyes-closed period [see Fig. 2.7(d)]. In particular, the dynamical neural noise caused by the light stimulus may play a role in realizing the noise-induced order. Typical time series [see Figs. 2.7(e) and 2.7(f)] of the eyes-open and eyes-closed states have implied that the TSD reflects the relative dominance ratio between the deterministic and stochastic components. In the case of the eyes-open state [see Fig. 2.7(e)], the TSD was larger corresponding with miniature fluctuations in the EEG data. In the case of the eyes-closed state [see Fig. 2.7(f)], the TSD was smaller corresponding with large fluctuations in the EEG data.

The proposed TSD may also work as an effective indicator of dynamical noise even for transient time series data (containing transient components). We have supported our claim with the numerical analysis presented in Section 2.4.3. In particular, short time series with the length $L_{\rm seg}(0, \Delta t) = 100$, obtained from four different systems, have shown a similar monotonically increasing property of the TSD with respect to the dynamical noise level, as depicted in Fig. 2.4. Thus, the present method may be used to analyze time series containing transient behavior.

On the other hand, if one has multivariate time series, especially two time series, one may be able to adjust their monotonic properties so that the universal monotonicity holds for both of them, by changing the length of time series [see Fig. 2.8] or by resampling time series [see Fig. 2.9]. Let us consider the situation that we have two monotonic properties and try to fit these properties with each other. As a particular example, we try to make a monotonic property generated from the harmonic oscillator system, equal to each of monotonic properties generated from the Lorenz system, the Rössler system, and the coupled Hindmarsh-Rose neuronal system. Here, each system is assumed to be affected by dynamical noise with level 0.1. The lengths of the time series associated with these four systems have been fixed to 4313, 179, 563, and 318 points, respectively so that the beginning of this simulation has been equivalent to Fig. A.1(a) in Appendix A; these lengths correspond to $\lfloor c^*/\Delta t \rfloor$ derived from two upper bounds $\epsilon_1 = 2.5$ and $\epsilon_2 = 0.06$ [see Eqs. (2.8) and (2.9)], where $\lfloor \cdot \rfloor$ denotes the rounding down. As the length $L_{\rm seg}(0, \Delta t) = 4313$ of the time series decreases, the root mean square (RMS) errors [see Eq. (A.1)] between two systems also decrease, as shown in Fig. 2.8. Among three pairs of two systems (i.e. (i) the harmonic oscillator system vs. the Lorenz system, (ii) the harmonic oscillator system vs. the Rössler system, and (iii) the harmonic oscillator system vs. the coupled Hindmarsh-Rose neuronal system), when we change the length of time

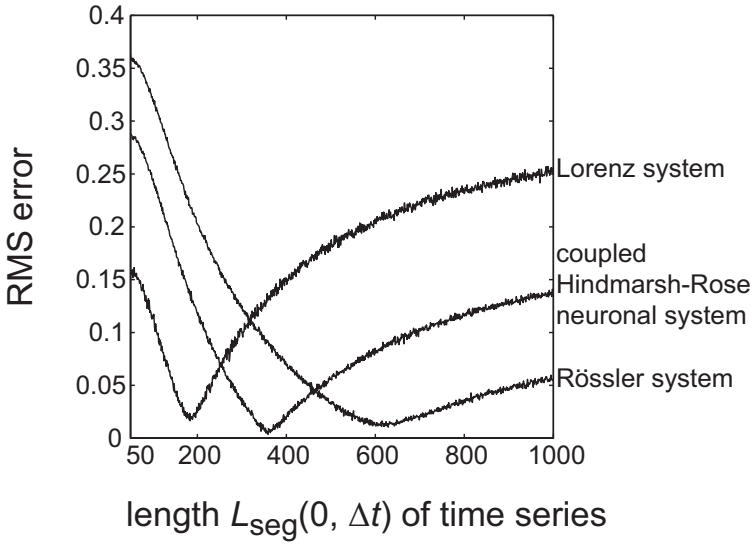

Figure 2.8. Adjustments of the length of short time series to work the systems universally. A case that the monotonic property of (I) the harmonic oscillator system approaches those of other three systems: (II) the Lorenz system, (III) the Rössler system, and (IV) the coupled Hindmarsh-Rose neuronal system. Clearly, the minimal values of the RMS errors correspond to $L_{\rm seg}(0, \Delta t) = 184$ for system (II), $L_{\rm seg}(0, \Delta t) = 629$ for system (III), and $L_{\rm seg}(0, \Delta t) = 359$ for system (IV), respectively.

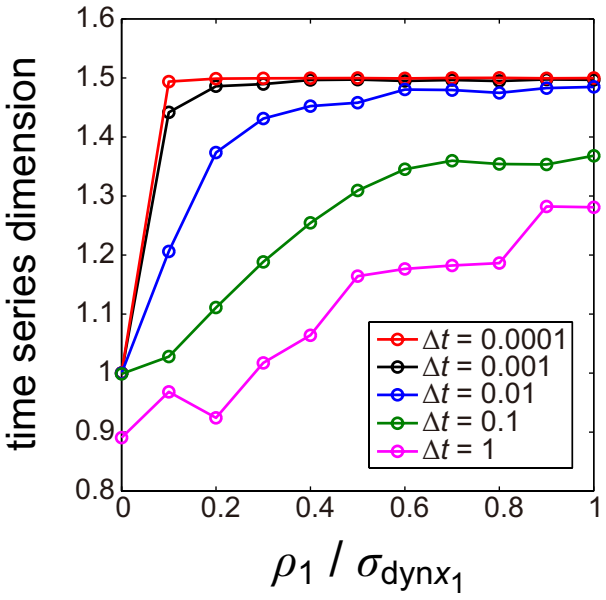

Figure 2.9. The effect of the sampling time Δt on the monotonic property corresponding to the harmonic oscillator system. As Δt decreases, the time series dimension (TSD) becomes constant along with the noise level larger than 0. As Δt increases, the monotonic property changes, but the property still holds even if $\Delta t = 1$.

series associated with the harmonic oscillator system from 4313 to 50, the RMS errors indicate very small values (less than 0.05) at certain length of time series, see Fig. 2.8. The lengths corresponding to the minimal values of the RMS errors are 184, 629, and 359 for pairs of systems (i) through (iii), respectively. Thus, we can flexibly control the monotonic properties to work them universally by changing the length of time series.

Finally, we discuss the case of adjusting the monotonic property of a system by re-sampling the corresponding time series data. We have simulated 100 short time series of $\{X_{\rm obs}(t)\}$ with the lengths of $L_{\rm seg}(0, \Delta t) = 4313$, as well as Fig. 8, corresponding to the harmonic oscillator system affected by dynamical noise. Five monotonic properties, each of which corresponds to the sampling time 0.0001, 0.001, 0.01, 0.1, and 1 of Δt, respectively, have been generated. At this point it is worth to remember that the TSD actually depends on Δt as well as $\vec{\rho}$, although until now we have considered a fixed sampling time $\Delta t = 0.001$. Now, consider the monotonic property obtained by using a very small sampling time, namely $\Delta t = 0.0001$. This property almost does not depend on the noise level except at $\vec{\rho} = \vec{0}$, and then the resulting TSD always indicates around 1.5 so that the property cannot work as an indicator of the dynamical noise level. Next, suppose that we resample the time series, which was sampled at $\Delta t = 0.001$, by new sampling times of 0.01, 0.1, and 1, respectively. As Δt increases, the monotonic property changes; that is, the slope of the monotonically increasing behavior gradually decreases. If Δt is a very large value for example $\Delta t = 1$, the monotonic behavior tends to be unstable, but the increasing property still holds. Thus, along with the resampled multivariate time series data in a plausible way, the resulting TSDs may work universally.

2.7 Conclusions

A method, based on the TSD, for detecting changes in the level of the dynamical noise in stochastic dynamical systems has been proposed. It has been shown that the TSD has a monotonic relationship with the level of dynamical noise. This novel TSD is an extended or, rather, a flexible version of the conventional Higuchi's fractal dimension because the TSD can handle any stochastic dynamical system, including non-fractal signals. Furthermore, a theory of the TSD has been presented for the case of linear stochastic dynamical systems. This theory should be extended to cover more general systems, such as systems affected by dynamical noise as well as observational noise. In addition, the method has been applied to EEG data, in which the TSD has shown robustness to sudden disturbances. We believe that the proposed method may help us understand the behavior of various complex dynamical systems, including the brain.

Chapter 3

Analysis on signals composed of deterministic slow and fast oscillations

3.1 Introduction

Neurons in the brain process information through diverse neural dynamics emergent from interaction among neurons via synapses. The relation of the underlying structure of neural network to its dynamics, such as oscillatory or synchronized activity, largely remains to be explored.

A variety of oscillatory phenomena in the brain have been studied with the local field potential and an electroencephalogram. The recorded neural activity can provide useful indices of distinctive brain functions, which indicates a possibility that the oscillatory phenomena correlate with brain functions [3]. Additionally, the recorded neural activity represents various types of oscillatory wave forms and can be categorized according to the frequency, whose plural bands can temporally coexist in the same or different brain regions [47, 45]. Cross-frequency coupling emerges when the slow and fast oscillatory components interact with each other. Among the sorted frequency bands, neighboring bands recorded in the same brain region typically differ in the brain function [43, 44, 45, 46]. A relationship between the slow and fast oscillations can be explained by the power spectrum, in which the power is inversely proportional to the frequency [48]. Such a relation between the power and the oscillatory frequency implies that spatially widespread slow oscillations modulate the local neural activity [47, 45, 49].

The mechanism underlying oscillatory phenomena is based on inhomogeneity of networks composed of multiple types of neurons. In the brain, there exist at least two kinds of neurons, namely, excitatory and inhibitory neurons, which exhibit different response properties [50]. In particular, an excitatory neuron shows slow firing whereas an inhibitory neuron shows fast firing.

Another fundamental structure for the investigation of oscillatory phenomena is synaptic connectivity. Synapses that exhibit rapid changes in the coupling strength among neurons with a short-term plasticity mechanism are called dynamic synapses [51, 52, 53, 54].

Two types of dynamic synapses exist: short-term depression and facilitation synapses. Both of these are characterized with transiently decreasing releasable neurotransmitters and with transiently increasing calcium concentration in the presynaptic terminal, where synaptic transmission efficacy decreases or increases; this variation is determined by the ratio of two time constants associated with recovery from the transient decrease or increase [52, 53]. The distribution of dynamic synapses in the brain differs among brain regions; for example, a lot of depression synapses are within the parietal lobe, while facilitation synapses are within the prefrontal lobe [54].

Properties on neural network models involving dynamic synapses have been intensively investigated. Synaptic facilitation enhances the working memory function [55]. Furthermore, the combination of depression and facilitation synapses contributes to flexible information representation [56]. Stochastic neural network models and their corresponding mean field models have been effectively used to consider the properties of neural networks, including those of dynamic synapses [57, 22]. Synaptic depression contributes to the destabilization of network activity, the generation of an oscillatory state, and spontaneous state transitions among multiple patterns in an associative memory network [58].

In this study, we have hypothesized that cross-frequency coupling is generated by the interaction between the excitatory and inhibitory networks, where excitatory and inhibitory neurons generate the slow and fast oscillations, respectively [Fig. 3.1(a)]. We therefore focus on a stochastic model composed of excitatory and inhibitory neural networks and dynamic synapses. Furthermore, the present model considers the decay process of the synaptic current. We analyze a macroscopic mean field model reproducing the overall network dynamics associated with the stochastic model. By adjustments of parameters specifying properties on synaptic currents and dynamic synapses, rich bifurcation structures of the network dynamics are expected to be found. In the following, first, we describe a stochastic network including dynamic synapses. Then, we get a mean field model which represents macroscopic properties of neurons. Subsequently, we investigate the bifurcation structures in the present model, and demonstrate various solutions in the dynamical systems of not only the excitatory or inhibitory network but also the inhomogeneous network composed of both excitatory and inhibitory neurons. The final part discusses the consequence of the bifurcation analysis.

3.2 Method

This section consists of three parts. The first part describes the short-term plasticity. The second part explains the stochastic model, which is formulated using an inhomogeneous network with dynamic synapses. The third part introduces a mean field theory in which the stochastic model is converted to the corresponding microscopic and macroscopic mean field models; the microscopic model is implemented for approximating the stochastic properties, where the noise average is introduced; the macroscopic model is used for elucidating the comprehensive properties of the present model.

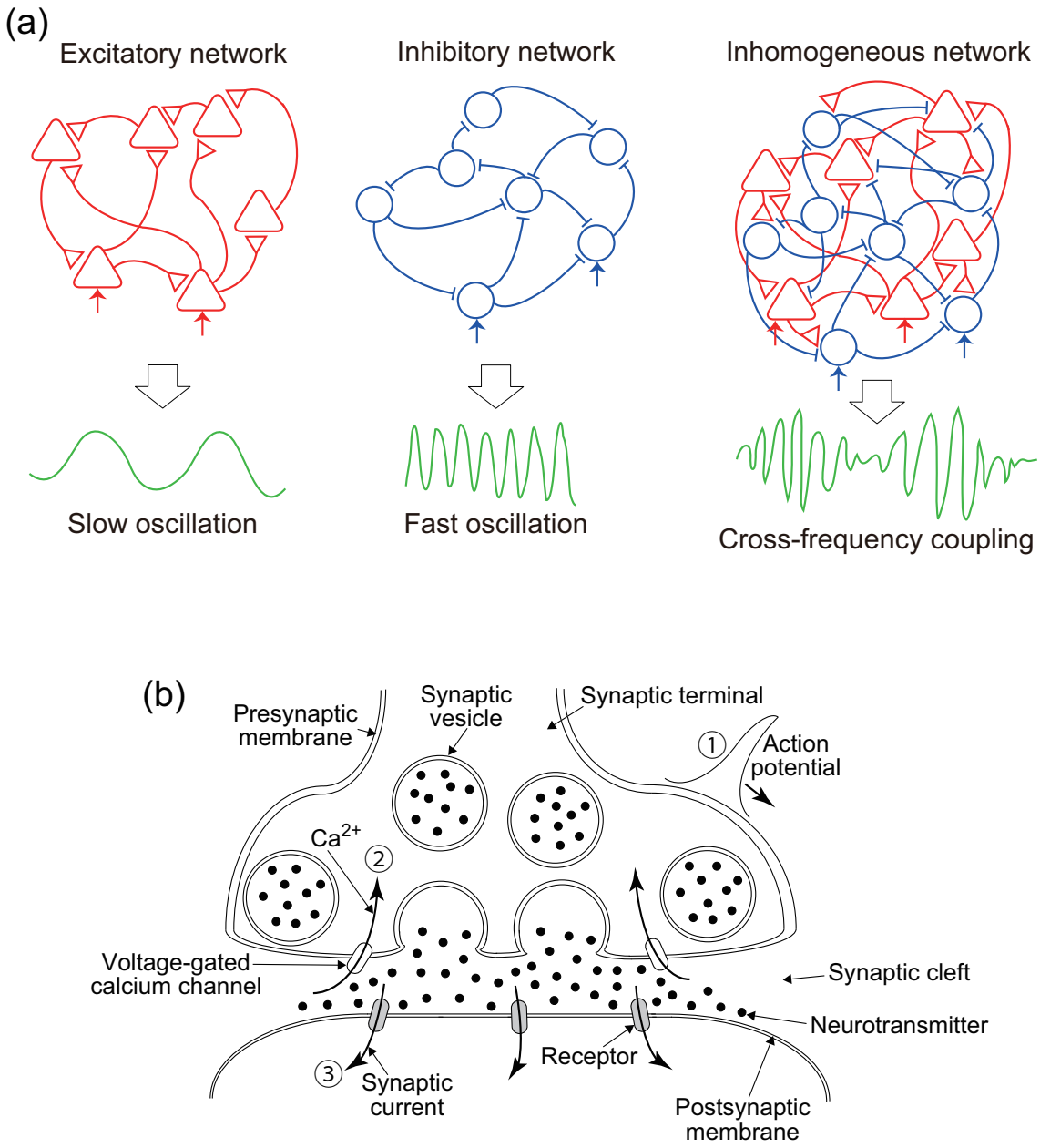

Figure 3.1. A hypothesis of emergent dynamics considered in the present model. (a) Cross-frequency coupling, in which two distinctive frequency components coexist, can emerge in the inhomogeneous network with dynamic synapses. The three types of networks, excitatory, inhibitory, and inhomogeneous networks, have been investigated with the assumption that neurons are recurrently and fully connected with each other. (b) Short-term plasticity. The synaptic current is evoked with transiently decreasing releasable neurotransmitters and with transiently increasing calcium concentration in the synaptic terminal. The emergent dynamics of these two transient responses are due to the action potentials of presynaptic neurons. In this study, networks with depression-dominant synapses have been investigated.

3.2.1 Mechanism of synaptic transmission

Here, we describe the short-term plasticity, which is one of the key components of the present model [Fig. 3.1(b)]. First, after the membrane potential exceeds a certain threshold value, the action potential is generated and reaches a synaptic terminal. Second, voltage-gated calcium channels open, and the calcium ions flow through channels into the terminal. Third, neurotransmitters within the vesicles are released in the synaptic cleft owing to the concatenation of vesicles and the membrane. Released neurotransmitters bind to the receptors, and then a synaptic current is induced in the connected neurons. The amplitude of the synaptic current decays with a certain time constant.

When a lot of action potentials appear in a presynapse within a short period, efficacy of the synaptic transmission transiently decreases or increases. Finally, the synaptic vesicles are retrieved and the neurotransmitters are restored in the reusable synaptic vesicles [51, 52, 53, 54].

3.2.2 Model

We investigate a discrete-time network model composed of the excitatory (E) and the inhibitory (I) subnetworks, which consist of $N_{\rm E}$ excitatory and $N_{\rm I}$ inhibitory neurons, respectively. The ith neuron belonging to network $\xi(\xi\in\{{\rm E},{\rm I}\})$ is denoted by $s_i^\xi(t)$. This variable indicates either the quiescent regime $[s_i^\xi(t)=0]$ or the activated regime $[s_i^\xi(t)=1]$. The state is updated in accordance with the following dynamics:

$$\begin{aligned} {\rm Prob}[s_i^\xi(t+1)=1] &= g_{\beta^\xi}[h_i^\xi(t)], & (3.1)\\ g_{\beta^\xi}[h_i^\xi(t)] &= \frac{1}{2}\{1+\tanh[\beta^\xi h_i^\xi(t)]\}, & (3.2) \end{aligned}$$

where $h_i^\xi(t)=\sum_{j\neq i}^{N_\xi}[J_{ij}^{\xi\xi}a_j^\xi(t)]+\sum_{j=1}^{N_\eta}[J_{ij}^{\xi\eta}a_j^\eta(t)]+I^\xi$ with $\eta\in\{{\rm E},{\rm I}|\eta\neq\xi\}$. The variables $h_i^\xi(t)$ and $a_j^\xi(t)$ represent the total input for the ith neuron on network ξ and the synaptic activity with short-term plasticity, respectively; $1/\beta^\xi=T^\xi$ denotes the noise intensity; $J_{ij}^{\xi\xi}$, $J_{ij}^{\xi\eta}$, and I^ξ indicate the connection from the jth neuron to the ith neuron on network ξ (coupling within a subnetwork), the connection from the jth neuron on network η to the ith neuron on network ξ (coupling between subnetworks), and the external input, respectively.

The short-term plasticity can be modeled by use of the synaptic activity $a_i^\xi(t)$ and two variables, $x_i^\xi(t)$ and $u_i^\xi(t)$. The synaptic activity $a_i^\xi(t)$ increases with the presynaptic neural activity. This increase is proportional to the product of $x_i^\xi(t)$ and $u_i^\xi(t)$, which represents the synaptic transmission efficacy [52, 55, 59]. If there is no synaptic activation, $a_i^\xi(t)$ converges to its steady state $a_i^\xi(t)=0$ with a time constant $\tau_{\rm a}^\xi$. The ratio $x_i^\xi(t)$ of releasable neurotransmitters decreases with the increase of presynaptic activation. Then, $x_i^\xi(t)$ returns to the steady state $x_i^\xi(t)=1$ with $\tau_{\rm R}^\xi$. The calcium concentration $u_i^\xi(t)$

changes depending on the presynaptic activity and returns to the steady state $u_i^\xi(t) = U_{\rm se}^\xi$ with $\tau_{\rm F}^\xi$. The dynamics can be summarized as follows:

$$a_i^\xi(t+1) = a_i^\xi(t) - \frac{a_i^\xi(t)}{\tau_{\rm a}^\xi} + s_i^\xi(t)x_i^\xi(t)u_i^\xi(t)/U_{\rm se}^\xi, \tag{3.3}$$

$$x_i^\xi(t+1) = x_i^\xi(t) + \frac{1-x_i^\xi(t)}{\tau_{\rm R}^\xi} - s_i^\xi(t)x_i^\xi(t)u_i^\xi(t), \tag{3.4}$$

$$u_i^\xi(t+1) = u_i^\xi(t) + \frac{U_{\rm se}^\xi - u_i^\xi(t)}{\tau_{\rm F}^\xi} + U_{\rm se}^\xi(1-u_i^\xi(t))s_i^\xi(t). \tag{3.5}$$

3.2.3 Mean field theory

The dynamic mean field model was developed according to the following two steps. The first step is the derivation of a microscopic mean field model. The second step is the development of a macroscopic mean field model.

First, Eq. (3.1) and Eq. (3.2) are converted to the following forms:

$$\langle s_i^\xi(t+1)\rangle = g_{\beta\varepsilon}[\langle h_i^\xi(t)\rangle], \tag{3.6}$$

$$\langle h_i^\xi(t)\rangle = \sum_{j\neq i}^{N_\xi}\left[J_{ij}^{\xi\xi}\langle a_j^\xi(t)\rangle\right] + \sum_{j=1}^{N_\eta}\left[J_{ij}^{\xi\eta}\langle a_j^\eta(t)\rangle\right] + I^\xi, \tag{3.7}$$

where the notation $\langle\cdot\rangle$ indicates the noise average. Similarly, the following equations, corresponding to Eqs. (3.3) to (3.5), are obtained:

$$\langle a_i^\xi(t+1)\rangle = \langle a_i^\xi(t)\rangle - \frac{\langle a_i^\xi(t)\rangle}{\tau_{\rm a}^\xi} + \langle s_i^\xi(t)x_i^\xi(t)u_i^\xi(t)\rangle/U_{\rm se}^\xi, \tag{3.8}$$

$$\langle x_i^\xi(t+1)\rangle = \langle x_i^\xi(t)\rangle + \frac{1-\langle x_i^\xi(t)\rangle}{\tau_{\rm R}^\xi} - \langle s_i^\xi(t)x_i^\xi(t)u_i^\xi(t)\rangle, \tag{3.9}$$

$$\langle u_i^\xi(t+1)\rangle = \langle u_i^\xi(t)\rangle + \frac{U_{\rm se}^\xi - \langle u_i^\xi(t)\rangle}{\tau_{\rm F}^\xi} + U_{\rm se}^\xi\langle(1-u_i^\xi(t))s_i^\xi(t)\rangle. \tag{3.10}$$

Here, we have assumed that $J_{ij}^{\xi\xi}$ and $J_{ij}^{\xi\eta}$ are of the orders of $1/N_\xi$ and $1/N_\eta$, respectively, so that the correlation between $s_i^\xi(t)$ and $x_i^\xi(t)$ is negligible when $N_\xi\to\infty$ [57] . The correlation between $s_i^\xi(t)$ and $u_i^\xi(t)$ is also ignored as $N_\xi\to\infty$. Furthermore, in the previous study, it was found that the correlation between $x_i^\xi(t)$ and $u_i^\xi(t)$ is negligible when the number of neurons is large enough [22], while it has been reported that the independence between $x_i^\xi(t)$ and $u_i^\xi(t)$ is maintained if there is no facilitation [60]. Consequently, we assume the following:

$$\langle s_i^\xi(t)x_i^\xi(t)u_i^\xi(t)\rangle = \langle s_i^\xi(t)\rangle\langle x_i^\xi(t)\rangle\langle u_i^\xi(t)\rangle, \tag{3.11}$$

$$\langle s_i^\xi(t)u_i^\xi(t)\rangle = \langle s_i^\xi(t)\rangle\langle u_i^\xi(t)\rangle. \tag{3.12}$$

As shown in the Results section, the dynamic mean field model is consistent with the simulation on the stochastic model. By using the above relations, we get the following microscopic mean field model:

$$m_i^\xi(t+1) = g_{\beta\xi}\left[\sum_{j\neq i}^{N_\xi}\left(J_{ij}^{\xi\xi}A_j^\xi(t)\right)+\sum_{j=1}^{N_\eta}\left(J_{ij}^{\xi\eta}A_j^\eta(t)\right)+I^\xi\right], \tag{3.13}$$

$$A_i^\xi(t+1) = A_i^\xi(t)-\frac{A_i^\xi(t)}{\tau_{\rm a}^\xi}+m_i^\xi(t)X_i^\xi(t)U_i^\xi(t)/U_{\rm se}^\xi, \tag{3.14}$$

$$X_i^\xi(t+1) = X_i^\xi(t)+\frac{1-X_i^\xi(t)}{\tau_{\rm R}^\xi}-m_i^\xi(t)X_i^\xi(t)U_i^\xi(t), \tag{3.15}$$

$$U_i^\xi(t+1) = U_i^\xi(t)+\frac{U_{\rm se}^\xi-U_i^\xi(t)}{\tau_{\rm F}^\xi}+U_{\rm se}^\xi(1-U_i^\xi(t))m_i^\xi(t), \tag{3.16}$$

where we have set $m_i^\xi(t)\equiv\langle s_i^\xi(t)\rangle$, $A_i^\xi(t)\equiv\langle a_i^\xi(t)\rangle$, $X_i^\xi(t)\equiv\langle x_i^\xi(t)\rangle$, and $U_i^\xi(t)\equiv\langle u_i^\xi(t)\rangle$.

We represent the fixed point as $\bar m_i^\xi$, $\bar A_i^\xi$, $\bar X_i^\xi$, and $\bar U_i^\xi$. The fixed point for Eqs. (3.14) to (3.16) is obtained as follows:

$$\bar A_i^\xi = \frac{\tau_{\rm a}^\xi\bar U_i^\xi\bar m_i^\xi\bar X_i^\xi}{U_{\rm se}^\xi}, \tag{3.17}$$

$$\bar X_i^\xi = \frac{1}{1+\tau_{\rm R}^\xi\bar U_i^\xi\bar m_i^\xi}, \tag{3.18}$$

$$\bar U_i^\xi = \frac{U_{\rm se}^\xi(1+\tau_{\rm F}^\xi\bar m_i^\xi)}{1+\tau_{\rm F}^\xi U_{\rm se}^\xi\bar m_i^\xi}. \tag{3.19}$$

Using these equations, we get the fixed point $\bar m_i^\xi$ as follows:

$$\begin{aligned}\bar m_i^\xi = g_{\beta\xi}\Bigg[&\sum_{j\neq i}^{N_\xi}J_{ij}^{\xi\xi}\left(\frac{\tau_{\rm a}^\xi\bar m_j^\xi(1+\tau_{\rm F}^\xi\bar m_j^\xi)}{1+(\tau_{\rm F}^\xi+\tau_{\rm R}^\xi)U_{\rm se}^\xi\bar m_j^\xi+U_{\rm se}^\xi\tau_{\rm F}^\xi\tau_{\rm R}^\xi\bar m_j^\xi\bar m_j^\xi}\right)\\ &+\sum_{j=1}^{N_\eta}J_{ij}^{\xi\eta}\left(\frac{\tau_{\rm a}^\eta\bar m_j^\eta(1+\tau_{\rm F}^\eta\bar m_j^\eta)}{1+(\tau_{\rm F}^\eta+\tau_{\rm R}^\eta)U_{\rm se}^\eta\bar m_j^\eta+U_{\rm se}^\eta\tau_{\rm F}^\eta\tau_{\rm R}^\eta\bar m_j^\eta\bar m_j^\eta}\right)+I^\xi\Bigg].\end{aligned} \tag{3.20}$$

We derive the macroscopic mean field model with uniform connections where weights $J_{ij}^{\xi\xi}$ and $J_{ij}^{\xi\eta}$ are given by

$$J_{ij}^{\xi\xi} = \frac{J_0^{\xi\xi}}{N_\xi}, \tag{3.21}$$

$$J_{ij}^{\xi\eta} = \frac{J_0^{\xi\eta}}{N_\eta}. \tag{3.22}$$

Here $J_0^{\xi\xi}$ and $J_0^{\xi\eta}$ are the parameters specifying the strength of the uniform connections. Because of this uniformity of the synaptic connections, the variables m_i^ξ, A_i^ξ, X_i^ξ, and U_i^ξ can be substituted with their averages $m_0^\xi=(1/N_\xi)\sum_{i=1}^{N_\xi}m_i^\xi$, $A_0^\xi=(1/N_\xi)\sum_{i=1}^{N_\xi}A_i^\xi$,

$X_0^\xi = (1/N_\xi)\sum_{i=1}^{N_\xi} X_i^\xi$, and $U_0^\xi = (1/N_\xi)\sum_{i=1}^{N_\xi} U_i^\xi$. The macroscopic mean field model for the network with uniform connections is given by

$$
\begin{aligned}
m_0^\xi(t+1) &= F_m^\xi(\Omega(t)), && (3.23)\\
A_0^\xi(t+1) &= F_A^\xi(\Omega(t)), && (3.24)\\
X_0^\xi(t+1) &= F_X^\xi(\Omega(t)), && (3.25)\\
U_0^\xi(t+1) &= F_U^\xi(\Omega(t)), && (3.26)
\end{aligned}
$$

where

$$
\begin{aligned}
F_m^\xi(\Omega(t)) &= g_{\beta\xi}\left[J_0^{\xi\xi}A^\xi + J_0^{\xi\eta}A^\eta + I^\xi\right], && (3.27)\\
F_A^\xi(\Omega(t)) &= A^\xi - \frac{A^\xi}{\tau_{\mathrm{a}}^\xi} + m^\xi X^\xi U^\xi / U_{\mathrm{se}}^\xi, && (3.28)\\
F_X^\xi(\Omega(t)) &= X^\xi + \frac{1-X^\xi}{\tau_{\mathrm{R}}^\xi} - m^\xi X^\xi U^\xi, && (3.29)\\
F_U^\xi(\Omega(t)) &= U^\xi + \frac{U_{\mathrm{se}}^\xi - U^\xi}{\tau_{\mathrm{F}}^\xi} + U_{\mathrm{se}}^\xi(1-U^\xi)m^\xi, && (3.30)
\end{aligned}
$$

with the state vector $\Omega(t)$ defined as

$$
\Omega(t) = \left[m_0^{\mathrm{E}}(t), m_0^{\mathrm{I}}(t), A_0^{\mathrm{E}}(t), A_0^{\mathrm{I}}(t), X_0^{\mathrm{E}}(t), X_0^{\mathrm{I}}(t), U_0^{\mathrm{E}}(t), U_0^{\mathrm{I}}(t)\right]^{\mathrm{T}}. \quad (3.31)
$$

By modifying Eq. (3.20), the fixed point for the macroscopic mean field model can be calculated as follows:

$$
\begin{aligned}
\bar{m}^{\mathrm{E}} &= f_{\mathrm{E}}(\bar{m}^{\mathrm{E}}, \bar{m}^{\mathrm{I}}), && (3.32)\\
\bar{m}^{\mathrm{I}} &= f_{\mathrm{I}}(\bar{m}^{\mathrm{I}}, \bar{m}^{\mathrm{E}}), && (3.33)
\end{aligned}
$$

where

$$
\begin{aligned}
f_\xi(\bar{m}^\xi, \bar{m}^\eta) &= g_{\beta\xi}\left[J_0^{\xi\xi}\left(\frac{\tau_{\mathrm{a}}^\xi \bar{m}^\xi(1+\tau_{\mathrm{F}}^\xi\bar{m}^\xi)}{1+(\tau_{\mathrm{F}}^\xi+\tau_{\mathrm{R}}^\xi)U_{\mathrm{se}}^\xi\bar{m}^\xi + U_{\mathrm{se}}^\xi\tau_{\mathrm{F}}^\xi\tau_{\mathrm{R}}^\xi\bar{m}^\xi\bar{m}^\xi}\right)\right.\\
&+ \left. J_0^{\xi\eta}\left(\frac{\tau_{\mathrm{a}}^\eta \bar{m}^\eta(1+\tau_{\mathrm{F}}^\eta\bar{m}^\eta)}{1+(\tau_{\mathrm{F}}^\eta+\tau_{\mathrm{R}}^\eta)U_{\mathrm{se}}^\eta\bar{m}^\eta + U_{\mathrm{se}}^\eta\tau_{\mathrm{F}}^\eta\tau_{\mathrm{R}}^\eta\bar{m}^\eta\bar{m}^\eta}\right) + I^\xi\right]. \quad (3.34)
\end{aligned}
$$

After solving the above equations simultaneously, we get the steady state $\bar{m}_0^{\mathrm{E}}$ and $\bar{m}_0^{\mathrm{I}}$. By substituting $\bar{m}_0^{\mathrm{E}}$ and $\bar{m}_0^{\mathrm{I}}$ into the following steady state equations

$$
\begin{aligned}
\bar{A}_0^\xi &= \frac{\tau_{\mathrm{a}}^\xi \bar{U}_0^\xi \bar{m}_0^\xi \bar{X}_0^\xi}{U_{\mathrm{se}}^\xi}, && (3.35)\\
\bar{X}_0^\xi &= \frac{1}{1+\tau_{\mathrm{R}}^\xi \bar{U}_0^\xi \bar{m}_0^\xi}, && (3.36)\\
\bar{U}_0^\xi &= \frac{U_{\mathrm{se}}^\xi(1+\tau_{\mathrm{F}}^\xi\bar{m}_0^\xi)}{1+\tau_{\mathrm{F}}^\xi U_{\mathrm{se}}^\xi\bar{m}_0^\xi}, && (3.37)
\end{aligned}
$$

we obtain the steady state $\bar{A}_0^\xi$, $\bar{X}_0^\xi$, and $\bar{U}_0^\xi$.

Here, we investigate the fixed point by considering small deviations $\delta m_0^\xi(t)$, $\delta A_0^\xi(t)$, $\delta X_0^\xi(t)$, and $\delta U_0^\xi(t)$ around the fixed point as follows:

$$m_0^\xi(t) = \bar{m}_0^\xi + \delta m_0^\xi(t), \tag{3.38}$$
$$A_0^\xi(t) = \bar{A}_0^\xi + \delta A_0^\xi(t), \tag{3.39}$$
$$X_0^\xi(t) = \bar{X}_0^\xi + \delta X_0^\xi(t), \tag{3.40}$$
$$U_0^\xi(t) = \bar{U}_0^\xi + \delta U_0^\xi(t). \tag{3.41}$$

By neglecting the higher order components, we get the following locally linearized equation:

$$\begin{pmatrix} \delta m_0^{\mathrm{E}}(t+1) \\ \delta A_0^{\mathrm{E}}(t+1) \\ \delta X_0^{\mathrm{E}}(t+1) \\ \delta U_0^{\mathrm{E}}(t+1) \\ \delta m_0^{\mathrm{I}}(t+1) \\ \delta A_0^{\mathrm{I}}(t+1) \\ \delta X_0^{\mathrm{I}}(t+1) \\ \delta U_0^{\mathrm{I}}(t+1) \end{pmatrix} = K \begin{pmatrix} \delta m_0^{\mathrm{E}}(t) \\ \delta A_0^{\mathrm{E}}(t) \\ \delta X_0^{\mathrm{E}}(t) \\ \delta U_0^{\mathrm{E}}(t) \\ \delta m_0^{\mathrm{I}}(t) \\ \delta A_0^{\mathrm{I}}(t) \\ \delta X_0^{\mathrm{I}}(t) \\ \delta U_0^{\mathrm{I}}(t) \end{pmatrix}, \tag{3.42}$$

where K is the Jacobian matrix

$$K = \begin{pmatrix} K_{mm}^{\mathrm{EE}} & K_{mA}^{\mathrm{EE}} & K_{mX}^{\mathrm{EE}} & K_{mU}^{\mathrm{EE}} & K_{mm}^{\mathrm{EI}} & K_{mA}^{\mathrm{EI}} & K_{mX}^{\mathrm{EI}} & K_{mU}^{\mathrm{EI}} \\ K_{Am}^{\mathrm{EE}} & K_{AA}^{\mathrm{EE}} & K_{AX}^{\mathrm{EE}} & K_{AU}^{\mathrm{EE}} & K_{Am}^{\mathrm{EI}} & K_{AA}^{\mathrm{EI}} & K_{AX}^{\mathrm{EI}} & K_{AU}^{\mathrm{EI}} \\ K_{Xm}^{\mathrm{EE}} & K_{XA}^{\mathrm{EE}} & K_{XX}^{\mathrm{EE}} & K_{XU}^{\mathrm{EE}} & K_{Xm}^{\mathrm{EI}} & K_{XA}^{\mathrm{EI}} & K_{XX}^{\mathrm{EI}} & K_{XU}^{\mathrm{EI}} \\ K_{Um}^{\mathrm{EE}} & K_{UA}^{\mathrm{EE}} & K_{UX}^{\mathrm{EE}} & K_{UU}^{\mathrm{EE}} & K_{Um}^{\mathrm{EI}} & K_{UA}^{\mathrm{EI}} & K_{UX}^{\mathrm{EI}} & K_{UU}^{\mathrm{EI}} \\ K_{mm}^{\mathrm{IE}} & K_{mA}^{\mathrm{IE}} & K_{mX}^{\mathrm{IE}} & K_{mU}^{\mathrm{IE}} & K_{mm}^{\mathrm{II}} & K_{mA}^{\mathrm{II}} & K_{mX}^{\mathrm{II}} & K_{mU}^{\mathrm{II}} \\ K_{Am}^{\mathrm{IE}} & K_{AA}^{\mathrm{IE}} & K_{AX}^{\mathrm{IE}} & K_{AU}^{\mathrm{IE}} & K_{Am}^{\mathrm{II}} & K_{AA}^{\mathrm{II}} & K_{AX}^{\mathrm{II}} & K_{AU}^{\mathrm{II}} \\ K_{Xm}^{\mathrm{IE}} & K_{XA}^{\mathrm{IE}} & K_{XX}^{\mathrm{IE}} & K_{XU}^{\mathrm{IE}} & K_{Xm}^{\mathrm{II}} & K_{XA}^{\mathrm{II}} & K_{XX}^{\mathrm{II}} & K_{XU}^{\mathrm{II}} \\ K_{Um}^{\mathrm{IE}} & K_{UA}^{\mathrm{IE}} & K_{UX}^{\mathrm{IE}} & K_{UU}^{\mathrm{IE}} & K_{Um}^{\mathrm{II}} & K_{UA}^{\mathrm{II}} & K_{UX}^{\mathrm{II}} & K_{UU}^{\mathrm{II}} \end{pmatrix}, \tag{3.43}$$

and each element of this matrix is given as follows:

$$K_{mA}^{\xi\xi} = \frac{\partial F_m^\xi}{\partial A^\xi} = g'_{\beta^\xi}[h^\xi] J_0^{\xi\xi}, \tag{3.44}$$
$$K_{mA}^{\xi\eta} = \frac{\partial F_m^\xi}{\partial A^\eta} = g'_{\beta^\xi}[h^\xi] J_0^{\xi\eta}, \tag{3.45}$$

where

$$g'_{\beta^\xi}[h^\xi] = \frac{\beta^\xi}{2}[1 - \tanh^2(\beta^\xi h^\xi)], \tag{3.46}$$
$$h^\xi = J_0^{\xi\xi} A^\xi + J_0^{\xi\eta} A^\eta + I^\xi. \tag{3.47}$$

Furthermore, the remaining elements of matrix K are given by

$$K_{Am}^{\xi\xi} = \frac{U^{\xi}X^{\xi}}{U_{\rm se}^{\xi}}, \tag{3.48}$$

$$K_{AX}^{\xi\xi} = \frac{m^{\xi}U^{\xi}}{U_{\rm se}^{\xi}}, \tag{3.49}$$

$$K_{AU}^{\xi\xi} = \frac{m^{\xi}X^{\xi}}{U_{\rm se}^{\xi}}, \tag{3.50}$$

$$K_{AA}^{\xi\xi} = 1 - \frac{1}{\tau_{\rm a}^{\xi}}, \tag{3.51}$$

$$K_{Xm}^{\xi\xi} = -U^{\xi}X^{\xi}, \tag{3.52}$$

$$K_{XX}^{\xi\xi} = \left(1 - \frac{1}{\tau_{\rm R}^{\xi}}\right) - m^{\xi}U^{\xi}, \tag{3.53}$$

$$K_{XU}^{\xi\xi} = -m^{\xi}X^{\xi}, \tag{3.54}$$

$$K_{Um}^{\xi\xi} = U_{\rm se}^{\xi}(1 - U^{\xi}), \tag{3.55}$$

$$K_{UU}^{\xi\xi} = \left(1 - \frac{1}{\tau_{\rm F}^{\xi}}\right) - U_{\rm se}^{\xi}m^{\xi}, \tag{3.56}$$

and the other elements are zeroes. We analyzed the stability of the fixed point using this Jacobian matrix.

3.3 Results

In this section, we analyze a variety of bifurcation structures associated with the present model by regarding $\tau_{\rm a}^{\xi}$, $J_0^{\xi\xi}$, and I^{ξ} as the bifurcation parameters. First, we investigate the excitatory network, in which we have set $J_0^{\rm EI} = 0$ and $J_0^{\rm EE} > 0$, and the inhibitory network, in which we have set $J_0^{\rm IE} = 0$ and $J_0^{\rm II} < 0$. Then, we analyze the network model composed of both excitatory and inhibitory neurons. When examining the above two subnetworks, we omit the superscripts attached to variables and parameters for simplicity. In the following, we analyze the depression-dominant region, namely, $\tau_{\rm R}^{\xi} = 70$ and $\tau_{\rm F}^{\xi} = 6$ with $U_{\rm se}^{\xi} = 0.1$, $T^{\xi} = 0.8$, and $N_{\xi} = 10^4$.

Both the excitatory and inhibitory networks exhibit distinctive oscillatory states, as shown in the (J_0, I) phase diagram [Fig. 3.2(a)]. The oscillatory state on the excitatory network (OSE) changes into the steady state via the Neimark-Sacker (NS) bifurcation when J_0 decreases/increases or I increases from the region of the OSE state. When J_0 decreases and I increases in the region of the steady state, the oscillatory state on the inhibitory network (OSI) is generated by the NS bifurcation. The bifurcation diagrams in Fig. 3.2(b) and Fig. 3.2(c) show the appearance of these oscillatory states via the NS bifurcations from the steady state. The bifurcation diagram with respect to J_0 on $I = -1$ [Fig. 3.2(b)] shows the emergence of the OSE state. The mean neural activity m_0 in the steady state increases with J_0, while the steady state destabilizes via the NS bifurcation at $J_0 = 1.63$,

and then the OSE state appears. Owing to the second NS bifurcation at $J_0 = 3.48$, the OSE state disappears, and the stable steady state reappears. The bifurcation diagram with respect to J_0 on $I = 1$ [Fig. 3.2(c)] shows the appearance of the OSI state. The mean neural activity m_0 in the steady state decreases with decreasing J_0 while the steady state destabilizes via the NS bifurcation at $J_0 = -4.73$, and then the OSI state appears.

The aforementioned bifurcation diagrams with respect to J_0 on $I = -1$ and on $I = 1$ show good agreement with those in the stochastic model [Fig. 3.3(a) and Fig. 3.3(b)].

To quantify the oscillatory frequency, we applied the Fourier transform to the oscillatory time courses, where 4096 time steps were used for the calculation. The frequency of the first typical peak in the derived power spectrum was converted to the corresponding time step, hereby called the 'period'. The oscillation in the inhibitory network tends to be faster than that in the excitatory network. In the parameter region shown in Fig. 3.2(a), the period of the OSI state ranges from 4.99 to 6.00 time steps whereas that of the OSE state ranges from 33.9 to 78.8 time steps.

Figures 3.2(d) and 3.2(e) show the bifurcation structures of the excitatory and inhibitory networks, respectively. Both the OSE and OSI states represent oscillations on the closed curve.

In the excitatory network, the period of the OSE state ranges from 44.0 to 75.9 time steps. The $(\tau_{\rm a}, I)$ phase diagram [Fig. 3.2(d)] shows the distribution of the OSE state. The period increases as $\tau_{\rm a}$ and I decrease. In the inhibitory network, the period of the OSI state ranges from 3.94 to 8.00 time steps. The $(\tau_{\rm a}, I)$ phase diagram [Fig. 3.2(e)] shows that the area of the OSI state expands and the period tends to increase as $\tau_{\rm a}$ and I increase.

The typical OSE and OSI states represent oscillations both in the stochastic model and in the macroscopic mean field model [Fig. 3.4]. The red curves in Fig. 3.4(a) and Fig. 3.4(d) indicate the time courses of the average values of the variables $s_0(t)[= (1/N)\sum_i^N s_i(t)]$, $a_0(t)[= (1/N)\sum_i^N a_i(t)]$, $x_0(t)[= (1/N)\sum_i^N x_i(t)]$, and $u_0(t)[= (1/N)\sum_i^N u_i(t)]$. The OSI state demonstrates a faster oscillation relative to that of the OSE state. The macroscopic mean field model is similar to the stochastic model in the time courses [Fig. 3.4(a) and Fig. 3.4(d)], in the power spectra [Fig. 3.4(b) and Fig. 3.4(e)], and in the orbits in the state space (Fig. 3.4(c) and Fig. 3.4(f)].

Figure 3.5 shows the dynamical structure of a network composed of the above excitatory and inhibitory subnetworks. Here, we use the parameter values corresponding to the typical OSE and OSI states described above; namely, $J_0^{\rm EE} = 2$ and $J_0^{\rm II} = -10$, respectively. The parameter point $(J_0^{\rm EI}, J_0^{\rm IE}) = (0, 0)$ indicates the direct product system composed of the two subnetworks, in which each network independently exists. The $(J_0^{\rm EI}, J_0^{\rm IE})$ phase diagram (Figure 5A) shows the four distinctive types of neural dynamics in the network: the steady state (SS) and an oscillatory state with a single frequency component with a closed curve (OS1C), one with two frequency components with a 2-dimensional torus (OS2T), and one with two frequency components with a closed curve (OS2C). The number of zero-Lyapunov

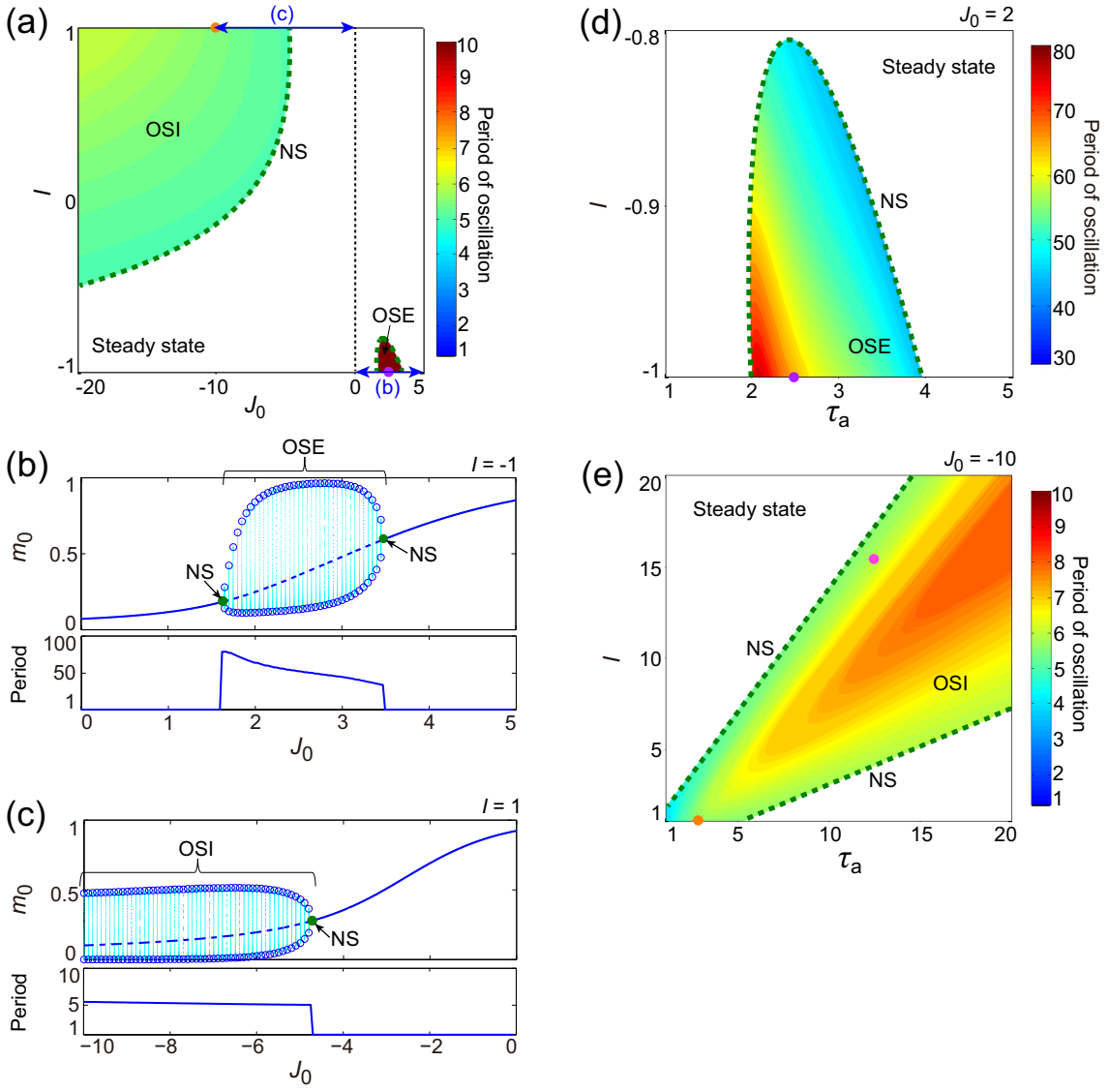

Figure 3.2. A dynamical qualitative change between the excitatory and inhibitory networks with depression synapses. (a) (J_0, I) phase diagram. The colored areas denote two distinctive oscillatory regions, namely, OSE and OSI regions, which appear via the NS bifurcation sets from the region of the steady state (the white region) and can be separated by $J_0 = 0$, indicated by the vertical dotted line. NS bifurcation sets are indicated by the dashed curves. (b) A bifurcation diagram and the corresponding oscillatory period with respect to the positive coupling strength ($J_0 \geq 0$), where a relatively low external input ($I = -1$) acts on the excitatory network. A set of the stable fixed point is indicated by the solid curve and the OSE state is indicated by the open circles with the dotted lines; the dashed curve indicates a set of the unstable fixed point. (c) A bifurcation diagram and the corresponding oscillatory period with respect to the negative coupling strength ($J_0 \leq 0$) for $I = 1$. In panels (b) and (c), the stable steady state and the OSE or OSI state are exchanged via the NS bifurcation points, indicated by the filled circles. (d) (τ_a, I) phase digram for the OSE region in which the coupling strength is positive ($J_0 = 2$). (e) (τ_a, I) phase digram for the OSI region in which the coupling strength is negative ($J_0 = -10$). The oscillatory periods in both the OSE and OSI regions change depending on τ_a and I.

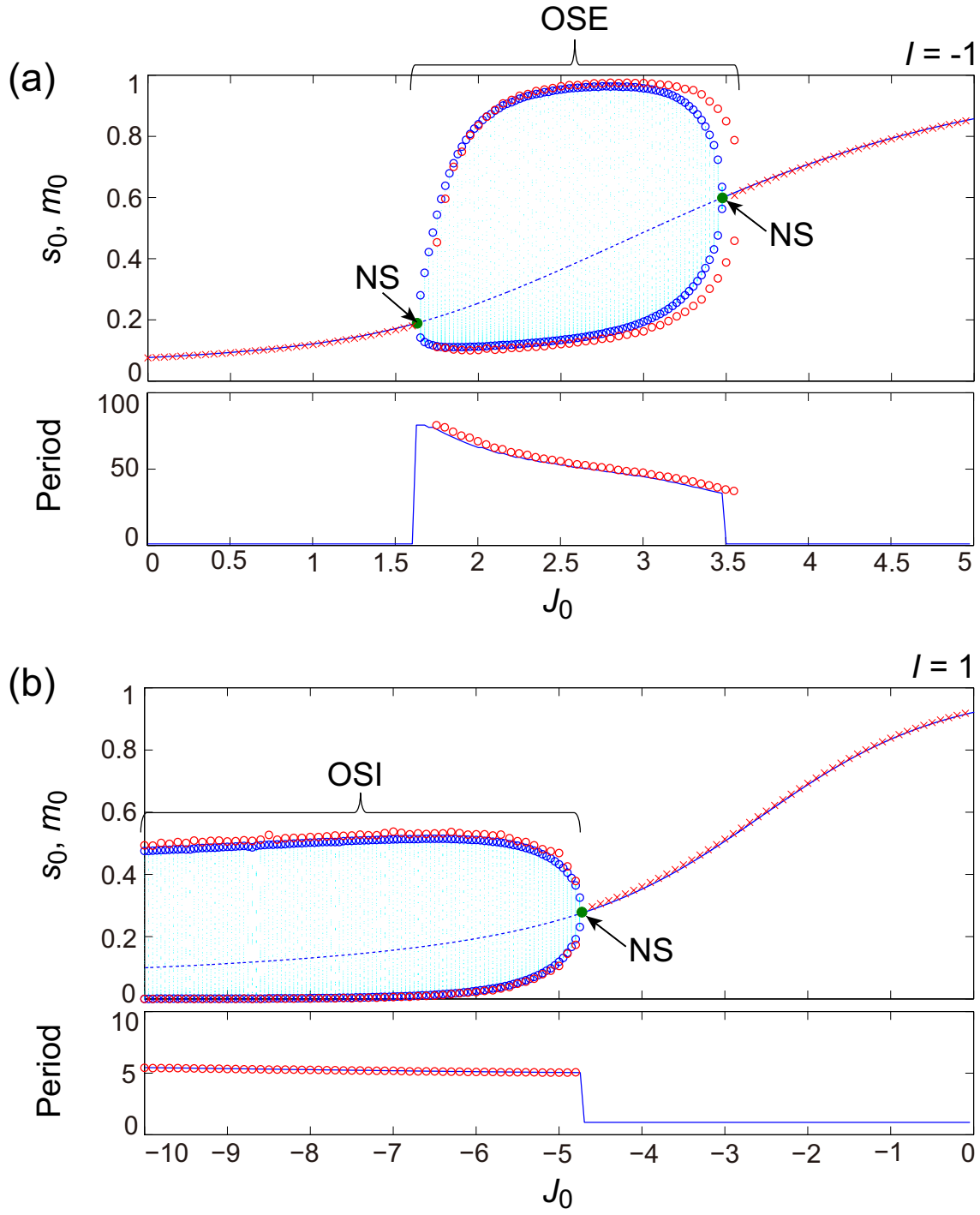

Figure 3.3. A comparison between typical bifurcation diagrams of the stochastic (red) and the macroscopic mean field (blue) models. The models show good agreement in the distribution of orbits and in the oscillatory period. In both panels (a) and (b) for the macroscopic mean field model, the notation is the same with Fig. 3.2(b) and Fig. 3.2(c). The open blue circles indicate maximal or minimal values of the OSE state for (a) or the OSI state for (b) and indicate the corresponding oscillatory period. In each bifurcation parameter point for the stochastic model, when the absolute difference between the maximal and minimal values exceeded a certain threshold value, a pair of two red open circles was plotted; the red cross indicates the averaged value of the stochastic variable. (a) A bifurcation diagram and the corresponding oscillatory period of the excitatory network on $I = -1$. (b) A bifurcation diagram and the corresponding oscillatory period of the inhibitory network on $I = 1$.

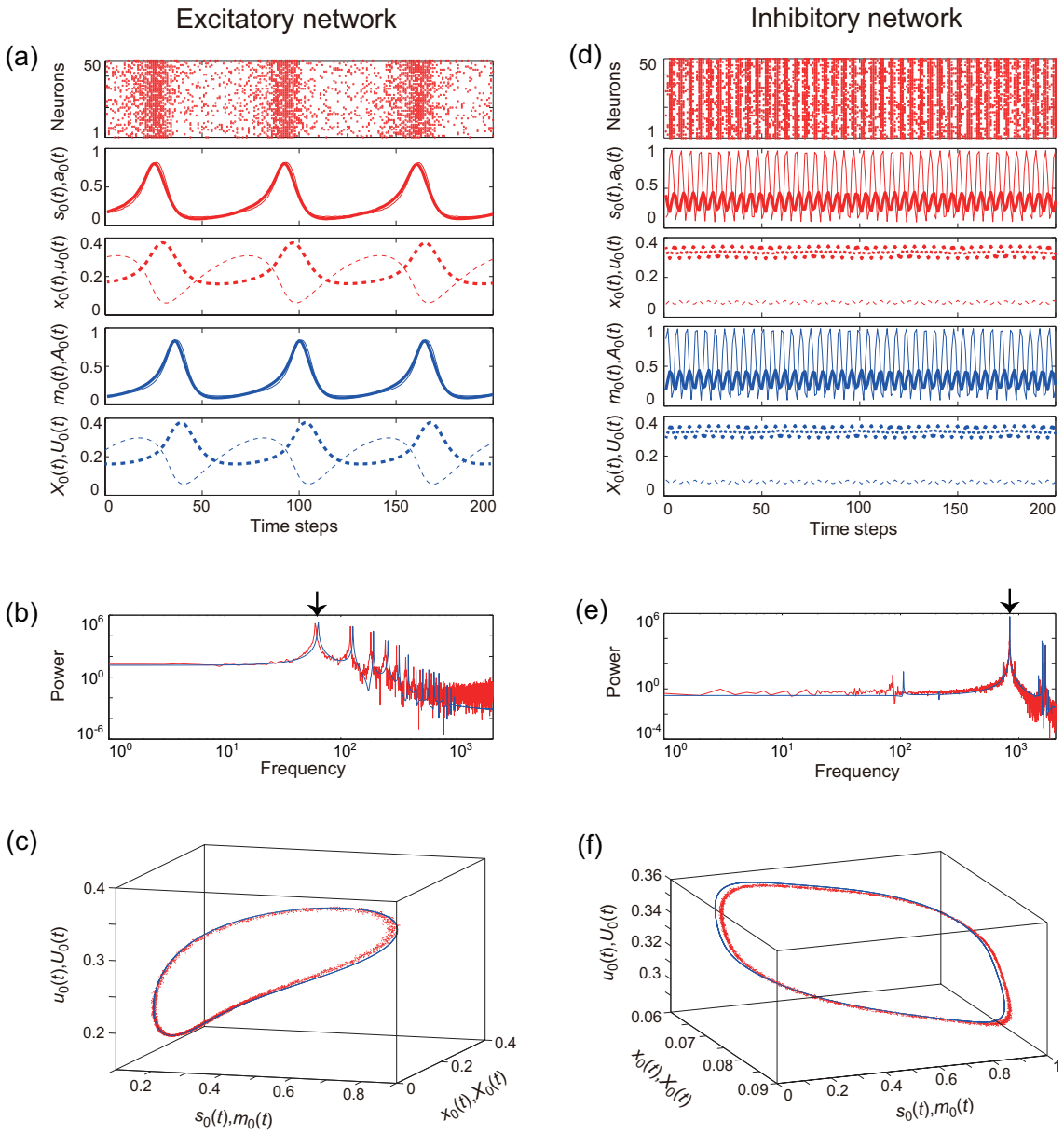

Figure 3.4. Simulation results of the excitatory and inhibitory networks with depression synapses. The dynamics on the stochastic and the macroscopic mean field models are illustrated in red and blue, respectively. The excitatory and inhibitory networks exhibit relatively slow (the left side) and fast oscillations (the right side), respectively. (a, d) Raster plots and time courses of the variables of the stochastic and macroscopic mean field models. The dots indicate 50 of 10^4 excitatory or inhibitory neurons (where $s_i(t) = 1$). Each of the stochastic variables, $s_0(t)$, $a_0(t)$, $x_0(t)$, and $u_0(t)$ and each of the macroscopic variables, $m_0(t)$, $A_0(t)$, $X_0(t)$, and $U_0(t)$ are indicated as time courses by the thin and thick solid lines and the thin and thick dashed lines, respectively. Note that the time courses of $s_0(t)$ and $a_0(t)$ and those of $m_0(t)$ and $A_0(t)$ for (a) are almost overlapping, respectively. (b, e) Power spectra of the variables $s_0(t)$ and $m_0(t)$. The two arrows indicate the fundamental low and high frequency components. (c, f) Closed curves in the state space.

exponents determines whether the attractor is the closed curve or the 2-dimensional torus. If the dynamics shows the OS2T state, two zero-exponents appear, whereas if the OS1C or OS2C state emerges in the system, only one zero-exponent appears.

Both the OS1C and OS2C states exhibit quasi-periodic oscillations on a one-dimensional torus in a map (MT1), and they are generated from the SS state via the NS bifurcation set; note that the MT1 is equivalent to the closed curve described above. On the other hand, the OS2T state shows quasi-periodic oscillations on a 2-dimensional torus in a map (MT2). These three oscillatory states, namely OS1C, OS2C, and OS2T states, can be separated by the following three sets of bifurcations: the NS bifurcation of MT1 (MT1NS), the saddle-node (SN) bifurcation of MT2 (MT2SN), and the cyclic SN bifurcation of MT1 (MT1SNC) [61]. Because the MT1NS bifurcation here is subcritical, there exists a specific hysteresis region between the OS1C and OS2T states.

By introducing a 'slice' into the quasi-periodic attractors, we can interpret the bifurcations of quasi-periodic oscillations, as those of the fixed point almost equivalently [Fig. 3.5(b)]; however, note that the slice has a width of radius ϵ, differently from the Poincaré section. Let us define a 'section' Σ as a codimension-one plane so that we can define the slice as follows:

$$\Sigma^{\epsilon} \quad = \quad \{\Omega \in \mathbb{R}^8 | \mathrm{dist}(\Omega, \Sigma) < \epsilon\}, \tag{3.57}$$

where $\mathrm{dist}(\cdot, \cdot)$ denotes the Euclidean distance between a point and a plane. For example, if a MT1 is applied to the slice, it will be converted to an 'isolated' point, and if a MT2 is applied to the slice, it will be converted to a 1-dimensional torus in a section (ST1), respectively. Although the isolated point and ST1 are not invariant sets, we apply the conventional bifurcation theory into them, to understand the quasi-periodic bifurcations more clearly.

Here we analyze the MT1 and MT2, by using the slice. When the MT1NS bifurcation occurs, a MT2 appears along with the destabilization of the MT1; in the corresponding slice, the isolated point loses its stability, and accordingly a ST1 emerges around it. On the other hand, when the MT2SN bifurcation occurs, a stable MT2 and a saddle one merge and disappear, and the trajectory on the stable MT2 goes onto a MT1; in the corresponding slice, a stable ST1 and a saddle one collides, and accordingly an isolated point appears. The bifurcation diagram of trajectories in the slice, with respect to J_0^{EI}, declares the qualitative difference between the OS1C and OS2T states [Fig. 3.5(c)]. The isolated point, which is one realization of the OS1C state, starts to oscillate via the MT1NS bifurcation, and changes to a ST1, which is one realization of the OS2T state. On the other hand, via the MT2SN bifurcation the ST1 suddenly changes to an isolated point; this abrupt change is due to the subcritical MT1NS bifurcation.

To understand the property of the MT1SNC bifurcation, we introduce a cyclic SN bifurcation of a zero-dimensional torus in a map (MT0SNC) [Fig. 3.6(a)]; note that the

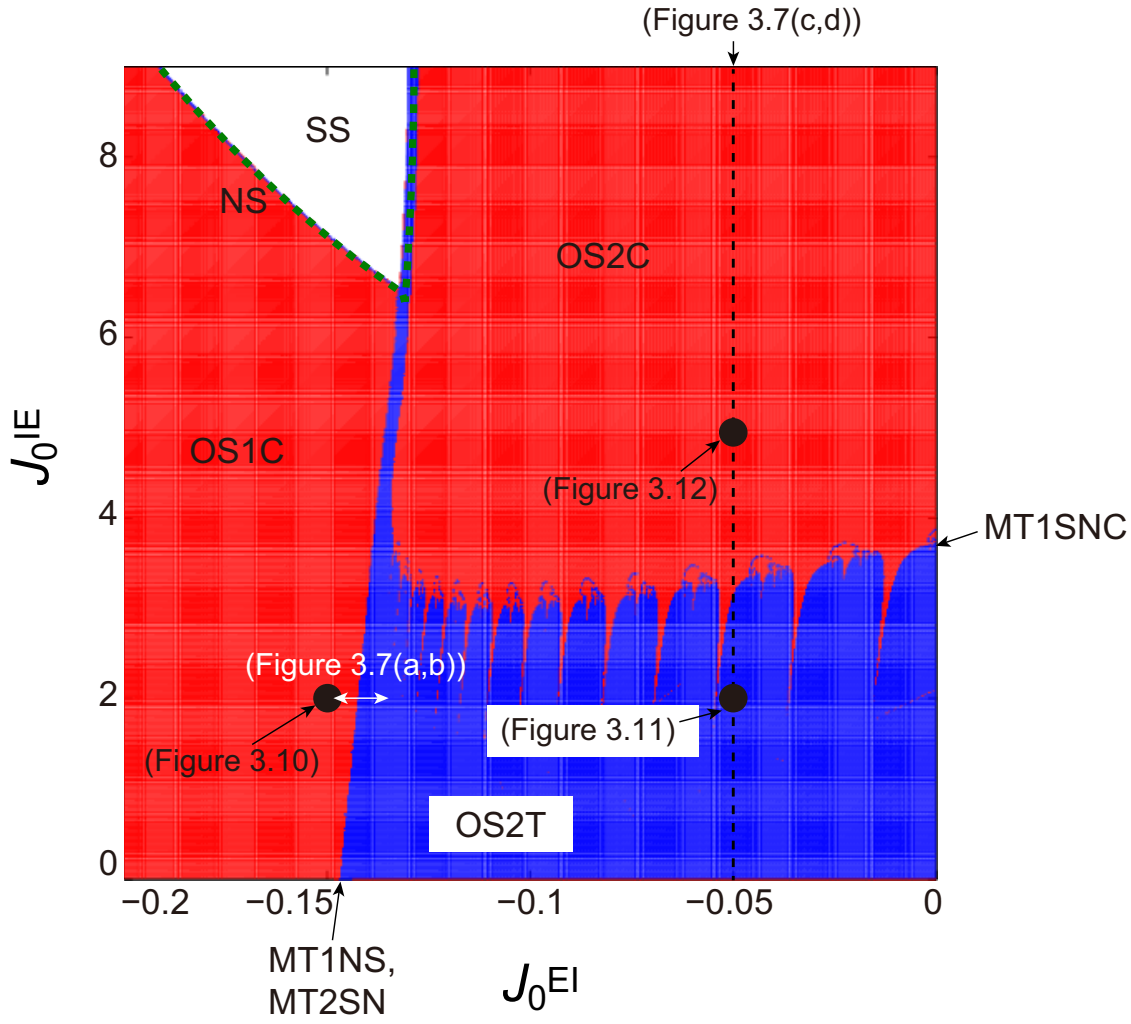

Figure 3.5. $(J_0^{\mathrm{EI}}, J_0^{\mathrm{IE}})$ phase diagram, emergent from the network composed of the excitatory and inhibitory subnetworks with depression synapses. In this network, $J_0^{\mathrm{EE}} = 2$, $I^{\mathrm{E}} = -1$, and $\tau_{\mathrm{a}}^{\mathrm{E}} = 2.5$ were set for the excitatory subnetwork, and $J_0^{\mathrm{II}} = -10$, $I^{\mathrm{I}} = 16$, and $\tau_{\mathrm{a}}^{\mathrm{I}} = 12.5$ for the inhibitory subnetwork, respectively. The Lyapunov exponents were calculated in each parameter point, where the number of zero-exponents determines the color; the parameter points with only one and two zero-exponents are denoted by red and blue colors, respectively, whereas the points with all the negative exponents are marked by the white color. The SS region bifurcates into the OS1C or OS2C region via the NS bifurcation set, indicated by the dashed curve. The OS1C and OS2T regions are separated by the MT1NS or the MT2SN bifurcation set, whereas the OS2C and OS2T regions are separated by the MT1SNC bifurcation set. Note that the MT1NS and MT2SN bifurcation sets are overlapping because the hysteresis region between them is very narrow.

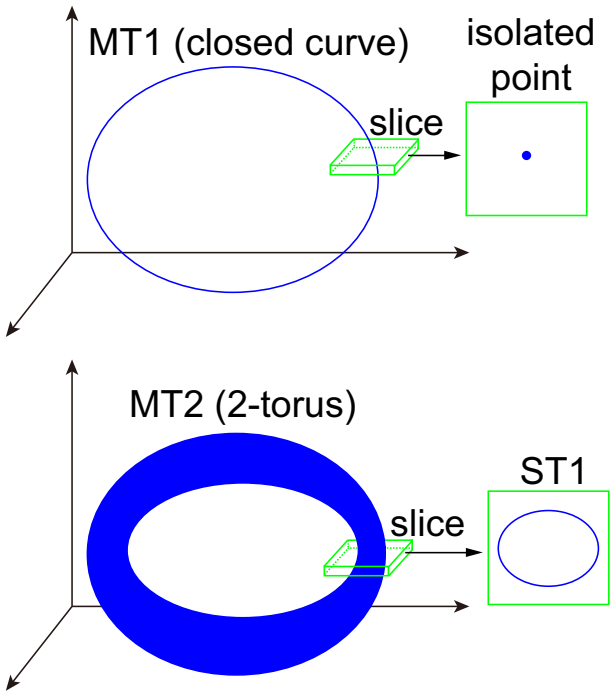

Figure 3.6. A schematic definition of the isolated point and ST1 in the slice. The slice has a width of radius ϵ. Via the slice, the MT1 and MT2 are converted to an isolated point and a ST1, respectively

zero-dimensional torus is equivalent to the fixed point. Before the MT0SNC bifurcation occurs, there exists a pair of a stable fixed point and a saddle one, and therefore the unstable set of the saddle point is generating a 1-dimensional torus. Via the MT0SNC bifurcation, in which the stable fixed point and the saddle one collide, the unstable set of the saddle point is stabilized and accordingly an MT1 appears. Next, we consider the MT1SNC bifurcation [Fig. 3.6(b)]. Before this bifurcation occurs, there exists a pair of a stable MT1 and a saddle one, and thus the unstable set of the saddle MT1 is generating a 2-dimensional torus; in the corresponding slice, there exists a pair of a stable isolated point and a saddle one so that the unstable set of the saddle isolated point can form a 1-dimensional torus. Via the MT1SNC bifurcation, the stable MT1 and the saddle one merge and disappear, and accordingly an MT2 appears with stabilization of the unstable set of the saddle MT1; in the corresponding slice, an ST1 appears similar to the MT0SNC bifurcation. The bifurcation diagram of trajectories in the slice, with respect to J_0^{IE}, declares the qualitative difference between the OS2C and OS2T [Fig. 3.5(d)]. As well as the MT1NS bifurcation, the isolated point, corresponding to the OS2C state, starts to oscillate via the MT1SNC bifurcation, and changes to the ST1, corresponding to the OS2T state.

Actually, the difference between the MT1NS and MT1SNC bifurcations becomes clear, by the consideration of both a state just before the bifurcations and a state just after

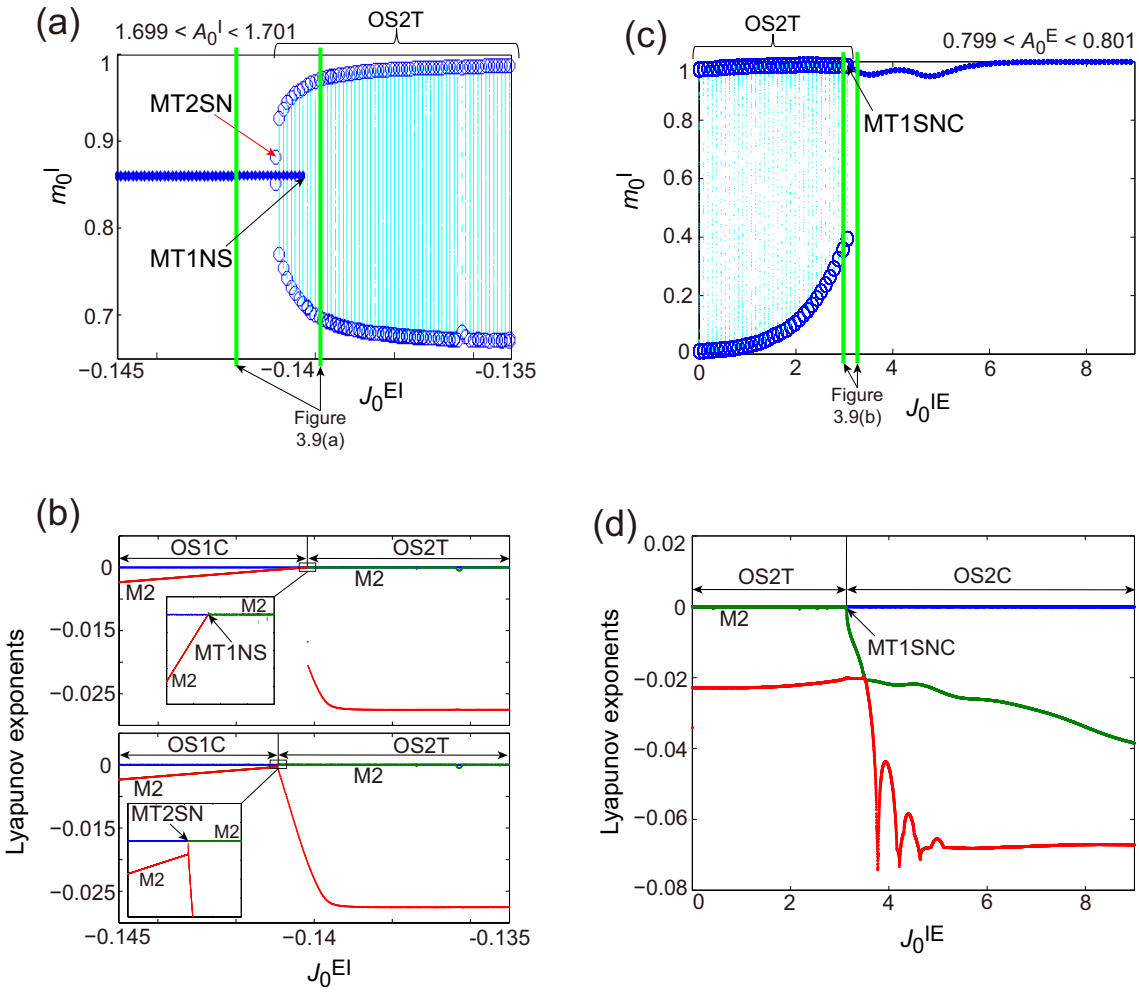

Figure 3.7. Representative bifurcation diagrams of trajectories in the section for (a) and (c) and of Lyapunov exponents for (b) and (d) with respect to J_0^{EI} or J_0^{IE}, respectively. (a, b) The OS1C and OS2T states were separated by the MT1NS and MT2SN bifurcations. (c, d) The OS2T and OS2C states were separated by the MT1SNC bifurcation. (a) A bifurcation diagram of trajectories in section $A_0^I = 1.7$ whose slice has $\epsilon = 0.001$, with respect to J_0^{EI}. The OS1C state is indicated by the solid line, while the OS2T state is indicated by dotted lines; maximal and minimal values of the orbits are indicated by the open circles. (b) A bifurcation diagram of the Lyapunov exponents with respect to J_0^{EI}. The first, second, and third Lyapunov exponents are plotted by the blue, green, and red colors, respectively. The multiplicity 2 of the exponents is indicated by notation "M2". For the upper diagram, the calculation of the Lyapunov exponents was conducted with the increase of J_0^{EI}, whereas for the lower diagram, it was conducted with the decrease of J_0^{EI}. (c) A bifurcation diagram of trajectories in section $A_0^E = 0.8$ whose slice has $\epsilon = 0.001$, with respect to J_0^{IE}. The OS2C state is indicated by the solid curve. (d) A bifurcation diagram of the Lyapunov exponents with respect to J_0^{IE}.

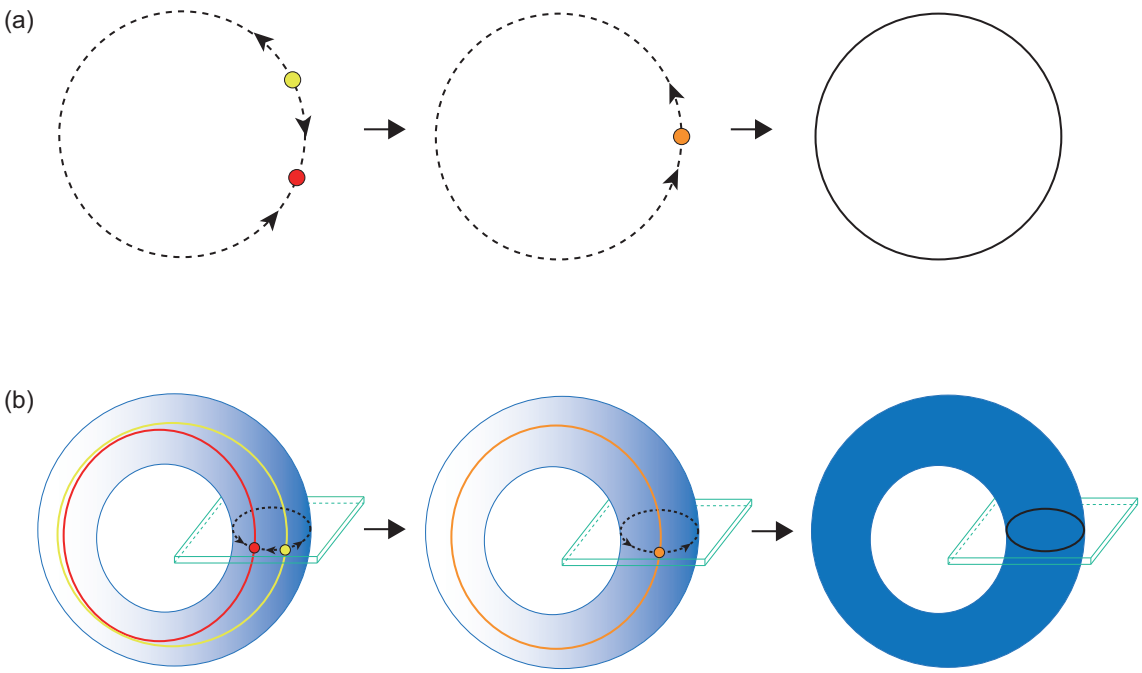

Figure 3.8. Illustrations of (A) the MT0SNC and (B) MT1SNC bifurcations. Each of the stable fixed point, saddle point, and MT0SNC bifurcation point for (A), and each of the stable MT1, saddle MT1, and MT1SNC bifurcation point for (B), are indicated by the red, yellow, and orange colors, respectively. In the slice, indicated by the green box, the MT1 is referred to as the isolated point. Before the bifurcation occurs, the unstable set of the saddle point (or the saddle MT1) is generating a 1-dimensional torus (or a 2-dimensional torus), indicated by the dotted curve for (A) (or the gradation area for (B)). Via the MT0SNC (MT1SNC) bifurcation, the unstable set is stabilized, and accordingly an MT1 (or an MT2) appears, indicated by the solid curve for (A) (or the uniformly filled area for (B)); in the slice, the unstable set of the isolated point, indicated by the dotted curve for (B), is stabilized and changes to a stable ST1, indicated by the solid curve for (B).

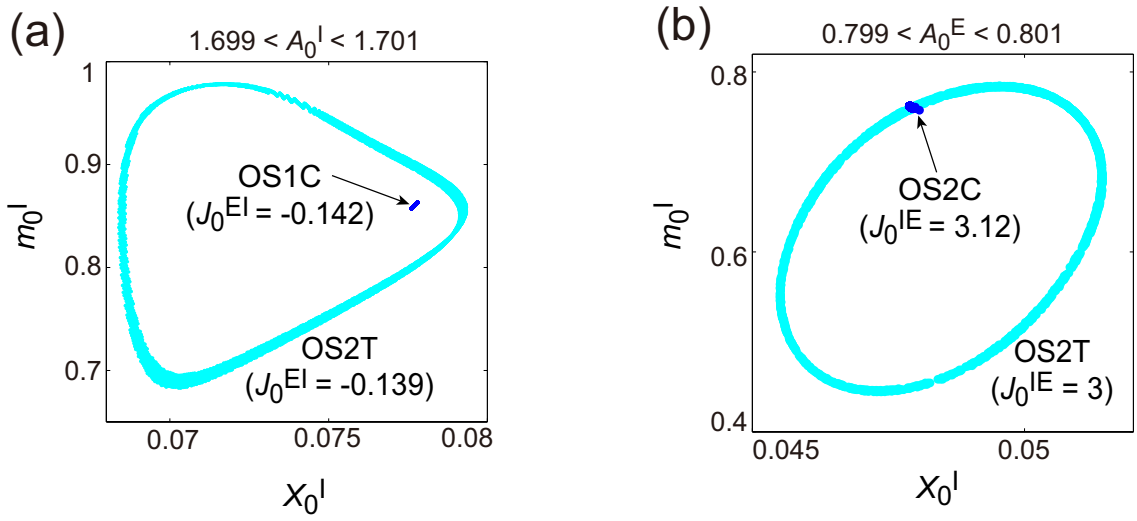

Figure 3.9. Qualitative difference between (a) the MT1NS and (b) MT1SNC bifurcations. (a) A section $A_0^{\mathrm{I}} = 1.7$ whose slice has $\epsilon = 0.001$; trajectories on the OS2T and OS1C states are plotted by the cyan and blue colors, respectively. Each parameter of these states was set to be near the MT1NS bifurcation points: $J_0^{\mathrm{EI}} = -0.139$ and $J_0^{\mathrm{EI}} = -0.142$. (b) A section $A_0^{\mathrm{E}} = 0.8$ whose slice has $\epsilon = 0.001$; trajectories on the OS2T and OS2C states are plotted by the cyan and blue colors, respectively. Each parameter of these states was set near the MT1SNC bifurcation points: $J_0^{\mathrm{IE}} = 3$ and $J_0^{\mathrm{IE}} = 3.12$.

the bifurcations, together with the slice. As mentioned above, in the MT1NS bifurcation, an ST1 appears around the isolated point within the slice [Fig. 3.5(g)]; however, in the MT1SNC bifurcation, an ST1 also appears, but it is formed on the isolated point [Fig. 3.5(h)]. Therefore, we can distinguish these bifurcations, by investigating whether the ST1 involves the isolated point within the slice.

The qualitative difference between the MT1NS bifurcation and the MT2SN or MT1SNC bifurcation is also evident with the consideration of the property of the Lyapunov exponents near the bifurcation points [Fig. 3.5(e) and Fig. 3.5(f)]. Indeed, when the OS1C state bifurcates into the OS2T state, the two negative exponents approach zero simultaneously, which is a property of the MT1NS bifurcation. However, when the OS2T bifurcates into the OS1C or the OS2C state, only one negative exponent starts to decrease; this is a property of the MT2SN or MT1SNC bifurcation.

Figures 3.10, 3.11, and 3.12 show the typical oscillatory states in the model composed of excitatory and inhibitory neurons. For each typical oscillatory state in the stochastic model, the average values of the variables $s_0^\xi(t)[= (1/N_\xi)\sum_i^{N_\xi} s_i^\xi(t)]$, $a_0^\xi(t)[= (1/N_\xi)\sum_i^{N_\xi} a_i^\xi(t)]$, $x_0^\xi(t)[= (1/N_\xi)\sum_i^{N_\xi} x_i^\xi(t)]$, and $u_0^\xi(t)[= (1/N_\xi)\sum_i^{N_\xi} u_i^\xi(t)]$ are indicated by red curves. The corresponding values in the macroscopic mean field model are indicated by blue curves. The power spectra of the oscillatory time courses were obtained using the variables $s_0^{\mathrm{I}}(t)$ and $m_0^{\mathrm{I}}(t)$. The macroscopic mean field model is similar to the stochastic model in the

time courses [Figs. 3.10(a), 3.10(b), 3.11(a), 3.11(b), 3.12(a), and 3.12(b)], in the power spectra [Figs. 3.10(c), 3.11(c), and 3.12(c)], in the orbits in the state space [Figs. 3.10(d), 3.11(d), and 3.12(d)] , and in the orbits in the slice [Figs. 3.10(e), 3.11(e), and 3.12(e)].

Figure 3.10 shows the appearance of the OS1C state in the network dynamics. The typical OS1C state [Fig. 3.10(a) and Fig. 3.10(b)] exhibits only fast oscillations both in the stochastic model and in the macroscopic mean field model. The excitatory subnetwork shows a low active state with fast oscillations. On the other hand, the inhibitory subnetwork indicates a highly active state with fast oscillations. The power spectra [Fig. 3.10(c)] of the oscillatory time courses exhibit a single large peak that indicates fast oscillations.

Figure 3.11 shows the appearance of the OS2T in the network dynamics. The typical OS2T state [Fig. 3.11(a) and Fig. 3.11(b)] shows the slow and fast oscillations both in the stochastic model and in the macroscopic mean field model. The excitatory subnetwork displays only the slow oscillations. On the other hand, the inhibitory subnetwork exhibits both the slow and fast oscillations. The power spectra [Fig. 3.11(c)] of the oscillatory time courses display two large peaks that indicate the slow and fast oscillations, respectively. The slice [Fig. 3.11(e)) in the state space describes the dynamical structure of the OS2T state, where a closed curve appears in the slice.

Figure 3.12 shows the appearance of the OS2C state in the network dynamics. The typical OS2C state [Fig. 3.12(a) and Fig. 3.12(b)] also exhibits the slow and fast oscillations both in the stochastic model and in the macroscopic mean field model. The excitatory subnetwork shows only the slow oscillation. On the other hand, the inhibitory subnetwork exhibits both the slow and fast oscillations as well as the OS2T state. The modulation of the amplitude is clearer than that in the OS2T state. The power spectra [Fig. 3.12(c)] of the oscillatory time courses exhibit two large peaks that indicate the slow and fast oscillations, respectively.

3.4 Discussion

We analyzed a stochastic model composed of excitatory and inhibitory neural networks and dynamic synapses and derived the mean field model. The analysis of the mean field model revealed overall dynamical properties of the network. The excitatory and inhibitory subnetworks represent the slow and fast oscillations, respectively. As a result of the interaction between the excitatory and inhibitory subnetworks, diverse oscillatory states with two major frequency components appear; this oscillatory state corresponds to cross-frequency coupling. The bifurcation analysis has clarified the dependency of oscillatory states on the weights J_0^{EI} and J_0^{IE} of the connection between the excitatory and inhibitory networks. Furthermore, we have found that the states of the cross-frequency coupling can be classified into two subtypes, namely, OS2T and OS2C states.

The present model is an extension of an excitatory neural network model with dynamic synapses [22]. The previous model, which corresponds to the excitatory network in this

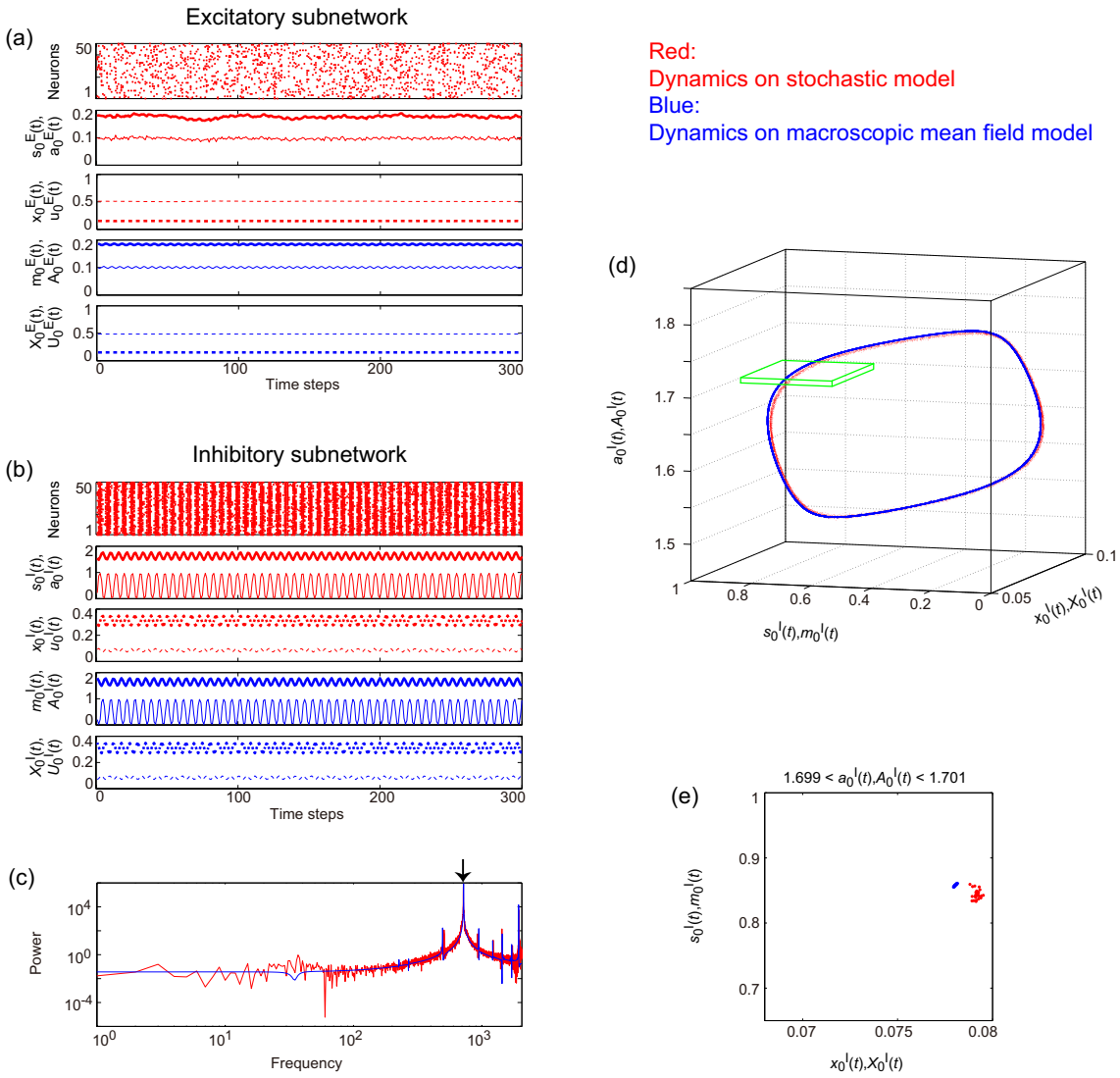

Figure 3.10. A typical oscillatory state with a single frequency component on a closed curve (OS1C) in the network with depression synapses. Both the excitatory and inhibitory subnetworks exhibit the fast oscillations on the closed curve, whereas the amplitude of excitatory oscillations is miniature. (a, b) Raster plots and time courses of the variables of the stochastic and macroscopic mean field models. The dots indicate 50 of 10^4 excitatory or inhibitory neurons (where $s_i^{\mathrm{E}}(t) = 1$ and $s_i^{\mathrm{I}}(t) = 1$). Each of the stochastic variables $s_0^{\mathrm{E}}(t)$, $a_0^{\mathrm{E}}(t)$, $x_0^{\mathrm{E}}(t)$, and $u_0^{\mathrm{E}}(t)$ for the excitatory subnetwork and $s_0^{\mathrm{I}}(t)$, $a_0^{\mathrm{I}}(t)$, $x_0^{\mathrm{I}}(t)$, and $u_0^{\mathrm{I}}(t)$ for the inhibitory subnetwork, and each of macroscopic variables, $m_0^{\mathrm{E}}(t)$, $A_0^{\mathrm{E}}(t)$, $X_0^{\mathrm{E}}(t)$, and $U_0^{\mathrm{E}}(t)$ for the excitatory subnetwork and $m_0^{\mathrm{I}}(t)$, $A_0^{\mathrm{I}}(t)$, $X_0^{\mathrm{I}}(t)$, and $U_0^{\mathrm{I}}(t)$ for the inhibitory subnetwork are indicated as time courses by the thin and thick solid lines and the thin and thick dashed lines, respectively. (c) Power spectra of the variables $s_0^{\mathrm{I}}(t)$ and $m_0^{\mathrm{I}}(t)$. The arrow indicates the representative frequency component, which exhibits a high frequency. (d) A closed curve in the state space, in which the slice is indicated by the green box. (e) A section with $a_0^{\mathrm{I}} = 1.7$ and $A_0^{\mathrm{I}} = 1.7$ whose slice has $\epsilon = 0.001$. The isolated point appears in the slice because the emergent attractor was the closed curve.

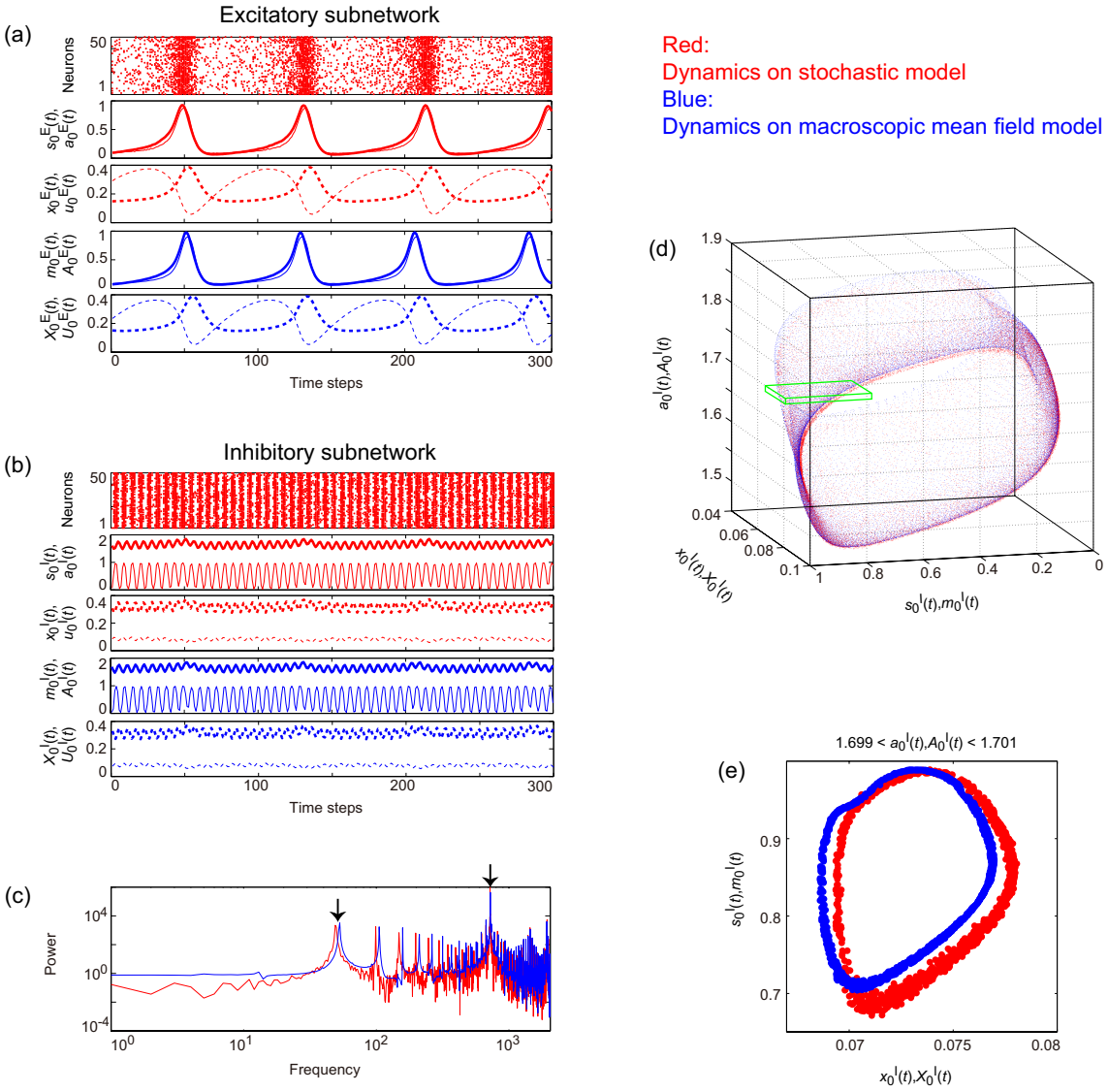

Figure 3.11. A typical oscillatory state with the two major frequency components on a 2-dimensional torus (OS2T) in the network with depression synapses. The excitatory and inhibitory subnetworks exhibit the slow and fast oscillations on the torus, respectively, whereas the amplitude of the inhibitory oscillations $s_0^{\mathrm{I}}(t)$ and $m_0^{\mathrm{I}}(t)$ is less modulated by the phase of excitatory slow oscillations. In panels (a) and (b), the notation is similar to that of Fig. 3.10. (c) Power spectra of the variables $s_0^{\mathrm{I}}(t)$ and $m_0^{\mathrm{I}}(t)$. The two arrows indicate the representative low and high frequency components. (d) A torus in the state space, in which the slice is indicated by the green box. (e) A section with $a_0^{\mathrm{I}} = 1.7$ and $A_0^{\mathrm{I}} = 1.7$ whose slice has $\epsilon = 0.001$. The closed curve appears in the slice because the emergent attractor was the 2-dimensional torus.

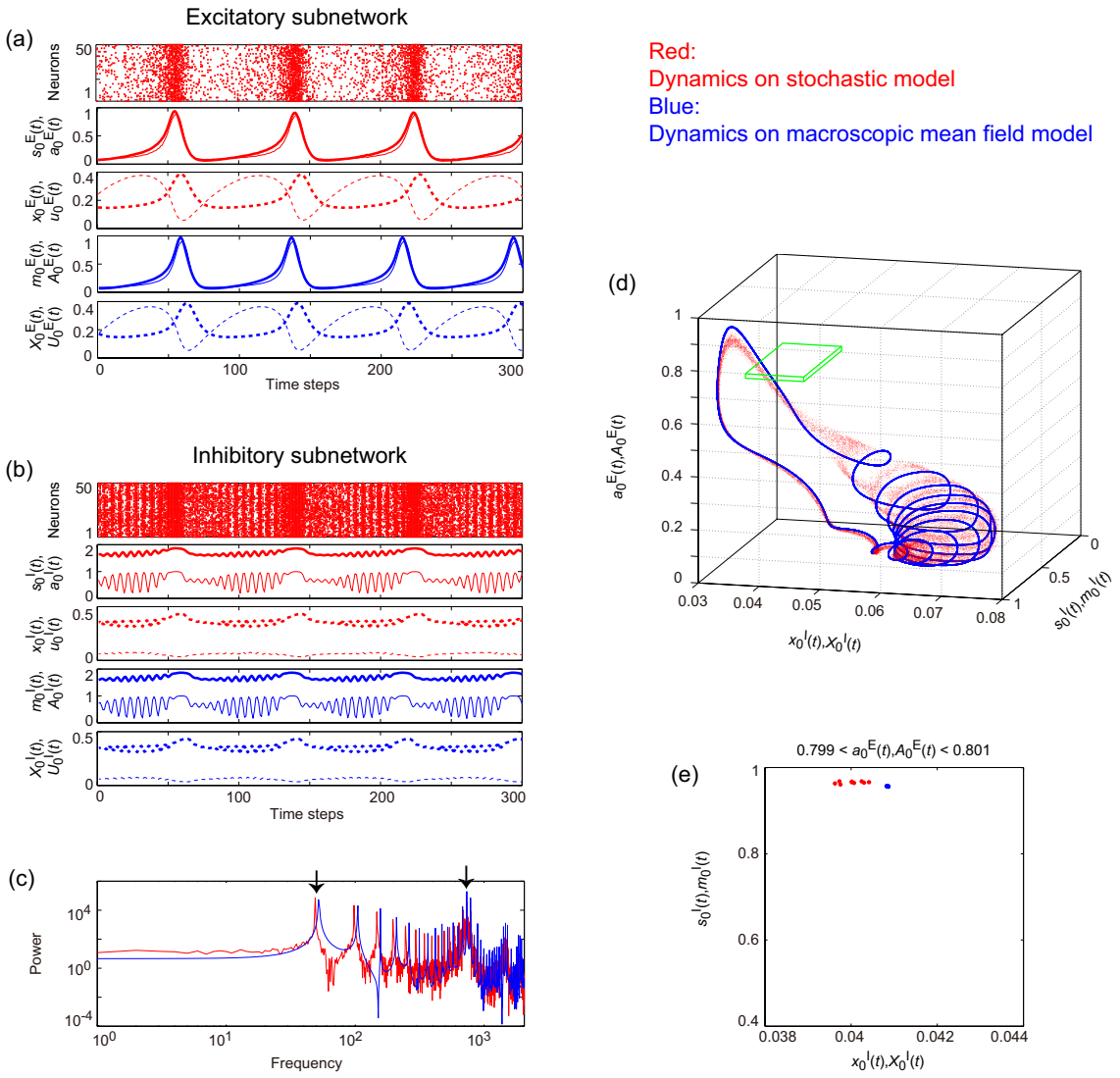

Figure 3.12. A typical oscillatory state with the two major frequency components on a closed curve (OS2C) in the network with depression synapses. The excitatory and inhibitory subnetworks exhibit the slow and fast oscillations on the closed curve, respectively, whereas the amplitude of inhibitory oscillations $s_0^{\mathrm{I}}(t)$ and $m_0^{\mathrm{I}}(t)$ is evidently modulated by the phase of excitatory slow oscillations. In panels (a) and (b), the notation is similar to that of Fig. 3.10. (c) Power spectra of the variables $s_0^{\mathrm{I}}(t)$ and $m_0^{\mathrm{I}}(t)$. The two arrows indicate the representative low and high frequency components. (d) A closed curve in the state space, in which the slice is indicated by the green box. (e) A section with $a_0^{\mathrm{E}} = 0.8$ and $A_0^{\mathrm{E}} = 0.8$ whose slice has $\epsilon = 0.001$. The isolated point appears in the slice because the emergent attractor was the closed curve.

study, was modified in terms of the following three aspects. First, we analyzed the dependency of the network dynamics on the coupling strength $J_0^{\xi\xi}$ of the network and on the external input I^{ξ}; these parameters were fixed in the previous study [22]. The analysis revealed that these parameters can be crucial for the generation of a variety of oscillatory states. The second point concerned the introduction of an additional variable $a_i^{\xi}(t)$ corresponding to the synaptic activity, with the parameter $\tau_{\rm a}^{\xi}$ representing the time constant for the decay process. The third point was the combination of the excitatory network with the inhibitory one, where the parameters $J_0^{\rm EI}$ and $J_0^{\rm IE}$ were introduced to indicate the coupling weights between these networks.

Depending on the synaptic properties, the network dynamics changes; the decay time constants $\tau_{\rm a}^{\rm E}$ and $\tau_{\rm a}^{\rm I}$ of the synaptic activity determine, respectively, the frequency of the slow oscillation in the excitatory network [Fig. 3.2(d)] and that of the fast oscillation in the inhibitory network [Fig. 3.2(e)]. A variation of the frequency band of neural activity, such as delta, theta, alpha, beta, and gamma waves, can be observed in the brain and has been suggested to be correlated with brain functions [3]. The synaptic parameters may contribute to modulate the oscillatory properties and brain functions. Indeed, aminomethylphosphonic acid (AMPA) synapses have a relatively short time constant, whereas N-methyl-D-aspartate (NMDA) synapses have a longer time constant; this difference between these synaptic properties should affect the generation of neural oscillations and functions.

We have found that the generation mechanism of the OSI state, as shown in the phase diagram [Fig. 3.2(a)], is qualitatively consistent with physiological experiments [62, 63]. Inhibitory interneurons in the rat hippocampal CA3 region show a relatively fast oscillation, which is referred to as the gamma oscillation. This gamma oscillation is blocked by the AMPA or gamma-aminobutyric acid (GABA) type-A receptor antagonist. The AMPA-type synapses send the excitatory input to the interneurons, while the GABA type-A synapses send recurrent inhibitory connections among the interneurons. On the phase diagram [Fig. 3.2(a)], we can consider these antagonists as the realizations of the external input $I^{\rm I}$ and the absolute value of the coupling strength $J_0^{\rm II}$, respectively. Thus, the OSI state observed in the present model can be interpreted as the gamma oscillations in inhibitory interneuron networks.

In the network composed of both excitatory and inhibitory subneurons, network dynamics shows phase-amplitude cross-frequency coupling as shown in Figs. 3.11 and 3.12. The properties of this oscillatory phenomenon are similar to those of the cross-frequency coupling between the theta (relatively slow) and gamma oscillations observed in the hippocampus [64].

Various oscillatory phenomena, including the cross-frequency coupling, may contribute to information coding in the brain. The presence of distinctive oscillatory states in our model implies that a variety of information coding schemes can exist in the neural network. We showed that the oscillatory state with the two major frequency components can be

classified into the OS2T and OS2C states [Fig. 3.11 and Fig. 3.12], respectively [see the detailed structures of the OS2T and OS2C states in Appendix E]. In the OS2T state, the peaks of the fast oscillation are broadly distributed on the phase of the slow oscillation. On the other hand, in the OS2C state, the phase of the fast oscillation is locked by the slow oscillation; thus, the peaks of the fast oscillation appear in specific phases of the slow oscillation. The phase of the neural activity can be utilized to encode certain information. Indeed, the physiologically observed cross-frequency coupling has been suggested to provide a basis for the effective communications among neurons [64].

The mechanisms and functions of the oscillatory phenomena must be further explored in the future. In the present model, we used the binary-state and discrete-time neuron model; in the future, the oscillatory phenomena observed in the present model should be evaluated with a more realistic network model that reflects detailed properties of the cerebral cortex.

Chapter 4

Conclusions

In this study, a variety of nonlinear dynamics have been analyzed in terms of multiple time-scales the brain involves to form macroscopic oscillations shown in e.g. EEG signals, where it has been believed that the oscillations are associated with the facilitation of information processing by adaptively changing the properties of themselves. Thus, this study has been performed with both aspects of nonlinearity and linearity, i.e., nonlinear dynamics emergent from the brain has been analyzed from the viewpoint of frequencies—which are separated linearly—forming oscillations. Towards analyses of brain dynamics, actually a set of oscillations has been divided into the following two subsets: (I) deterministic oscillations and (II) stochastic fast oscillations, and furthermore subset (I) has been divided into the following two sub-subsets (Ia) deterministic slow oscillations and (Ib) deterministic fast oscillations, in terms of stochastic dynamical systems so that the dynamical noise has been defined in the sense of the Gaussian white noise.

In Chapter 2, signals composed of deterministic oscillations (subset (I)) and stochastic fast oscillations (subset (II)) have been analyzed, where a novel nonlinear time series analysis method had been strongly required because the conventional nonlinear time series analysis methods based on Takens' embedding theorem, in general, have been suitable only for deterministic dynamical systems, not for stochastic dynamical systems. Typically, it has been considered that the essential difference between the deterministic and stochastic dynamical systems is whether the dynamical noise drives variables in the state space so that the trajectory temporally evolves stochastically, although many conventional nonlinear time series analysis methods mainly have aimed at characterizing deterministic trajectories. Accordingly, a novel nonlinear time series analysis method, called time series dimension (TSD), has been developed to overcome the aforementioned drawback, where the novel dimension, TSD, enabled to detect the level of underlying dynamical noise only from time series data and furthermore, the TSD does not require any information associated with the dynamics generating time series and works even if the length of time series is very short so that there exist a possibility that the TSD can open the door where nonlinear time series analysis methods including the TSD have been broadly used in the neuroscience field.

In Chapter 3, signals composed of deterministic slow oscillations (sub-subset (Ia)) and deterministic fast oscillations (sub-subset (Ib)) have been analyzed, where an extended discrete-time neural network model, comprising excitatory and inhibitory stochastic neurons, has been introduced so that the corresponding macroscopic model can be derived through the mean field approximation. Now it has been considered that this mean field approximation is a key technology to approach the elucidation of the process of consciousness generation because it has been hypothesized that the interactions between microscopic elements (herein the stochastic model) and macroscopic ones (herein the macroscopic model via the mean field approximation) originate from consciousness. Note, however, that it has been investigated only in the case of the feedforward interaction from the microscopic to macroscopic elements, because to study the feedback interaction between them, prior knowledge resulting from experiments using an integration between EEG recordings and external stimulation inputs to brain dynamics—for example, the transcranial magnetic stimulation (TMS) or the transcranial alternating current stimulation (tACS)—should be needed to model, where the external stimulation (pseudo macroscopic element) plays a role of EEG dynamics and affects synaptic plasticity to get some evidences that the feedback interaction concerns consciousness. To return, through the mean field approximation, the original stochastic model has been converted to the corresponding macroscopic model, namely eight-dimensional discrete-time dynamical system so that this system can generate the deterministic slow and fast oscillations, each of which originates from the excitatory subnetwork and from the inhibitory subnetwork, respectively. It has been revealed that the system involves the following two kinds of phase-amplitude frequency-coupling phenomena: oscillatory state with two frequency components on two-dimensional torus (OS2T) and that with two frequency component on closed curve (OS2C) by use of the bifurcation analysis. Furthermore, it has been identified that these states can be separated by the cyclic bifurcation of a one-dimensional torus in a map (MT1SNC).

It has been believed that the aforementioned two kinds of analyses, namely (1) nonlinear time series analysis and (2) bifurcation analysis, make us approach the elucidation of brain oscillatory dynamics with multiple time-scales. In particular, analysis (1) will lead many neuroscientists to the world filled with nonlinear dynamics, while analysis (2) will be helpful to clarify functional roles of phase-amplitude cross-coupling phenomena, connecting between macroscopic and microscopic dynamics.

Acknowledgments

First of all, I would like to express my sincere gratitude to the journal of Physics Letters A, because the publisher Elsevier has permitted Chapter 2 to include major parts of the contents in Ref. [1]. In addition, the contents of Chapter 3 was submitted to the journal of Frontiers in Computational Neuroscience.

I would like to express my deepest gratitude to Professor Kazuyuki Aihara, who gave me very suitable environmental spaces to study with his laboratory members, including many postdoctoral researchers, especially belonging to the Aihara innovative mathematical modelling project through the FIRST program. All the discussions with them inspired my inquiring mind. In particular, I have remembered that Prof. Aihara gave me very critical some comments related to the relationship between the continuous-time and discrete-time dynamical systems. A simple example consisting of the logistic equation and the logistic map was very beneficial to model brain dynamics as a form of the discrete-time dynamical system. Furthermore, I have realized values of the torus attractors emergent from the discrete-time dynamical system.

In addition, I would like to thank Professor. Fumiyasu Komaki, Professor. Takayasu Matsuo, Professor. Yoko Yamaguchi, Professor. Hideyuki Suzuki, and Professor. Yoshito Hirata, each professor of who kindly received a role of the referee for my Ph. D program. Especially, the comments arising from Prof. Komaki were very kind to facilitate my understanding of the theory for the time series dimension (TSD).

In considering the creation of Chapter 2, I would like to express my sincere gratitude to Prof. Hirata, who gently accepted to work as a coauthor of my Ph. D study. All the discussions with him were very helpful to progress my mathematical thinking and English writing skills, needed for Ph. D graduation. I would also like to thank Dr. Keiichi Kitajo, who gave me some crucial suggestions concerned with neural oscillations in the brain. Discussions with him were so exciting for me.

In considering the creation of Chapter 3, I would like to express my sincere gratitude to Professor. Motomasa Komuro, who kindly taught me how to analyze bifurcations in discrete-time dynamical systems. Thanks to him, I could stand at the starting point of the bifurcation research. I would also like to thank Dr. Yuichi Katori, who motivated me to study the bifurcation analysis via mathematical modeling.

Further, I would like to thank Dr. Makito Oku, who was always supporting me, even if he was so busy.

Finally, I would like to thank all of the laboratory members, my friends, and my families both in Japan and in Malaysia. They warmly watched over the growth of me. In particular, I would like to express my deep gratitude to my mother and farther, who greatly supported me. Of course, I would like to express my deep gratitude to my wife, Nurul Liyana Binti Mohamad Zulkufli, who was always beside me, even if she was in Malaysia.

Bibliography

[1] T. Sase, J. Pena Ramirez, K. Kitajo, K. Aihara, and Y. Hirata (2016), Estimating the level of dynamical noise in time series by using fractal dimensions, Phys. Lett. A **380**, pp. 1151–1163.

[2] G. Edelman and G. Tononi, *A universe of consciousness: How matter becomes imagination* (Basic Books, New York, 2000).

[3] G. Buzsáki and A. Draguhn (2004), Neuronal oscillations in cortical networks, Science **304**, 1926.

[4] M. Kawasaki, K. Kitajo, and Y. Yamaguchi (2010), Dynamic links between theta executive functions and alpha storage buffers in auditory and visual working memory, Eur. J. Neurosci. **31**, 1683.

[5] B. C. Armstrong, M. V. Ruiz-Blondet, N. Khalifian, K. J. Kurtz, , Zhanpeng Jin, and S. Laszlo (2015), Brainprint: Assessing the uniqueness, collectability, and permanence of a novel method for ERP biometrics, Neurocomputing, **166**, 59.

[6] F. Takens, *in Dynamical Systems and Turbulence*, Lecture Notes in Mathematics Vol. 898, edited by D. A. Rand and L. S. Young (Springer, Berlin, 1981), p. 366.

[7] A. Wolf, J. B. Swift, H. L. Swinney, and J. A. Vastano (1985), Determining Lyapunov exponents from a time series, Physica D, **16**, 285.

[8] M. Thiel, M. C. Romano, P. L. Read, and J. Kurths (2004), Estimation of dynamical invariants without embedding by recurrence plots, Chaos, **14**, 234.

[9] Y. Hirata and K. Aihara (2010), Identifying hidden common causes from bivariate time series: A method using recurrence plots, Phys. Rev. E **81**, 016203.

[10] N. Marwan, M. C. Romano, M. Thiel, and J. Kurths (2007), Recurrence plots for the analysis of complex systems, Phys. Rep. **438**, 237.

[11] Y. Hirata , S. Horai, and K. Aihara, (2008), Reproduction of distance matrices and original time series from recurrence plots and their applications, Eur. Phys. J. Spec. Top. **164**, 13.

[12] T. Schreiber (2000), Measuring Information Transfer, Phys. Rev. Lett. **85**, 461.

[13] M. Kawasaki, Y. Uno, J. Mori, K. Kobata, and K. Kitajo (2014), Transcranial magnetic stimulation-induced global propagation of transient phase resetting associated with directional information flow, Front. Hum. Neurosci. **8**, doi: 10.3389/fnhum.2014.00173.

[14] O. Jensen and L. L. Colgin (2007), Cross-frequency coupling between neuronal oscillations, Trends Cogn. Sci. **11**, 267.

[15] J. A. Acebron, L. L. Bonilla, C. J. Perez Vicente, F. Ritort, and R. Spigler (2005), The Kuramoto model: A simple paradigm for synchronization phenomena, Rev. Mod. Phys. **77**, 137.

[16] M. K. Stephen Yeung and S. H. Strogatz (1999), Time Delay in the Kuramoto Model of Coupled Oscillators, Phys. Rev. Lett. **82**, 648.

[17] Y. L. Maistrenko, B. Lysyansky, C. Hauptmann, O. Burylko, and P. A. Tass (2007), Multistability in the Kuramoto model with synaptic plasticity, Phys. Rev. E **75**, 066207.

[18] O. Davida and K. J. Fristona (2003), A neural mass model for MEG/EEG:: coupling and neuronal dynamics, Neuroimage **20**, 1743.

[19] R. C. Sotero, N. J. Trujillo-Barreto, Y. Iturria-Medina, F. Carbonell, and J. C. Jimenez (2007), Realistically Coupled Neural Mass Models Can Generate EEG Rhythms, Neural Comput. **19**, 478.

[20] O. David, L. Harrison, and K. J. Friston (2005), Modelling event-related responses in the brain, Neural Comput. **25**, 756.

[21] E. P. Hoel, L. Albantakis, and G. Tononi (2013), Quantifying causal emergence shows that macro can beat micro, PNAS **110**, 19790.

[22] Y. Katori, Y. Igarashi, M. Okada, and K. Aihara (2012), Stability analysis of stochastic neural network with depression and facilitation synapses, J. Phys. Soc. Jpn. **81**, 114007.

[23] H. Kantz and T. Schreiber, *Nonlinear Time Series Analysis* (Cambridge University Press, Cambridge, MA, 1997), p. 174.

[24] M. R. Muldoon, D. S. Broomhead, J. P. Huke, and R. Hegger, (1998), Delay embedding in the presence of dynamical noise, Dyn. Stab. Sys. **13**, 175.

[25] A. Serletis, A. Shahmoradi, and D. Serletis (2007), Effect of noise on the bifurcation behavior of nonlinear dynamical systems, Chaos Solitons Fractals **33**, 914.

[26] J. P. M. Heald and J. Stark (2000), Estimation of noise levels for models of chaotic dynamical systems, Phys. Rev. Lett. **84**, 2366.

[27] D. Orrell (2005), Filtering chaos: A technique to estimate dynamical and observational noise in nonlinear systems, Int. J. Bifurcat. Chaos **15**, 99.

[28] M. Siefert, A. Kittel, R. Friedrich, and J. Peinke (2003), On a quantitative method to analyze dynamical and measurement noise, Europhys. Lett. **61**, 466.

[29] A. N. Kolmogorov (1931), Math. Ann. **140**, 415.

[30] J. E. Moyal (1949), Stochastic processes and statistical physics, J. R. Stat. Soc. **11** 195.

[31] K. Urbanowicz and J. A. Holyst (2003), Noise-level estimation of time series using coarse-grained entropy, Phys. Rev. E **67**, 046218.

[32] T. Higuchi (1988), Approach to an irregular time series on the basis of the fractal theory, Physica D **31**, 277.

[33] P. Grassberger and I. Procaccia (1983), Estimation of the Kolmogorov entropy from a chaotic signal, Phys. Rev. A **28**, 2591.

[34] G. Benettin, L. Galgani, and J. M. Strelcyn (1976), Kolmogorov entropy and numerical experiments, Phys. Rev. A **14**, 2338.

[35] J. L. Hindmarsh and R. M. Rose (1984), A model of neuronal bursting using three coupled first order differential equations, Proc. R. Soc. London B **221**, 87.

[36] D. Hansel and H. Sompolinsky (1992), Synchronization and computation in a chaotic neural network, Phys. Rev. Lett. **68**, 718.

[37] B. B. Mandelbrot (1985), Self-affine fractals and fractal dimension, Phys. Scr. **32**, 257.

[38] T. Higuchi (1989), Toukeisuri **37**, 209.

[39] B. B. Mandelbrot, *The Fractal Geometry of Nature* (Freeman, San Francisco, 1982).

[40] W. Rudin, *Principles of Mathematical Analysis* (McGraw-Hill, New York, 1967), p. 83.

[41] K. Kitajo, D. Nozaki, L. M. Ward, and Y. Yamamoto (2003), Behavioral stochastic resonance within the human brain, Phys. Rev. Lett. **90**, 218103.

[42] K. Rektorys, *Survey of Applicable Mathematics* (Iliffe Books, London, 1969), p. 1125.

[43] A. K. Engel, P. Fries, and W. Singer (2001), Dynamic predictions: oscillations and synchrony in top - down processing, Nature Rev. Neurosci. **2**, 704.

[44] W. Klimesch (1999), EEG alpha and theta oscillations reflect cognitive and memory performance: a review and analysis, Brain Res. Rev. **29**, 169.

[45] J. Csicsvari, B. Jamieson, K. D. Wise, and G. Buzsáki (2003), Mechanisms of gamma oscillations in the hippocampus of the behaving rat, Neuron **37**, 311.

[46] N. Kopell, G. B. Ermentrout, M. Whittington, and R. D. Traub (2000), Gamma rhythms and beta rhythms have different synchronization properties, Proc. Natl. Acad. Sci. U.S.A. **97**, 1867.

[47] M. Steriade (2001), Impact of network activities on neuronal properties in corticothalamic systems, J. Neurophysiol. **86**, 1.

[48] W. J. Freeman, L. J. Rogers, M. D. Holmes, and D. L. Silbergeld (2000), Spatial spectral analysis of human electrocorticograms including the alpha and gamma bands, J. Neurosci. Methods **95**, 111.

[49] A. Sirota, J. Csicsvari, D. Buhl, and G. Buzsáki (2003), Communication between neocortex and hippocampus during sleep in rodents, Proc. Natl. Acad. Sci. U.S.A. **100**, 2065.

[50] T. Tateno, A. Harsch, and H. P. C. Robinson (2004), Threshold firing frequency - current relationships of neurons in rat somatosensory cortex: type 1 and type 2 dynamics, J. Neurophysiol. **92**, 2283.

[51] H. Markram and M. Tsodyks (1996), Redistribution of synaptic efficacy between neocortical pyramidal neurons, Nature **382**, 807.

[52] H. Markram, Y. Wang, and M. Tsodyks (1998), Differential signaling via the same axon of neocortical pyramidal neurons, Proc. Natl. Acad. Sci. U.S.A. **95**, 5323.

[53] A. M. Thomson (2000), Facilitation, augmentation and potentiation at central synapses, Trends Neurosci. **23**, 305.

[54] Y. Wang, H. Markram, P. H. Goodman, T. K. Berger, J. Ma, and P. S. Goldman-Rakic (2006), Heterogeneity in the pyramidal network of the medial prefrontal cortex, Nat. Neurosci. **9**, 534.

[55] G. Mongillo, O. Barak, and M. Tsodyks (2008), Synaptic theory of working memory, Science **319**, 1543.

[56] Y. Katori, K. Sakamoto, N. Saito, J. Tanji, H. Mushiake, and K. Aihara (2011), Representational switching by dynamical reorganization of attractor structure in a network model of the prefrontal cortex, PLoS. Comput. Biol. **7**, doi: 10.1371/journal.pcbi.1002266.

[57] Y. Igarashi, M. Oizumi, and M. Okada (2010), Mean field analysis of stochastic neural network models with synaptic depression, J. Phys. Soc. Jpn. **79**, 84001.

[58] Y. Katori, Y. Otsubo, M. Okada, and K. Aihara (2013), Stability analysis of associative memory network composed of stochastic neurons and dynamic synapses, Front. Comput. Neurosci. **21**, doi: 10.3389/fncom.2013.00006.

[59] J. F. Mejias and J. J. Torres (2009), Maximum memory capacity on neural networks with short-term synaptic depression and facilitation, Neural Comput. **21**, 851.

[60] M. Tsodyks, K. Pawelzik, and H. Markram (1998), Neural networks with dynamic synapses, **10**, 821.

[61] K. Kamiyama, M. Komuro, T. Endo, and K. Aihara (2014), Classification of Bifurcations of Quasi-Periodic Solutions Using Lyapunov Bundles, Int. J. Bifurcation Chaos **24**, 1430034.

[62] A. Fisahn, F. G. Pike, E. H. Buhl, and O. Paulsen (1998), Cholinergic induction of network oscillations at 40 Hz in the hippocampus in vitro, Nature **394**, 186.

[63] E. O. Mann, J. M. Suckling, N. Hajos, S. A. Greenfield, and O. Paulsen (2005), Perisomatic feedback inhibition underlies cholinergically induced fast network oscillations in the rat hippocampus in vitro, Neuron **45**, 105.

[64] J. J. Chrobak and G. Buzsáki (1998), Gamma oscillations in the entorhinal cortex of the freely behaving rat, J. Neurosci. **18**, 388.

Appendix A

How to determine the threshold value c^* in Eq. (2.10)

In this appendix, a procedure for determining the threshold value c^* for a given observational signal is presented. This threshold value provides a boundary between short and long time series for the TSD analysis. An optimal length or analysis window for the TSD is assessed, based on the threshold value and accordingly, the time series within the analysis window will be converted to the TSD in turn along the time axis. Actually depending on the length of time series, the function of the TSD can be changed from the viewpoint of the monotonic behavior, which can be seen between the TSD and the level of dynamical noise [Fig. 2.6]. The diagrams, consisting of the two upper bounds ϵ_1 and ϵ_2 [Eq. (2.8) and Eq. (2.9)] with the monotonic properties, are described. On the diagrams, the similarity among typical monotonic properties—for which the upper bounds can be selected reasonably for a given observational signal—is plotted.

Here we regard a monotonic property consisting of TSDs, as a function of the two upper bounds ϵ_1 and ϵ_2. Furthermore, assume that ϵ_1 and ϵ_2 vary from 1 to 9.5 and from 0.01 to 0.095, respectively; note that if these bounds are set to very large values, they cannot work as the plausible boundary because short time series defined in the sense of this study mean that the time series is referred to as a process close to a semi-stationary process; i.e., it only includes small discrepancies between stationarity and nonstationarity [Fig. 2.1]. We have generated the (ϵ_1, ϵ_2) diagrams in terms of the similarity among the following four systems: (I) the harmonic oscillator system, (II) the Lorenz system, (III) the Rössler system, and (IV) the coupled Hindmarsh-Rose neuronal system [Eqs. (2.18) to (2.32)], depicted in Fig. A.1(a), in which each parameter point indicates the similarity among four monotonic properties generated from the systems. This similarity has been

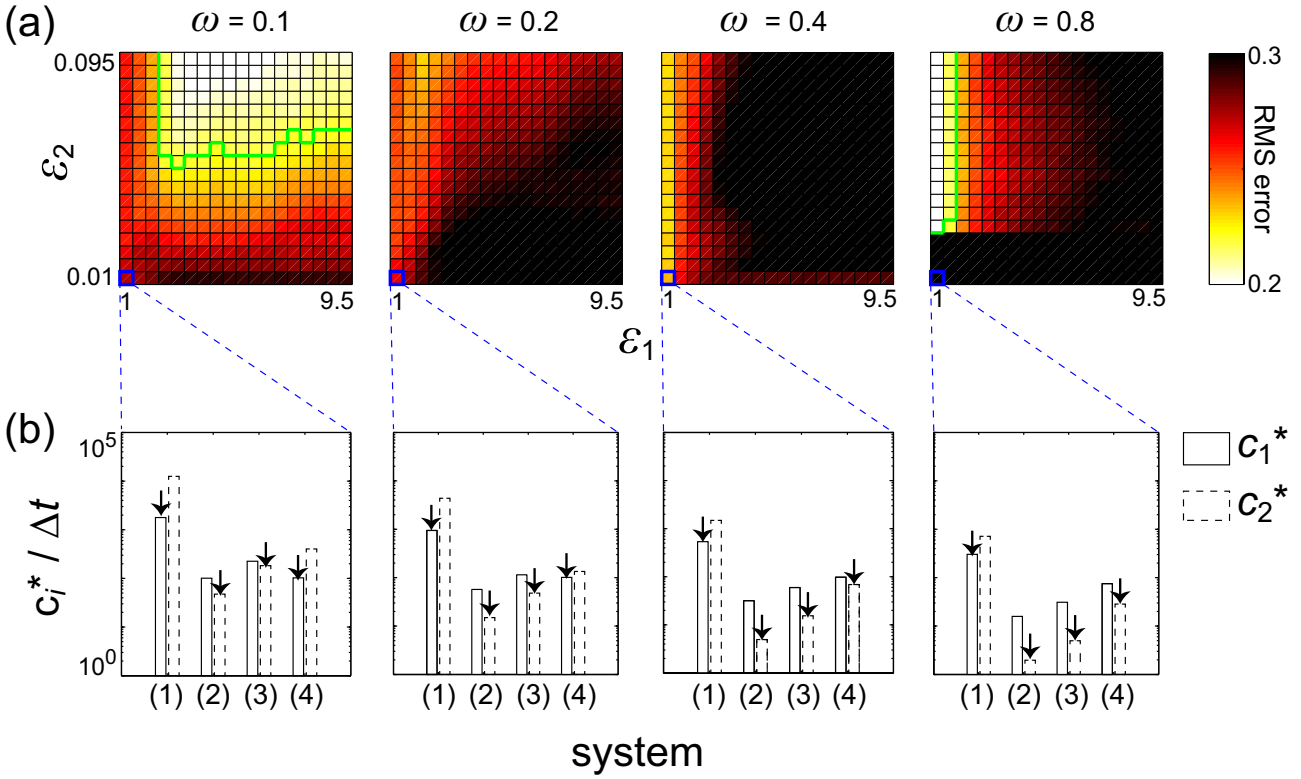

Figure A.1. Effects of the two upper bounds ϵ_1 and ϵ_2, on the monotonic property of the TSD. (a) The (ϵ_1, ϵ_2) diagrams in accordance with the noise level ω from left to right: 0.1, 0.2, 0.4, and 0.8. The horizontal axis is ϵ_1 ranged from 1 to 9.5 in steps of 0.5, while the vertical axis is ϵ_2 ranged from 0.01 to 0.095 in steps of 0.005. Each parameter point on the diagrams represents the similarity of the monotonic properties among four systems: (I) the harmonic oscillator system, (II) the Lorenz system, (III) the Rössler system, and (IV) the coupled Hindmarsh-Rose neuronal system, where the similarity was evaluated by the RMS error so that a smaller error is indicated by a lighter color. The two green curves are boundaries of the RMS error of 0.22. (b) Examples of threshold values for c_1^* and c_2^* on a point $(\epsilon_1, \epsilon_2) = (1, 0.01)$, indicated by open blue rectangles in (a). The vertical axes are displayed by the log scale. The arrows indicate the threshold values of c^*, by which we set the length of short time series and calculated RMS errors for (a); namely, we used $\lfloor c^*/\Delta t \rfloor$ as the length of each short time series.

measured by the RMS error defined as follows:

$$RMS = \sqrt{\frac{1}{|\Omega|(V^2-V)}\sum_{\omega\in\Omega}\sum_{e=1}^{V}\sum_{f\neq e}\left|\tilde{D}^{(e)}_{\rm mean}(\omega\vec{\rho_e}) - \tilde{D}^{(f)}_{\rm mean}(\omega\vec{\rho_f})\right|^2}, \tag{A.1}$$

$$\tilde{D}^{(e)}_{\rm mean}(\omega\vec{\rho_e}) = \frac{1}{100}\sum_{\lambda=1}^{100}\tilde{D}^{(e)}_{\lambda}(\omega\vec{\rho_e}), \tag{A.2}$$

where $\tilde{D}^{(e)}_{\lambda}(\omega\vec{\rho_e})$ denotes the TSD of a time series sampled with $\Delta t = 0.001$ observed from d-dimensional system (e) [Eqs. (2.18) to (2.32)], corresponding to the λth simulation; e represents the index of systems (I) through (IV) so that $V = 4$; ω is the level of dynamical noise, which indicates an element of a set $\Omega = \{0, 0.1, 0.2, ..., 1\}$; and $\vec{\rho_e} = (\sigma^{(e)}_{{\rm dyn}x_1}, \sigma^{(e)}_{{\rm dyn}x_2}, ..., \sigma^{(e)}_{{\rm dyn}x_d})$. Then, $\sigma^{(e)}_{{\rm dyn}x_q}$ for $q = 1, 2, ..., d$ is the standard deviation of a time series associated with the variable x_q included in system (e). Here $|\Omega|$ represents the number of elements in Ω, namely $|\Omega| = 11$. The size $|\vec{\rho_e}|$ of $\vec{\rho_e}$ differs among systems; that is, $|\vec{\rho_1}|$, $|\vec{\rho_2}|$, $|\vec{\rho_3}|$, and $|\vec{\rho_4}|$ are respectively 2, 3, 3, and 300, each of which corresponds to the number of variables contained in system (e) [Eqs. (2.18) to (2.32)].

Towards an application of the (ϵ_1, ϵ_2) diagrams to the real-data analysis, in fact, we have used the same lengths of $\lfloor c^*/\Delta t \rfloor$ among the four systems, where $\lfloor\cdot\rfloor$ denotes the rounding down; the length $\lfloor c^*/\Delta t \rfloor$ corresponds to the upper limit value of the length of short time series. For the sake of clarity, the above simulation has reflected transient behavior, where the initial condition of variables follows the uniform distribution between 0 and 1. We have applied time series data with the following four kinds of noise levels: 0.1, 0.2, 0.4, and 0.8, respectively, to a set of ϵ_1 and ϵ_2; i.e., we accumulated discrepancies between stationarity and nonstationarity until their accumulation reached ϵ_1 or ϵ_2 [Eqs. (2.4) to (2.9)], so that only the two (ϵ_1, ϵ_2) diagrams associated with the noise levels of 0.1 and 0.8 show the relatively small RMS errors less than 0.22 [see Fig. A.1(a)].

Here we show the two typical points on one (ϵ_1, ϵ_2) diagram realized with the noise level of 0.1 [Fig. A.2(a)] and on the other (ϵ_1, ϵ_2) diagram realized with the noise level of 0.8 [Fig. A,2(b)]; namely, point $(\epsilon_1, \epsilon_2) = (2.5, 0.06)$ for noise level 0.1 and point $(\epsilon_1, \epsilon_2) = (1, 0.03)$ for noise level 0.8. For the noise level of 0.1, the monotonic behavior can be clearly seen among the four systems [see Fig. A.2(a)]. In this case, $\lfloor c^*/\Delta t \rfloor$ of short time series were 4313, 179, 563, and 318 for systems (1) through (4), respectively. On the other hand, for the noise level of 0.8, the monotonic behavior has not been observed among three systems except for the harmonic oscillator system [see Fig. A.2(b)], because in this case, the lengths of short time series were 304, 4, 11, and 75 for systems (1) through (4), respectively. This irregularity tends to happen when the time series applied to ϵ_1 and ϵ_2 has been affected by the large dynamical noise level so that the length $\lfloor c^*/\Delta t \rfloor$ of short time series, especially generated from the Lorenz system, the Rössler system, and the coupled Hindmarsh-Rose neuronal system, has been very short [see Fig. A.1(b)]. Therefore, in order to select the

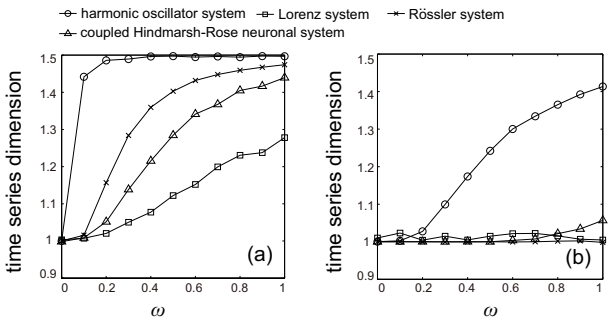

Figure A.2. Two examples of monotonic properties among four systems: (I) the harmonic oscillator system, (II) the Lorenz system, (III) the Rössler system, and (IV) the coupled Hindmarsh-Rose neuronal system, where for both panels (a) and (b), the RMS errors over monotonic properties were less than 0.22. The lengths of time series used here were obtained as the upper limit values $\lfloor c^*/\Delta t \rfloor$ of short time series, through the uses of ϵ_1 and ϵ_2 as in Fig. A1. (a) Monotonic behavior. The time series were observed through systems with the noise level of 0.1, and applied to $(\epsilon_1, \epsilon_2) = (2.5, 0.06)$. Each length of time series for systems (I) through (IV) was 4313, 179, 563, and 318, respectively. (b) When the noise level was fixed to 0.8 and $(\epsilon_1, \epsilon_2) = (1, 0.03)$, monotonic behavior did nor appear for all systems. Only the harmonic oscillator has shown the monotonic property. In this case, each length of time series for systems (I) through (IV) was 304, 4, 11, and 75, respectively.

upper bounds ϵ_1 and ϵ_2—which in turn set the upper limit value of the length of short time series—we should use nearly clean data, i.e. the noise level should be less than 0.1, especially when we have multivariate time series data and try to work their monotonic properties universally [Fig. 2.8].

Appendix B

Propagation of dynamical noise

In this appendix, how the property of dynamical noise propagates among variables and along the integrals is shown. Suppose that a two-dimensional stochastic dynamical system with state variables x_1 and x_2 is given by

$$\mathrm{d}x_1 = f_1(x_1, x_2)\mathrm{d}t + \rho_1 \mathrm{d}W_1(t), \tag{B.1}$$

$$\mathrm{d}x_2 = f_2(x_1, x_2)\mathrm{d}t + \rho_2 \mathrm{d}W_2(t), \tag{B.2}$$

where function $f_q(\cdot)$ with $q \in \{1, 2\}$ is linear or nonlinear, and the term $\rho_q \mathrm{d}W_q(t)$ denotes the dynamical noise such that the variable $\mathrm{d}W_q(t)$ follows a normal distribution with mean 0 and standard deviation $\sqrt{\mathrm{d}t}$.

Consider the effect of dynamical noises $\rho_1 \mathrm{d}W_1(t)$ and $\rho_2 \mathrm{d}W_2(t)$ on the variable x_1. As shown in Eq. (B.1), the variable x_1 is influenced by $W_1(t)$, where the property of the Wiener process $W_1(t)$ is sent to $x_1(t)$; we describe this situation using the following phrase: $W_1(t)$ drives $x_1(t)$. The function f_1 involves not only $x_1(t)$ but also $x_2(t)$, so that the dynamics of $x_2(t)$ is influential on that of $x_1(t)$; namely, $W_2(t)$ contributes to the time evolution of $x_1(t)$. However, $W_2(t)$ does not drive $x_1(t)$, i.e., the property of $W_2(t)$ is not directly transferred to $x_1(t)$, because $W_2(t)$ is integrated over t when the variable $x_2(t)$ within f_1 is substituted with the solution $x_2(t)$ of Eq. (B.2). Thus, instead of $W_2(t)$, the integrated Wiener process $V_2(t)$ drives $x_1(t)$, where one realization of the Wiener process can be regarded as a continuous function of time, and is integrable by means of the fundamental theorem of calculus. The aforementioned driving process has been illustrated in Fig. B.1. Because the process $V_2(t)$ is a smooth function, the TSD $\tilde{D}^{(1)}(\vec{\rho})$ of the time series associated with the variable x_1 is not changed due to dynamical noise $\rho_2 \mathrm{d}W_2(t)$, even if coefficient ρ_2 becomes large enough. Thus, the monotonic relationship between $\tilde{D}^{(q)}(\vec{\rho})$ and ρ_r ($r \in \{1, 2\}$) can be observed in the case of $r = q$. If $r \neq q$, the left-hand side of Eq. (2.43) becomes zero.

Next, we consider a two-dimensional linear stochastic dynamical system given by

$$\mathrm{d}x_1 = x_2\mathrm{d}t + \rho_1 \mathrm{d}W_1(t), \tag{B.3}$$

$$\mathrm{d}x_2 = -x_1\mathrm{d}t + \rho_2 \mathrm{d}W_2(t), \tag{B.4}$$

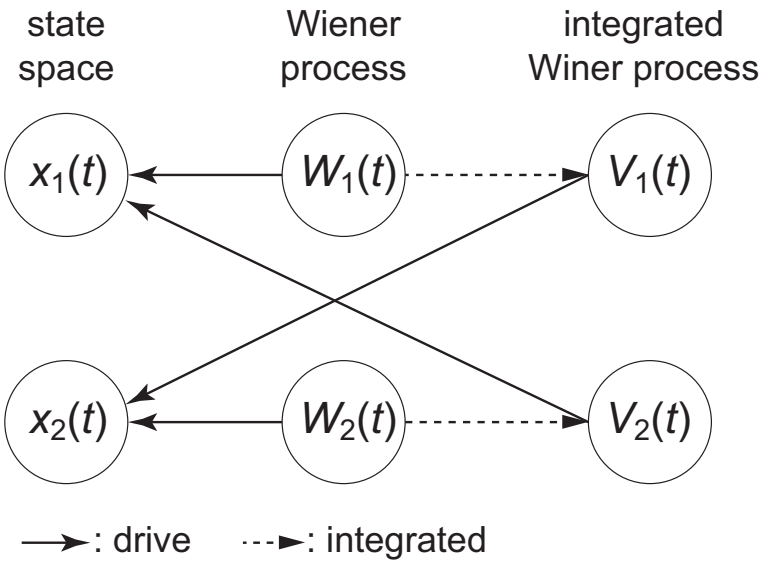

Figure B.1. Directions of driving forces in a two-dimensional dynamical stochastic system. Stochastic variables $W_1(t)$ and $V_2(t)$ drive only $x_1(t)$, whereas $W_2(t)$ and $V_1(t)$ drive only $x_2(t)$.

where $f_1(x_1, x_2)$ and $f_2(x_1, x_2)$ have been substituted with x_2 and $-x_1$ in Eqs. (B.1) and (B.2), respectively. Provided the initial condition $x_1(0) = 1$ and $x_2(0) = 0$, the following solution can be obtained:

$$x_1(t) = \cos(t) + \rho_1\{\cos(t) * \eta_1(t)\} + \rho_2\{\sin(t) * \eta_2(t)\}, \tag{B.5}$$

$$x_2(t) = -\sin(t) - \rho_1\{\sin(t) * \eta_1(t)\} + \rho_2\{\cos(t) * \eta_2(t)\}, \tag{B.6}$$

where the variable $\eta_q(t)$ denotes white Gaussian noise such that $\eta_q(t) = \mathrm{d}W_q(t)/\mathrm{d}t$.

Convolutions $\cos(t) * \eta_q(t)$ and $\sin(t) * \eta_q(t)$ reflect the properties of the Wiener process $W_q(t)$ and the integrated Wiener process $V_q(t)$, respectively [see Fig. B.2]. In the convolution,

$$\begin{aligned} \xi^{(\cos)}(t) &= \cos(t) * \eta_q(t) \\ &= \int_0^t \eta_q(\psi)\cos(t-\psi)\mathrm{d}\psi, \end{aligned} \tag{B.7}$$

the term $\cos(t)$ integrates the Gaussian noise $\eta_q(t)$. This characteristic of $\cos(t)$ is similar to the step function. In the process of Eq. (B.7), $\cos(t-\psi)$ indicates 1 when $\psi = t$ and generates a curve along the time axis until $\psi = 0$, where time ψ goes to the past. Suppose that time t goes up to $t + \delta t$ in which $\delta t > 0$ and δt is a small deviation. Here, within the small area between $\psi = t$ and $\psi = t + \delta t$, $\cos(t + \delta t - \psi)$ is almost 1, and therefore, the term $\cos(t)$ in Eq. (B.7) has the role of integrating the Gaussian noise $\eta_q(t)$. Further, in the convolution,

$$\begin{aligned} \xi^{(\sin)}(t) &= \sin(t) * \eta_q(t) \\ &= \int_0^t \eta_q(\psi)\sin(t-\psi)\mathrm{d}\psi, \end{aligned} \tag{B.8}$$

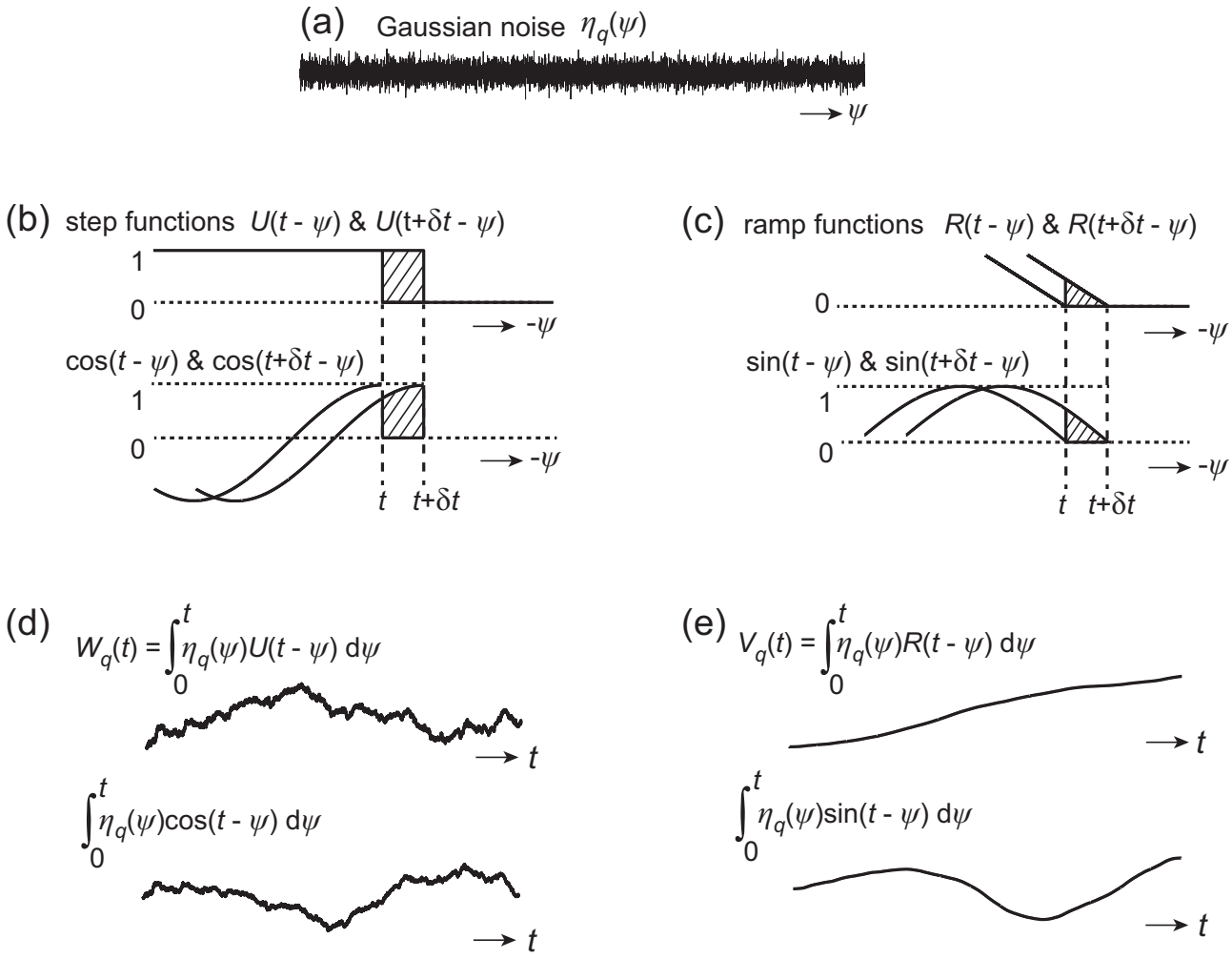

Figure B.2. A schematic representation of convolutions $\cos(t) * \eta_q(t)$ and $\sin(t) * \eta_q(t)$. The Gaussian noise (a) is integrated over t once or twice when it is convoluted with the step function $U(t)$ or with the ramp function $R(t)$, respectively. The function $\cos(t)$ also has the role of integrating the Gaussian noise once as well as the step function, as shown in (b), because the small area between $\cos(t-\psi)$ and $\cos(t+\delta t-\psi)$ is almost δt as well as that between $U(t-\psi)$ and $U(t+\delta t-\psi)$ (see shaded areas in (b)). Further, the function $\sin(t)$ has the role of integrating the Gaussian noise twice as well as the ramp function, as shown in (c), because the small area between $\sin(t-\psi)$ and $\sin(t+\delta t-\psi)$ resembles that between $R(t-\psi)$ and $R(t+\delta t-\psi)$ (see shaded areas in (c)). The wave forms corresponding to the Wiener process $W_q(t)$ and $\cos(t) * \eta_q(t)$ are shown in (d), whereas the wave forms corresponding to the integrated Wiener process $V_q(t)$ and $\sin(t) * \eta_q(t)$ are shown in (e).

the term $\sin(t)$ integrates the Gaussian noise $\eta_q(t)$ twice. This characteristic of $\sin(t)$ is similar to the ramp function. Note that the ramp function can be obtained by convoluting step functions. In Eq. (B.8), $\sin(t-\psi)$ is 0 when $\psi = t$. Suppose again that time t goes up to $t+\delta t$. Here, within the small area between $\psi = t$ and $\psi = t+\delta t$, $\sin(t+\delta t-\psi)$ behaves like a ramp function, and therefore, the term $\sin(t)$ in Eq. (B.8) has the role of integrating the Gaussian noise $\eta_q(t)$ twice. Thus, $W_1(t)$ and $V_2(t)$ drive $x_1(t)$, while $V_1(t)$ and $W_2(t)$ drive $x_2(t)$ [see Fig. B.1 and Eqs. (B.5) and (B.6)].

Appendix C

Theory of time series dimension

In this appendix, the monotonic relationship between the TSD $\tilde{D}^{(q)}(\vec{\rho})$ and the standard deviation $\vec{\rho}(t)$ of the time-dependent Gaussian dynamical noise is shown. First, the analytic solution of a linear stochastic dynamical system, obtained via the Laplace transform [42], is introduced. Next, an inequality for the monotonic relationship between the TSD and the noise level, occurring in linear stochastic dynamical systems, is derived. Finally, the success rate of the derived inequality—i.e. the ratio between the number of successful trials satisfying the aforementioned inequality, and the number of total trials—is numerically illustrated in the case of a harmonic oscillator.

C.1 Linear stochastic dynamical system

The linear stochastic dynamical system with state vector $\vec{x} = (x_1, x_2, ..., x_d)$ is given by

$$\mathrm{d}x_q = \left(\sum_{l=1}^{d} a_{ql} x_l\right) \mathrm{d}t + \rho_q(t)\mathrm{d}W_q(t), \text{ for } q = 1, 2, ..., d, \tag{C.1}$$

where $\rho_q(t)$ is an element of $\vec{\rho}(t) = (\rho_1(t), \rho_2(t), ..., \rho_d(t))$. This system is the linear version of Eq. (2.1), where $f_q(\vec{x})$ is substituted with the linear combination of $\vec{x}$; a_{ql} represents the connection from the variable x_l to the variable x_q. Note that Eq. (C.1) denotes a d-dimensional linear stochastic dynamical system. Under any initial condition, if the temporal change of $\rho_q(t)$ is negligible compared to that of the deterministic component, the solution $x_q(t)$ of Eq. (C.1) is represented by

$$\begin{aligned} x_q(t) &= F_q(t) + \sum_{l=1}^{d} \rho_l(t) \{G_{ql}(t) * \eta_l(t)\} \\ &= F_q(t) + \sum_{l=1}^{d} \rho_l(t) \xi_{ql}(t), \end{aligned} \tag{C.2}$$

where $\eta_q(t) = \mathrm{d}W_q(t)/\mathrm{d}t$ follows a normal distribution of mean 0 and standard deviation 1. The functions $F_q(t)$ and $G_{ql}(t)$ are time-dependent and contribute to the deterministic component and stochastic components, respectively; $G_{ql}(t) * \eta_l(t)$ denotes the convolution

between the terms $G_{ql}(t)$ and $\eta_l(t)$. We cannot give an explicit form of the functions $F_q(t)$ and $G_{ql}(t)$, but let us show an example of them by considering the following two-dimensional dynamics:

$$\begin{aligned} \mathrm{d}x_1 &= x_2\mathrm{d}t + \rho_1\mathrm{d}W_1(t), && \text{(C.3)} \\ \mathrm{d}x_2 &= -x_1\mathrm{d}t + \rho_2\mathrm{d}W_2(t), && \text{(C.4)} \end{aligned}$$

where we have set $(a_{11}, a_{12}, a_{21}, a_{22}) = (0, 1, -1, 0)$ in Eq. (C.1). Additionally, we have assumed that ρ_1 and ρ_2 are constant over time, for simplicity. By applying the Laplace transform to the above system and considering initial condition $x_1(0) = 1$ and $x_2(0) = 0$, we obtain

$$\begin{aligned} x_1(t) &= \cos(t) + \rho_1 \left\{\cos(t) * \eta_1(t)\right\} + \rho_2 \left\{\sin(t) * \eta_2(t)\right\} \\ &= \cos(t) + \sum_{l=1}^{2} \rho_l \xi_{1l}(t), && \text{(C.5)} \end{aligned}$$

and

$$\begin{aligned} x_2(t) &= -\sin(t) - \rho_1 \left\{\sin(t) * \eta_1(t)\right\} + \rho_2 \left\{\cos(t) * \eta_2(t)\right\} \\ &= -\sin(t) + \sum_{l=1}^{2} \rho_l \xi_{2l}(t), && \text{(C.6)} \end{aligned}$$

for $t \geq 0$.

C.2 Monotonic relationship between time series dimension and noise level

We derive the inequality for the monotonic relationship between $\tilde{D}^{(q)}(\vec{\rho})$ and ρ_q, holding in a linear stochastic dynamical system [Eq. (C.1)]. First, the curve length [Eq. (2.34) and Eq. (2.35)] is written in terms of the time series associated with the variable x_q as given in Eq. (C.2). This yields

$$\tilde{L}^{(q)}(\zeta_k, \vec{\rho}) = \frac{(N-1)}{k^2 \zeta_k} \sum_{m=1}^{k} \left[\frac{1}{\lfloor \frac{N-m}{k} \rfloor} \sum_{j=1}^{\lfloor \frac{N-m}{k} \rfloor} \left| J_{\vec{\rho}}^{(q)}(m, j, k) \right| \right], \qquad \text{(C.7)}$$

where

$$\begin{aligned} J_{\vec{\rho}}^{(q)}(m, j, k) = & \left\{ F_q((m + jk)\Delta t) + \sum_{l=1}^{d} \rho_l \xi_{ql}((m + jk)\Delta t) \right\} \\ & - \left\{ F_q((m + (j-1)k)\Delta t) + \sum_{l=1}^{d} \rho_l \xi_{ql}((m + (j-1)k)\Delta t) \right\}. \end{aligned} \qquad \text{(C.8)}$$

In the above expressions and the latter arguments, we have denoted $\vec{\rho}(i\Delta t)$ as $\vec{\rho}$ for simplicity. As a next step, we define the following sets:

$$\Omega_{\mathrm{pq}}(\vec{\rho},m,k) := \left\{ j \mid J^{(q)}_{\vec{\rho}}(m,j,k) > 0 \right\}, \tag{C.9}$$

$$\Omega_{\mathrm{zq}}(\vec{\rho},m,k) := \left\{ j \mid J^{(q)}_{\vec{\rho}}(m,j,k) = 0 \right\}, \tag{C.10}$$

$$\Omega_{\mathrm{nq}}(\vec{\rho},m,k) := \left\{ j \mid J^{(q)}_{\vec{\rho}}(m,j,k) < 0 \right\}. \tag{C.11}$$

Then, the summation over j in Eq. (C.9) can be written in the following form:

$$\sum_{j=1}^{\lfloor \frac{N-m}{k} \rfloor} \left| J^{(q)}_{\vec{\rho}}(m,j,k) \right| = \sum_{j\in\Omega_{\mathrm{pq}}(\vec{\rho},m,k)} J^{(q)}_{\vec{\rho}}(m,j,k) - \sum_{j\in\Omega_{\mathrm{nq}}(\vec{\rho},m,k)} J^{(q)}_{\vec{\rho}}(m,j,k). \tag{C.12}$$

Next, in order to perform piecewise differentiation of $\tilde{L}^{(q)}(\zeta_k,\vec{\rho})$ with respect to ρ_q, we have removed the non-smooth points by using the set defined as

$$\Psi^{(q)}(m,k) := \left\{ \vec{\rho} \,\middle|\, \Omega_{\mathrm{zq}}(\vec{\rho},m,k) = \emptyset \right\}, \tag{C.13}$$

which sorts the differentiable domains. Consequently, with $\vec{\rho}\in\Psi^{(q)}(m,k)$, Eq. (C.9) can be converted to a piecewise smooth function as follows:

$$\tilde{L}^{(q)}_{\mathrm{pw}}(\zeta_k,\vec{\rho}) = \frac{(N-1)}{k^2\zeta_k} \sum_{m=1}^{k} \left[\frac{1}{\lfloor \frac{N-m}{k} \rfloor} \left\{ \sum_{j\in\Omega_{\mathrm{pq}}(\vec{\rho},m,k)} J^{(q)}_{\vec{\rho}}(m,j,k) - \sum_{j\in\Omega_{\mathrm{nq}}(\vec{\rho},m,k)} J^{(q)}_{\vec{\rho}}(m,j,k) \right\} \right], \tag{C.14}$$

where subindex "pw" in the left-hand side has been used to indicate that the function is piecewisely and sufficiently smooth with respect to $\vec{\rho}$. Therefore, its derivative with respect to ρ_q exists and is given by

$$\begin{aligned} \frac{\partial \tilde{L}^{(q)}_{\mathrm{pw}}(\zeta_k,\vec{\rho})}{\partial \rho_q} = \frac{(N-1)}{k^2\zeta_k} \sum_{m=1}^{k} \Bigg[\frac{1}{\lfloor \frac{N-m}{k} \rfloor} \Bigg\{ & \sum_{j\in\Omega_{\mathrm{pq}}(\vec{\rho},m,k)} \{\xi_{qq}((m+jk)\Delta t) - \xi_{qq}((m+(j-1)k)\Delta t)\} \\ & - \sum_{j\in\Omega_{\mathrm{nq}}(\vec{\rho},m,k)} \{\xi_{qq}((m+jk)\Delta t) - \xi_{qq}((m+(j-1)k)\Delta t)\} \Bigg\} \Bigg], \end{aligned} \tag{C.15}$$

where we have used the fact that elements and sizes of sets $\Omega_{\mathrm{pq}}(\vec{\rho},m,k)$ and $\Omega_{\mathrm{nq}}(\vec{\rho},m,k)$ are not changed due to differentiation with respect to ρ_q; namely, $\Omega_{\mathrm{pq}}(\vec{\rho},m,k) = \Omega_{\mathrm{pq}}(\vec{\rho}+\mathrm{d}\vec{\rho}_q,m,k)$ and $\Omega_{\mathrm{nq}}(\vec{\rho},m,k) = \Omega_{\mathrm{nq}}(\vec{\rho}+\mathrm{d}\vec{\rho}_q,m,k)$ where $\mathrm{d}\vec{\rho}_q$ is a small deviation around ρ_q such that $\mathrm{d}\vec{\rho}_q = (0,0,...,\mathrm{d}\rho_q,...,0,0)$, and $\mathrm{d}\vec{\rho}_q$ implicitly depends on time. Finally, by substituting Eqs. (C.14) and (C.15) in Eq. (2.42), the inequality

$$\frac{1}{\tilde{L}^{(q)}_{\mathrm{pw}}(\zeta_1,\vec{\rho})} \frac{\partial \tilde{L}^{(q)}_{\mathrm{pw}}(\zeta_1,\vec{\rho})}{\partial \rho_q} > \frac{1}{\tilde{L}^{(q)}_{\mathrm{pw}}(\zeta_2,\vec{\rho})} \frac{\partial \tilde{L}^{(q)}_{\mathrm{pw}}(\zeta_2,\vec{\rho})}{\partial \rho_q} \tag{C.16}$$

is obtained. If the above inequality is satisfied, and if $\tilde{L}^{(q)}(\zeta_k, \vec{\rho})$ [Eq. (C.7)] is a continuous function, then a monotonic relationship between the TSD $\tilde{D}^{(q)}(\vec{\rho})$ and ρ_q is achieved as a whole. We can easily prove that the absolute function in Eq. (C.7) is continuous by using the (ϵ, δ)-definition of limit [40], and then $\tilde{L}^{(q)}(\zeta_k, \vec{\rho})$ is also continuous. Note that the inner operation, the increment of $X_{\vec{\rho}}(t)$, of the absolute function is continuous with respect to $\vec{\rho}$ because $X_{\vec{\rho}}(t)$ changes with $\vec{\rho}$. This conditional equation is built on the appropriate values of Δt, N, and $\vec{\rho}$. Note that $\tilde{L}^{(q)}_{\rm pw}(\zeta_1, \vec{\rho})$ and $\tilde{L}^{(q)}_{\rm pw}(\zeta_2, \vec{\rho})$ can easily be obtained from Eq. (C.14) by using $k = 1$ and $k = 2$, respectively. Likewise, $\partial\tilde{L}^{(q)}_{\rm pw}(\zeta_1, \vec{\rho})/\partial\rho_q$ and $\partial\tilde{L}^{(q)}_{\rm pw}(\zeta_2, \vec{\rho})/\partial\rho_q$ can be obtained from Eq. (C.15) by considering $k = 1$ and $k = 2$, respectively.

The aforementioned analysis can be summarized in the following proposition.

Proposition C.2.1 (Monotonic relationship between the TSD and the noise level)**.** *Consider the d-dimensional linear stochastic system [Eq. (C.1)]. Assume that only the variable x_q is observed during the observational process and that observational noise does not influence the process. Then, if condition Eq. (C.16) is satisfied, there exists a monotonic relationship between the TSD $\tilde{D}^{(q)}(\vec{\rho})$ and the noise level $\rho_q(t)/\sigma_{{\rm dyn}x_q}(t)$.*

The $(L_{\rm seg}(0, \Delta t), \rho_q/\sigma_{{\rm dyn}x_q})$ diagram [see Fig. C.1] shows the success rate in which the derived inequality [Eq. (C.18)] holds given a noise level (uniformly distributed between 0.01 and 1) and length (uniformly distributed between 10 and 500) of a time series taken from the harmonic oscillator system [Eq. (C.3) and Eq. (C.4)] simulated with the initial condition $x_1(0) = 1$ and $x_2(0) = 0$. The variable $x_1(t)$ was used as a target time series; namely, its curve length $\tilde{L}^{(1)}(\zeta_k, \vec{\rho})$ was calculated. We calculated the inequality [Eq. (C.16)] 100 times on each parameter point in the diagram to obtain the success rate. We define the success rate as the ratio between the number of successful simulations satisfying the inequality [Eq. (C.16)] and the number of total simulations. In this simulation, ρ_1 and $\sigma_{{\rm dyn}x_1}$ were constant for each trial. Then, the dynamical noise level of $x_2(t)$ was fixed at 0.1 for each trial. The sampling time Δt was set to 0.001. As a result, a larger size of data satisfies the inequality in a wider range of the noise level. Note that when the inequality is simulated, ${\rm Prob}[J^{(q)}_{\vec{\rho}}(m, j, k) = 0] = 0$ because $\vec{\rho}$ is optionally given, and thereby any used $\hat{\rho}_q$ is within (S, E), that is $\hat{\rho}_q \in \Omega^{(S,E)}_q$ [see Eq. (2.40) and Eq. (2.41)]. Moreover, we have revealed that the original inequality [Eq. (43)] also shows the same diagram with Fig. C.1, where $\tilde{D}^{(1)}_{\rm pw}(\rho_1 + 0.0001, \rho_2) - \tilde{D}^{(1)}_{\rm pw}(\rho_1, \rho_2)$ was used for calculation of the success rate. Then, the correlation coefficient between success rates of the original and the derived inequalities is more than 0.999. Thus, the derived inequality is valid for linear stochastic dynamical systems.

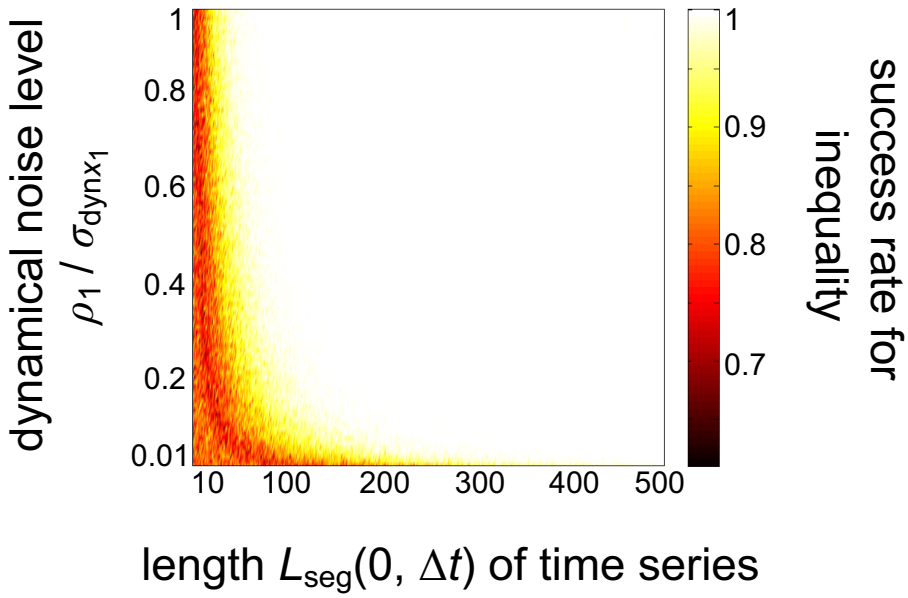

Figure C.1. The $(L_{\mathrm{seg}}(0, \Delta t), \rho_1/\sigma_{\mathrm{dyn}x_1})$ diagram in which the harmonic oscillator system was simulated. A larger success rate for the inequality is indicated by a lighter color.

Appendix D

TSD analysis results on EEG signals

In this appendix, multivariate TSD time series derived from 63-dimensional EEG data are shown. For the channel location on the human brain, the readers are referred to Fig. D.1. The EEG data during a cycle consists of measurements recording two distinctive brain states: eyes-open state and eyes-closed state, where the length of each state was 35 s so that the total length of the cycle was 70 s. This cycle was repeated 10 times and accordingly, TSD time series among 10 trials as well as the mean TSD time series over 10 trials are depicted [see Figs. D.2 to D.13].

To understand which site exhibits the difference between the eyes-open and eyes-closed states visually, two-dimensional topographies plotting TSD values are presented with respect to each trial and to each state [see Figs. D.14 to D.18]. Clearly, sites located in the frontal lobe change their noise levels due to visual inputs, especially for subject 1 [see Fig. D.17].

One can suppose that a TSD time series is the temporal change of a set of variables $\rho_1(t)$, $\rho_2(t)$,...,$\rho_{63}(t)$ [Eq. (2.1)] and that the corresponding set of variables x_1, x_2..., x_{63} is a part of dynamics generating EEG data so that the underlying system can be regarded as a system composed of coordinates with more than 63 dimensions. However, perhaps an EEG data is not multivariate, that is, there exists a possibility that each EEG signal belongs to its specific system so that EEG signals cannot be analyzed collectively.

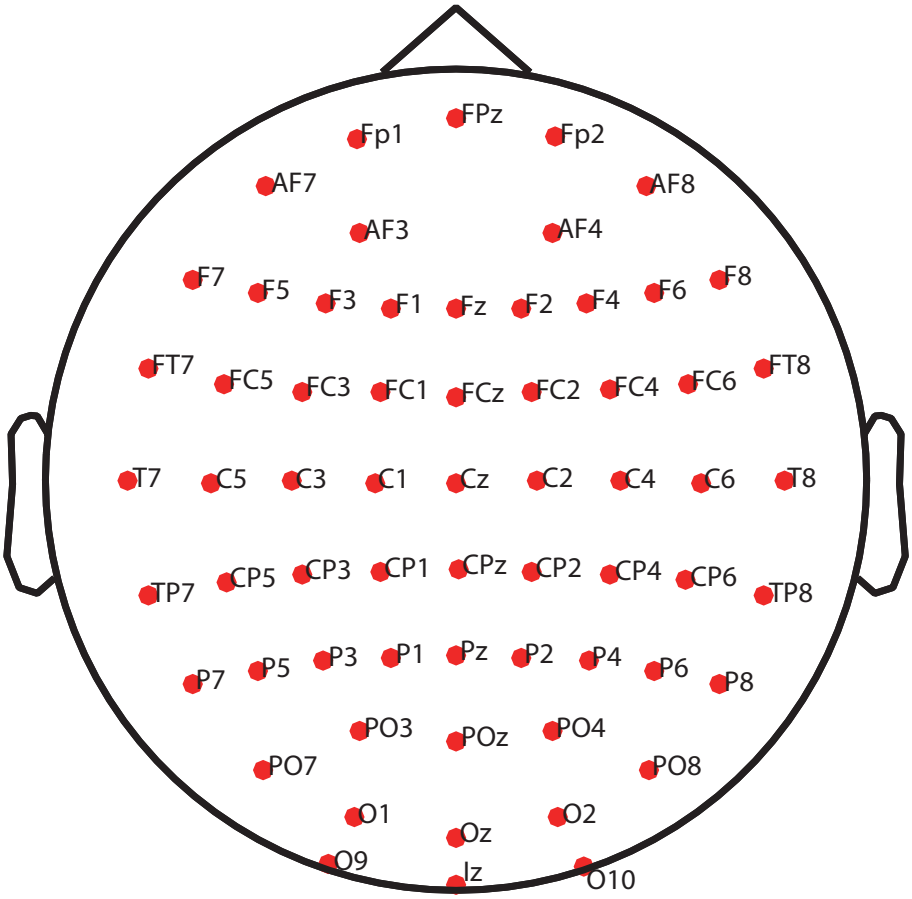

Figure D.1. A channels location on the human brain.

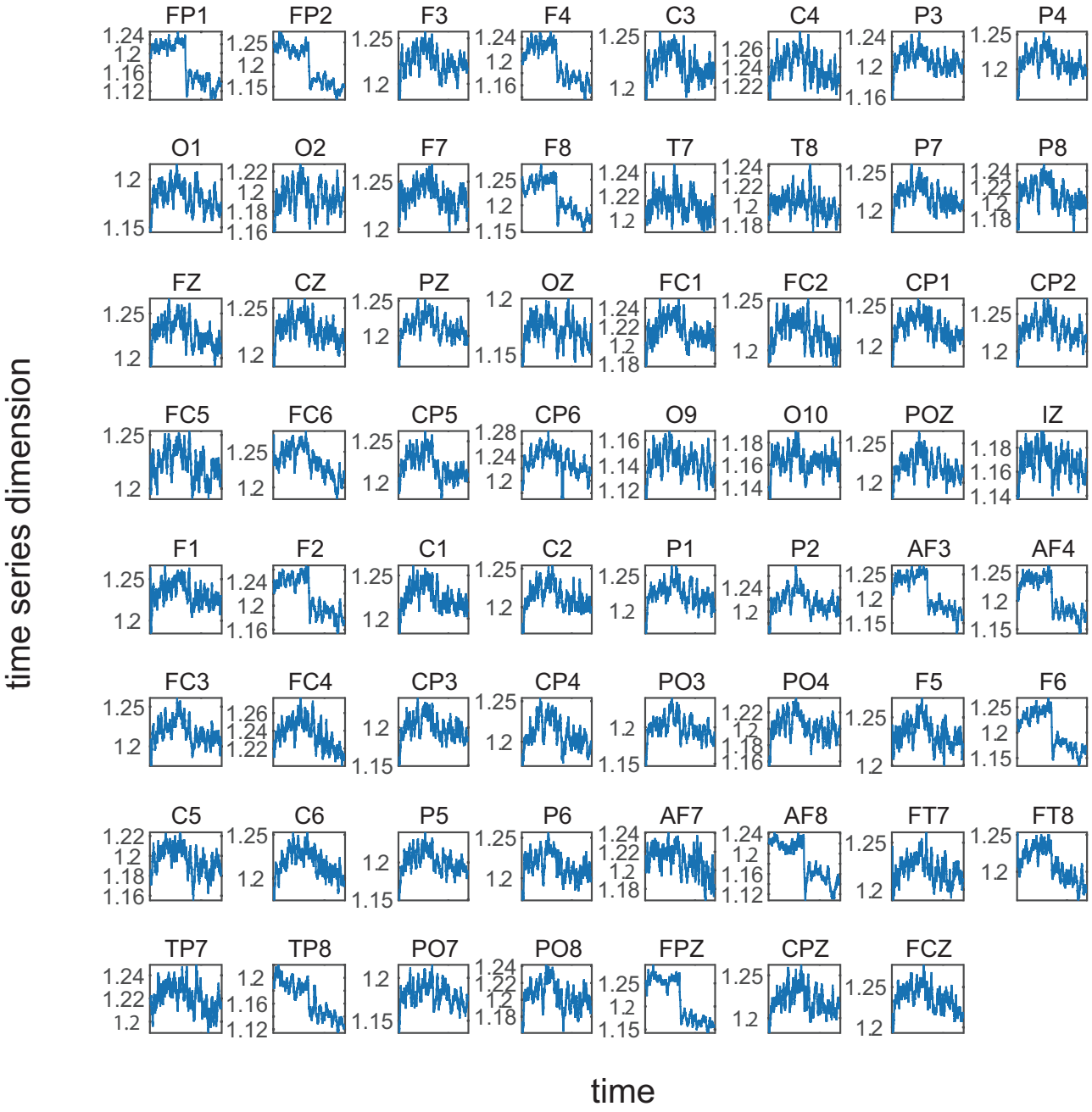

Figure D.2. TSD time series converted from EEG data obtained from 63 channels during trial 1. Displaying 70 s, first half of which corresponds to the eyes-open state, while latter half corresponds to the eyes-closed state.

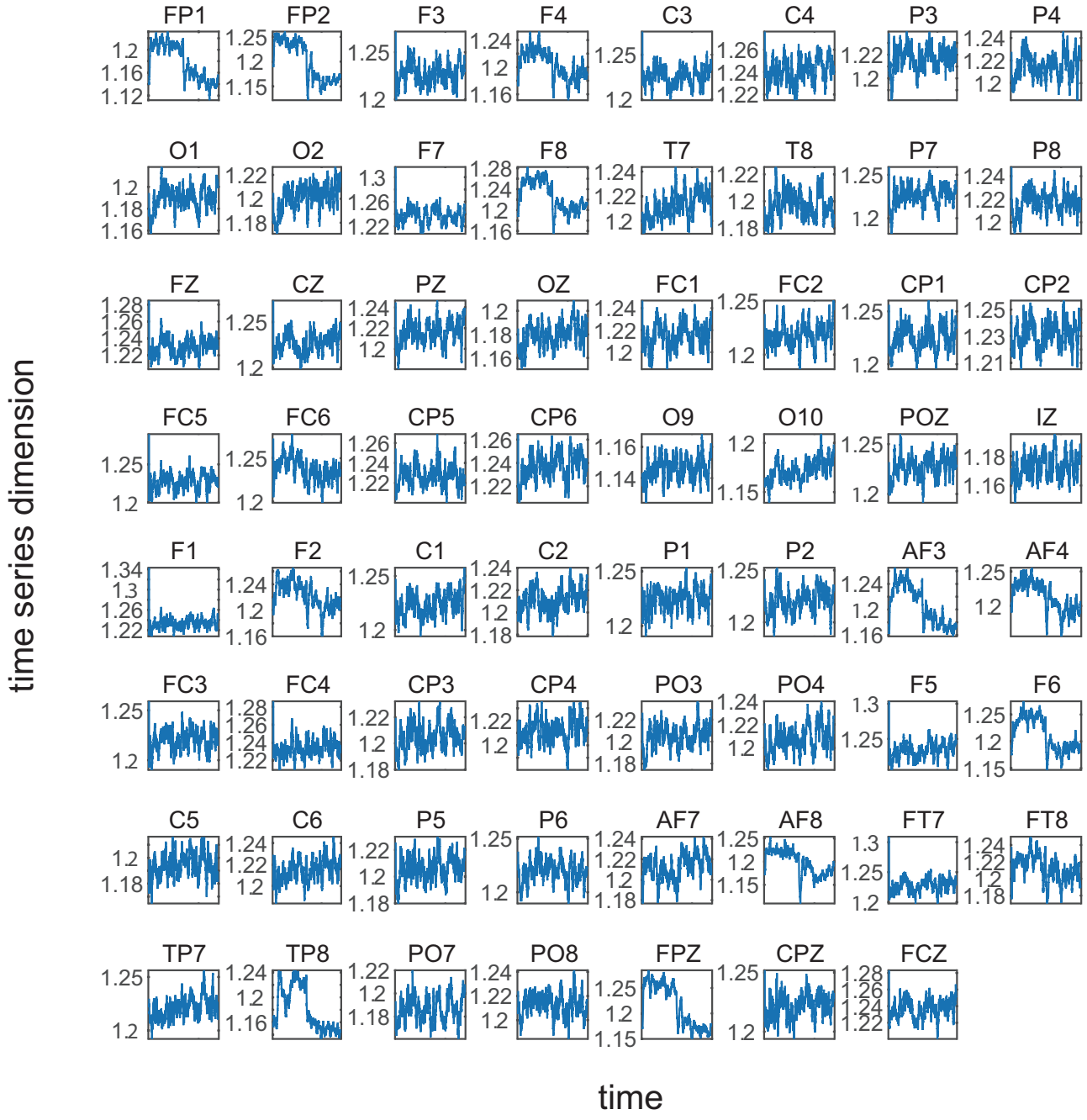

Figure D.3. TSD time series converted from EEG data obtained from 63 channels during trial 2. The notation of the time axis is the same with Fig. D.2.

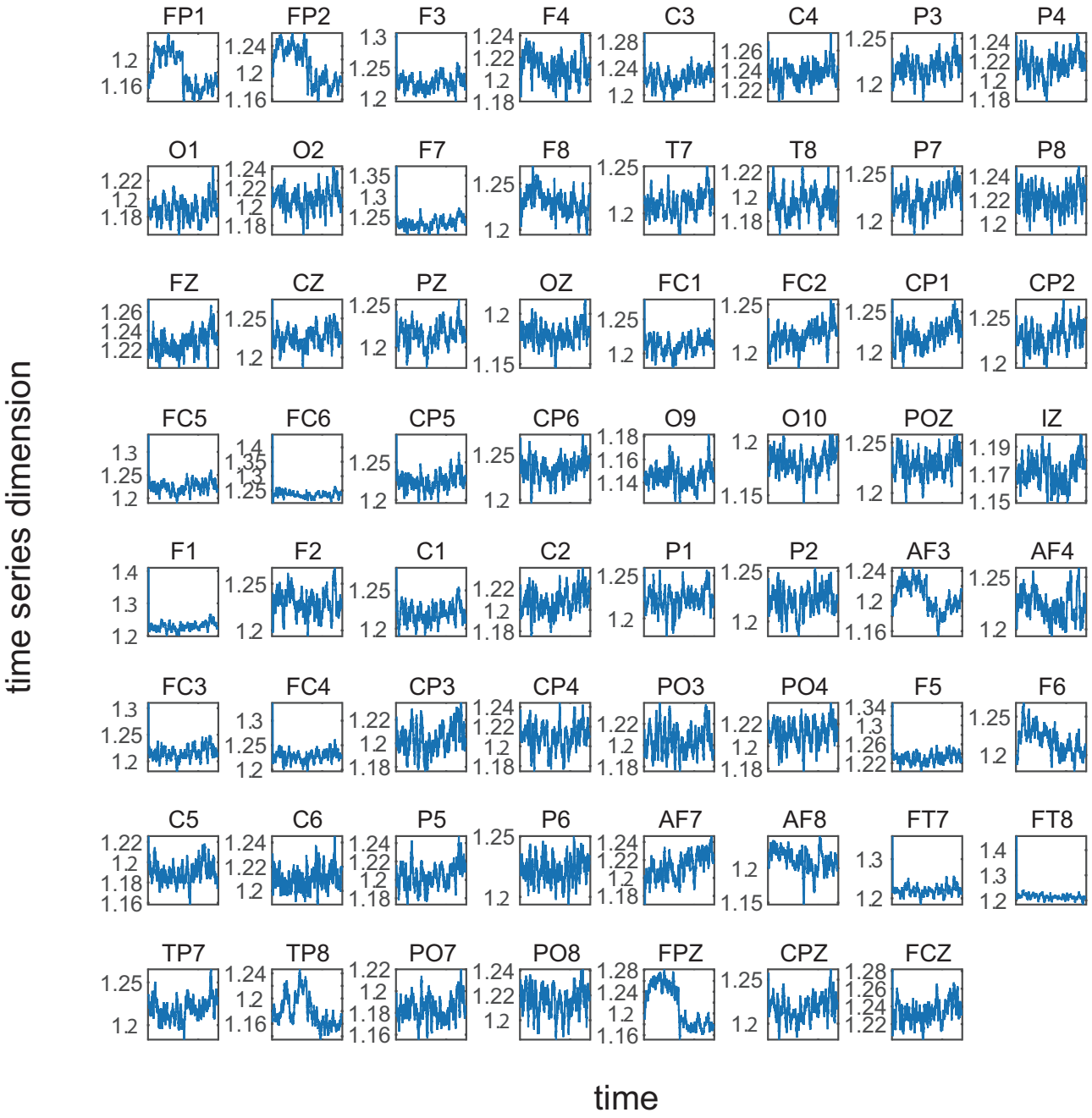

Figure D.4. TSD time series converted from EEG data obtained from 63 channels during trial 3. The notation of the time axis is the same with Fig. D.2.

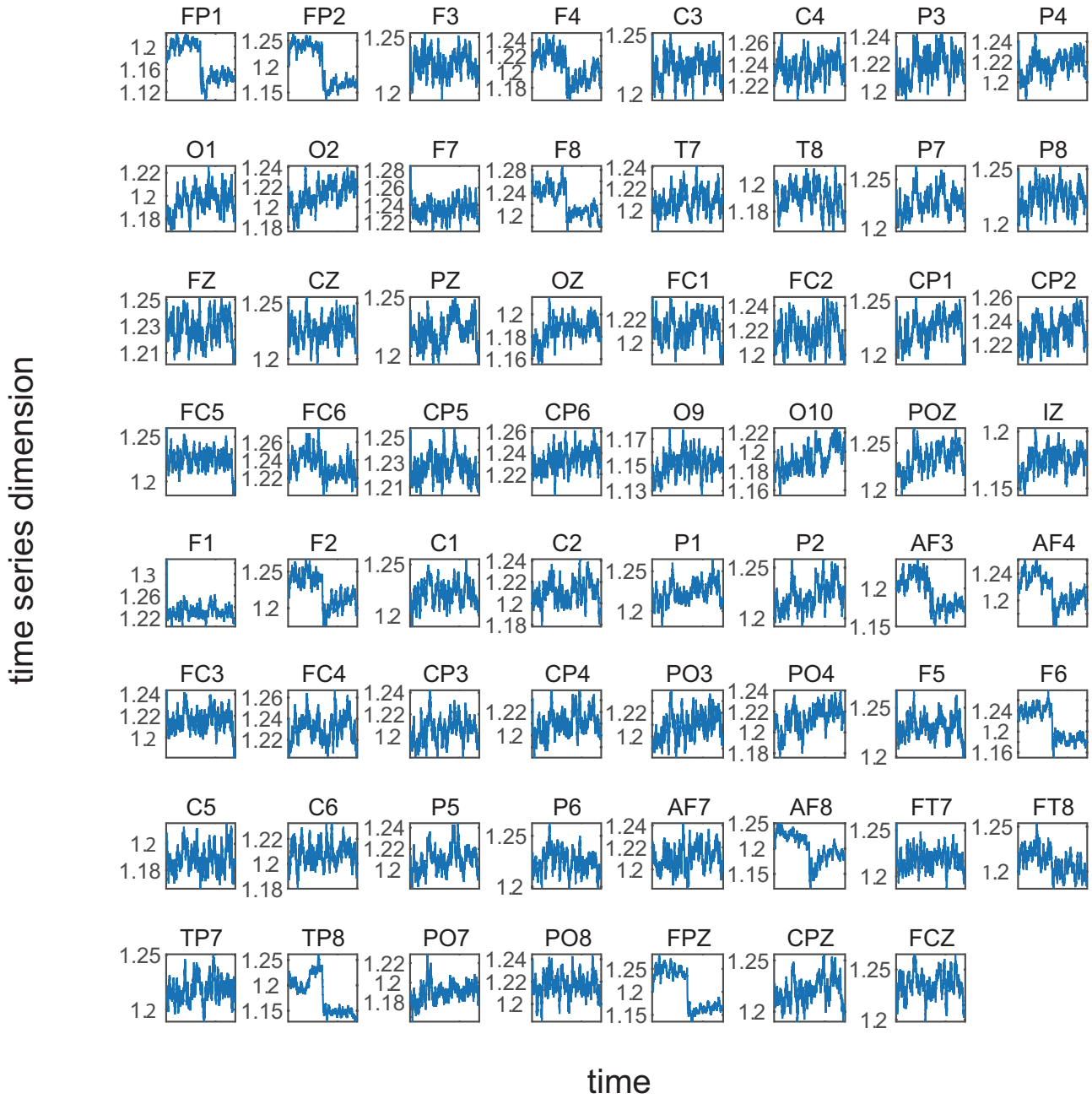

Figure D.5. TSD time series converted from EEG data obtained from 63 channels during trial 4. The notation of the time axis is the same with Fig. D.2.

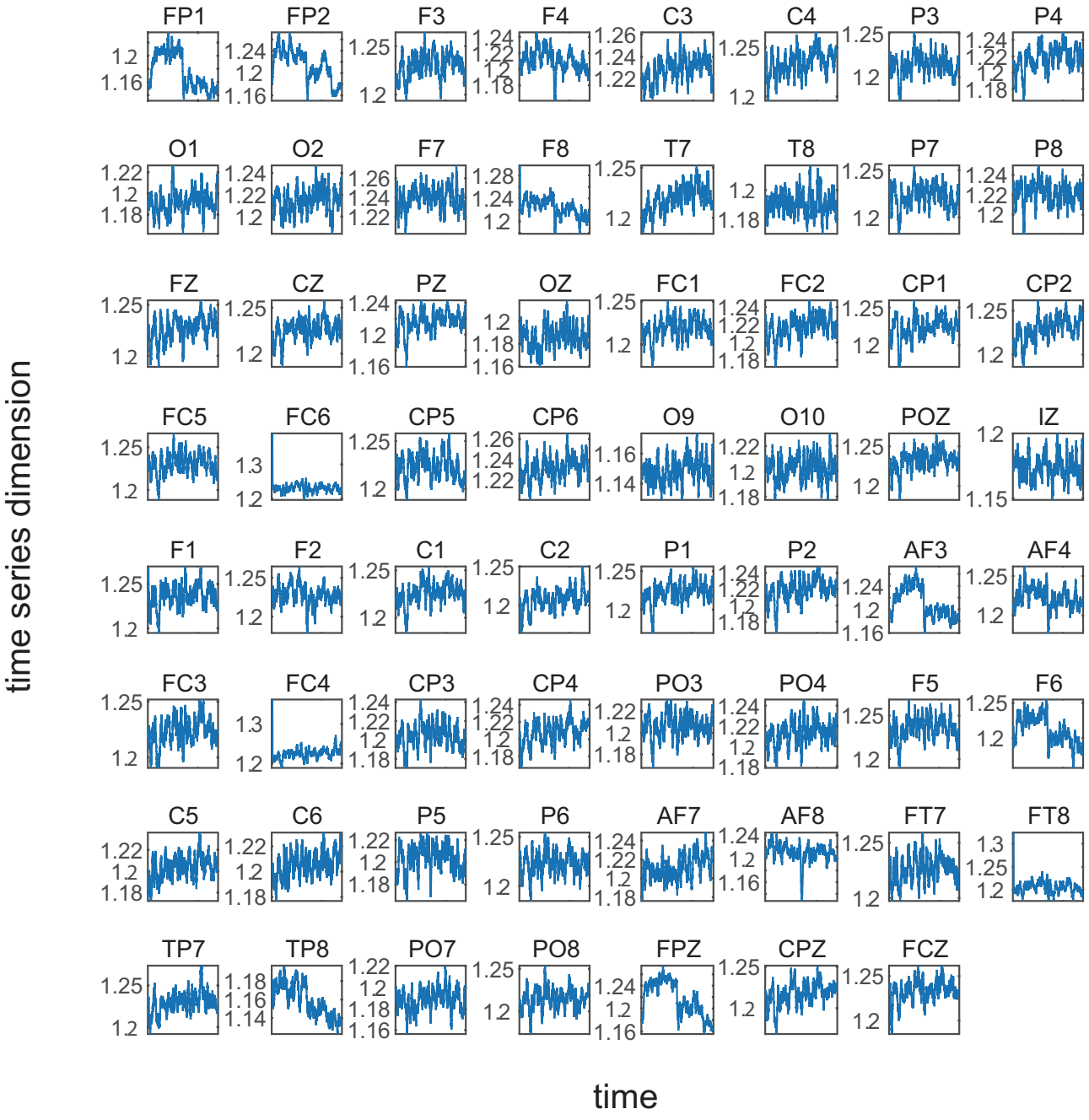

Figure D.6. TSD time series converted from EEG data obtained from 63 channels during trial 5. The notation of the time axis is the same with Fig. D.2.

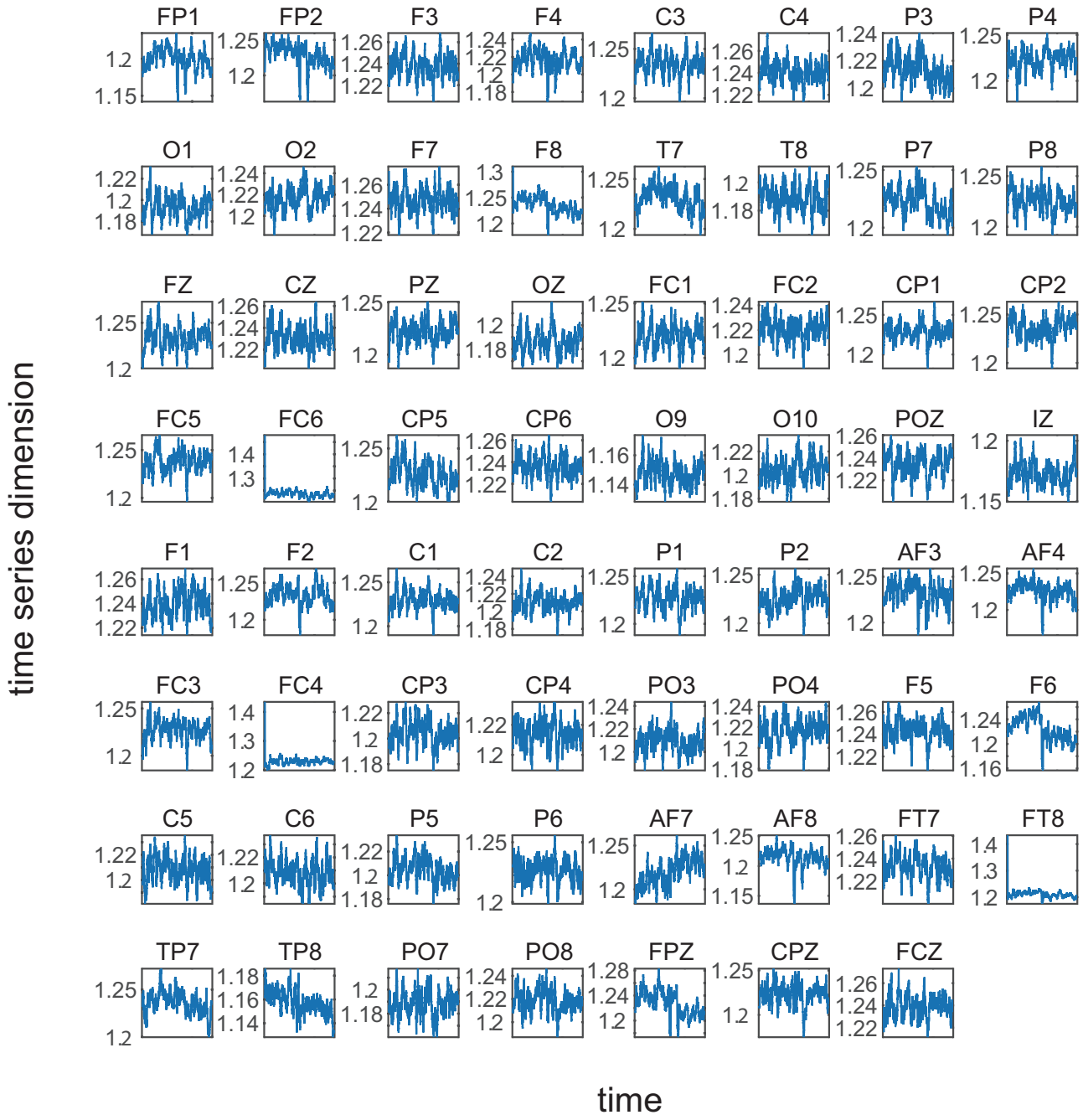

Figure D.7. TSD time series converted from EEG data obtained from 63 channels during trial 6. The notation of the time axis is the same with Fig. D.2.

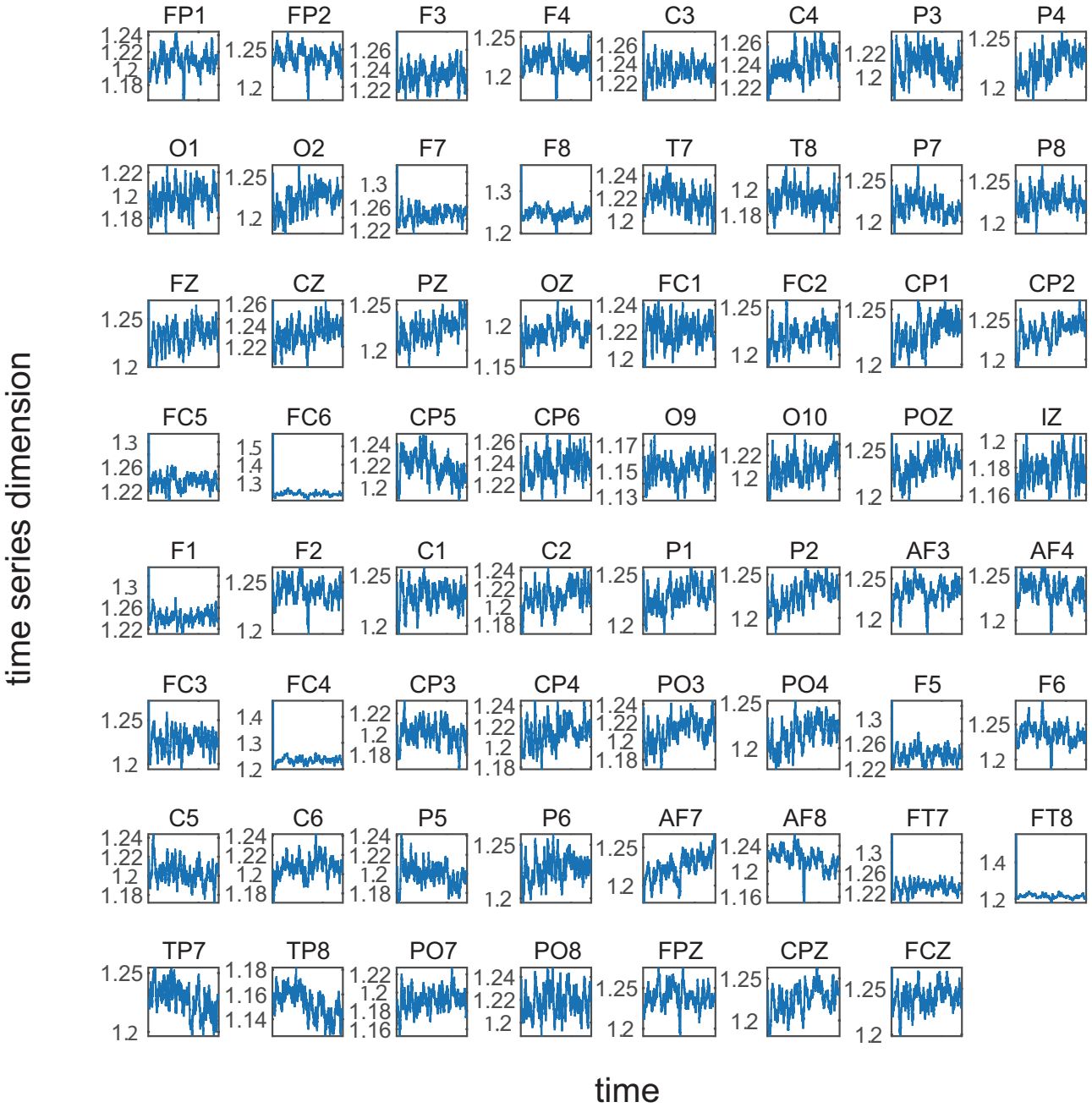

Figure D.8. TSD time series converted from EEG data obtained from 63 channels during trial 7. The notation of the time axis is the same with Fig. D.2.

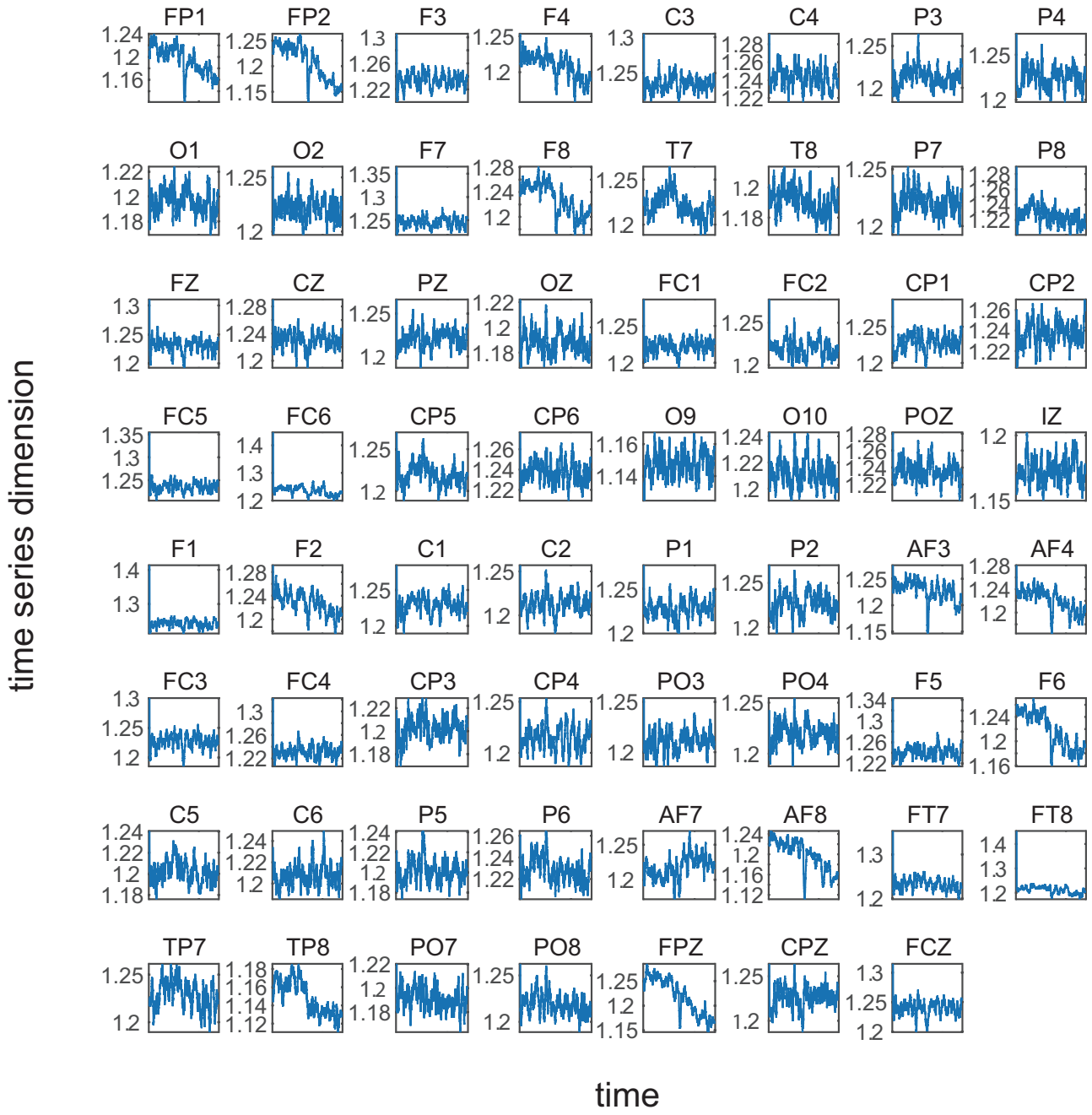

Figure D.9. TSD time series converted from EEG data obtained from 63 channels during trial 8. The notation of the time axis is the same with Fig. D.2.

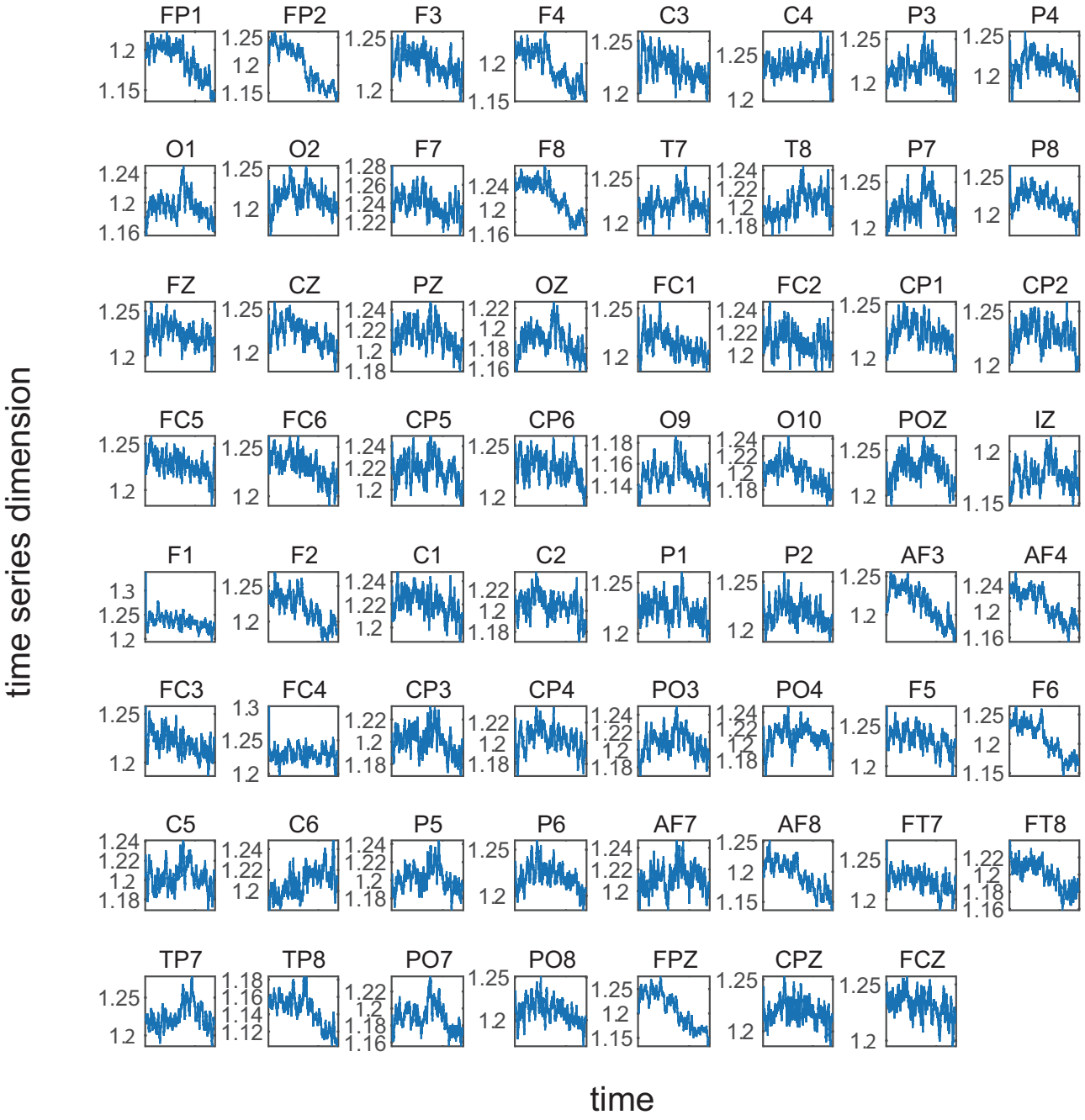

Figure D.10. TSD time series converted from EEG data obtained from 63 channels during trial 9. The notation of the time axis is the same with Fig. D.2.

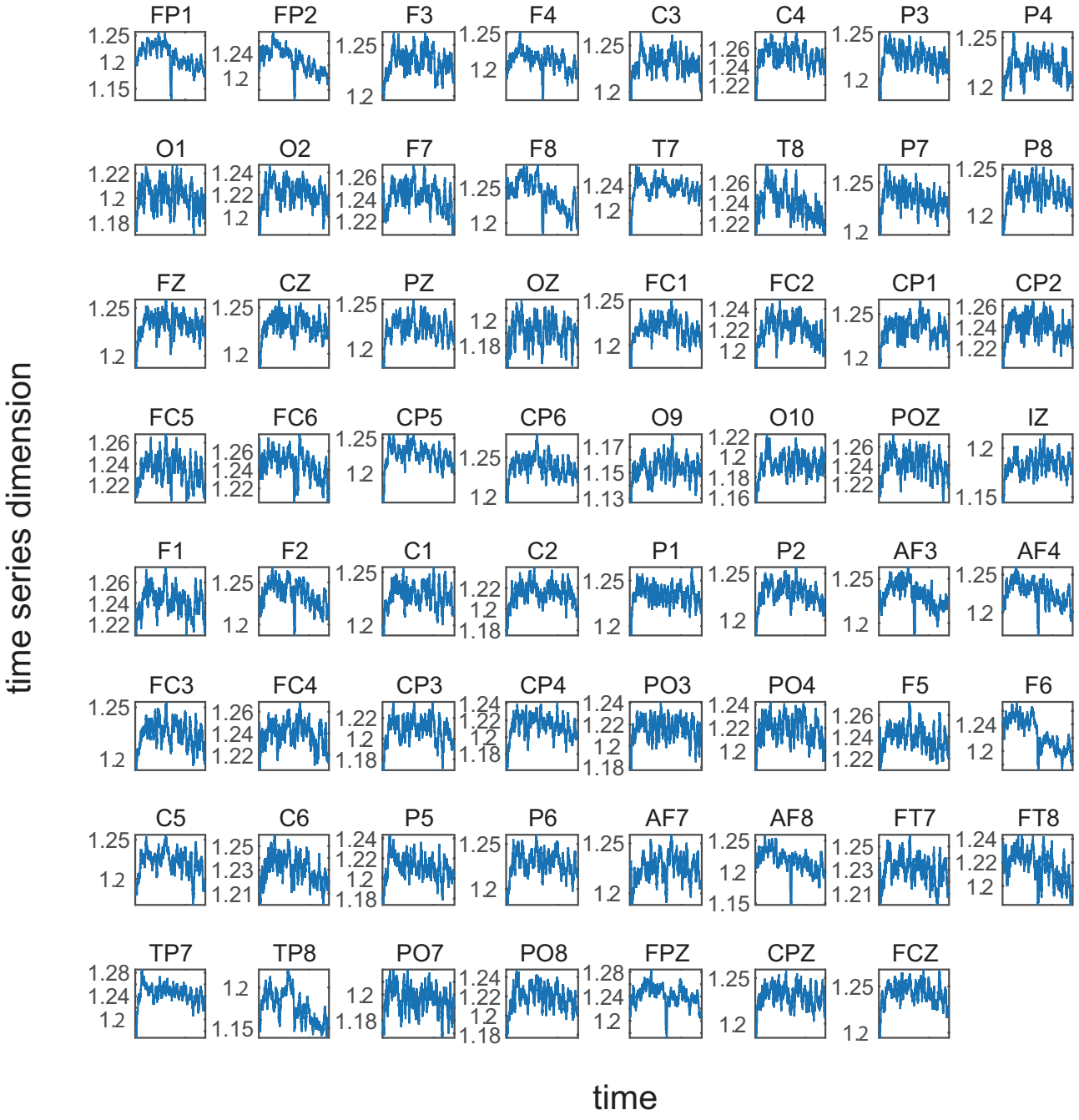

Figure D.11. TSD time series converted from EEG data obtained from 63 channels during trial 10. The notation of the time axis is the same with Fig. D.2.

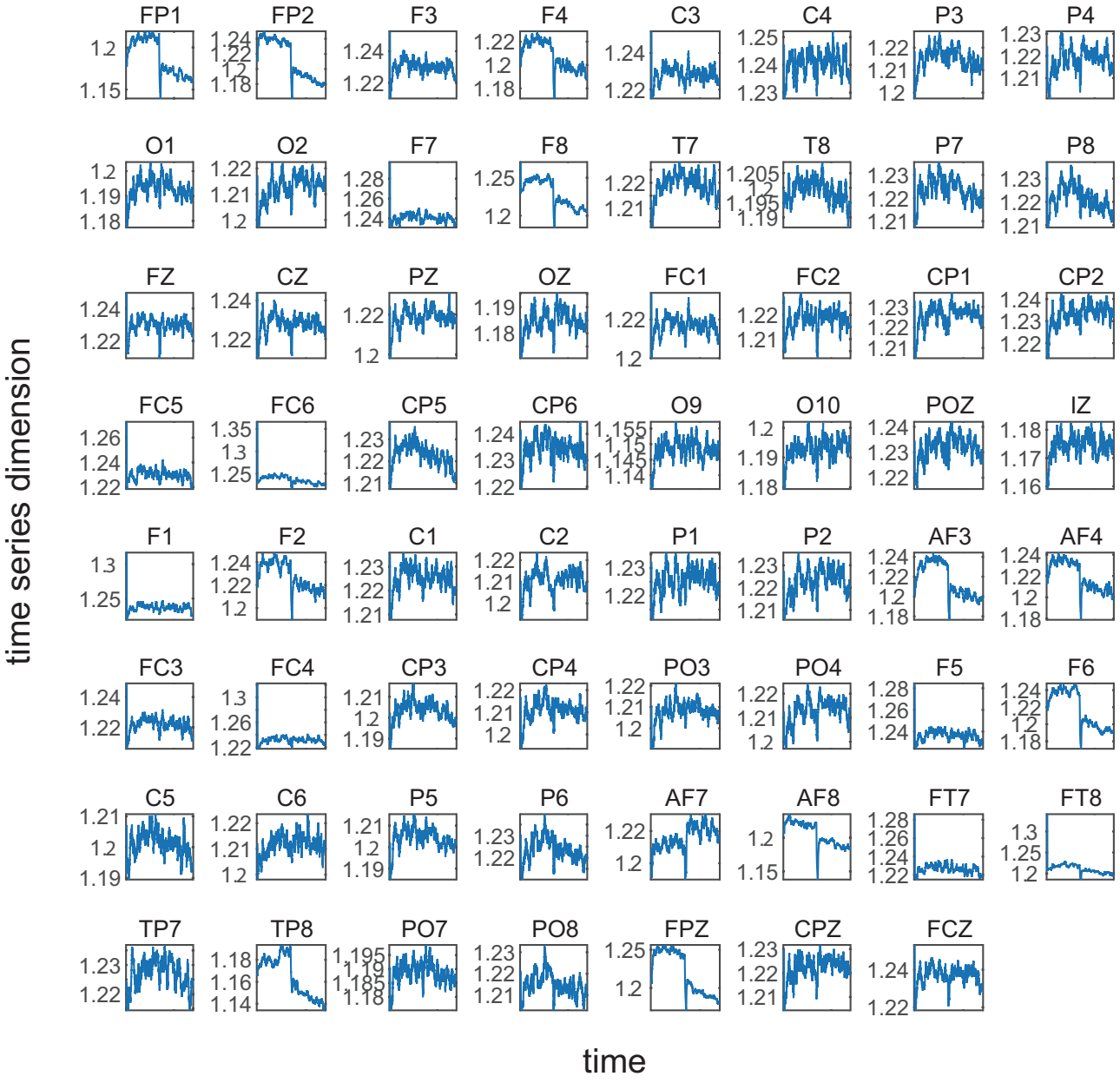

Figure D.12. TSD time series averaged over 10 trials depicted in Figs. D.2 to D.11 with respect to each channel. The notation of the time axis is the same with Fig. D.2.

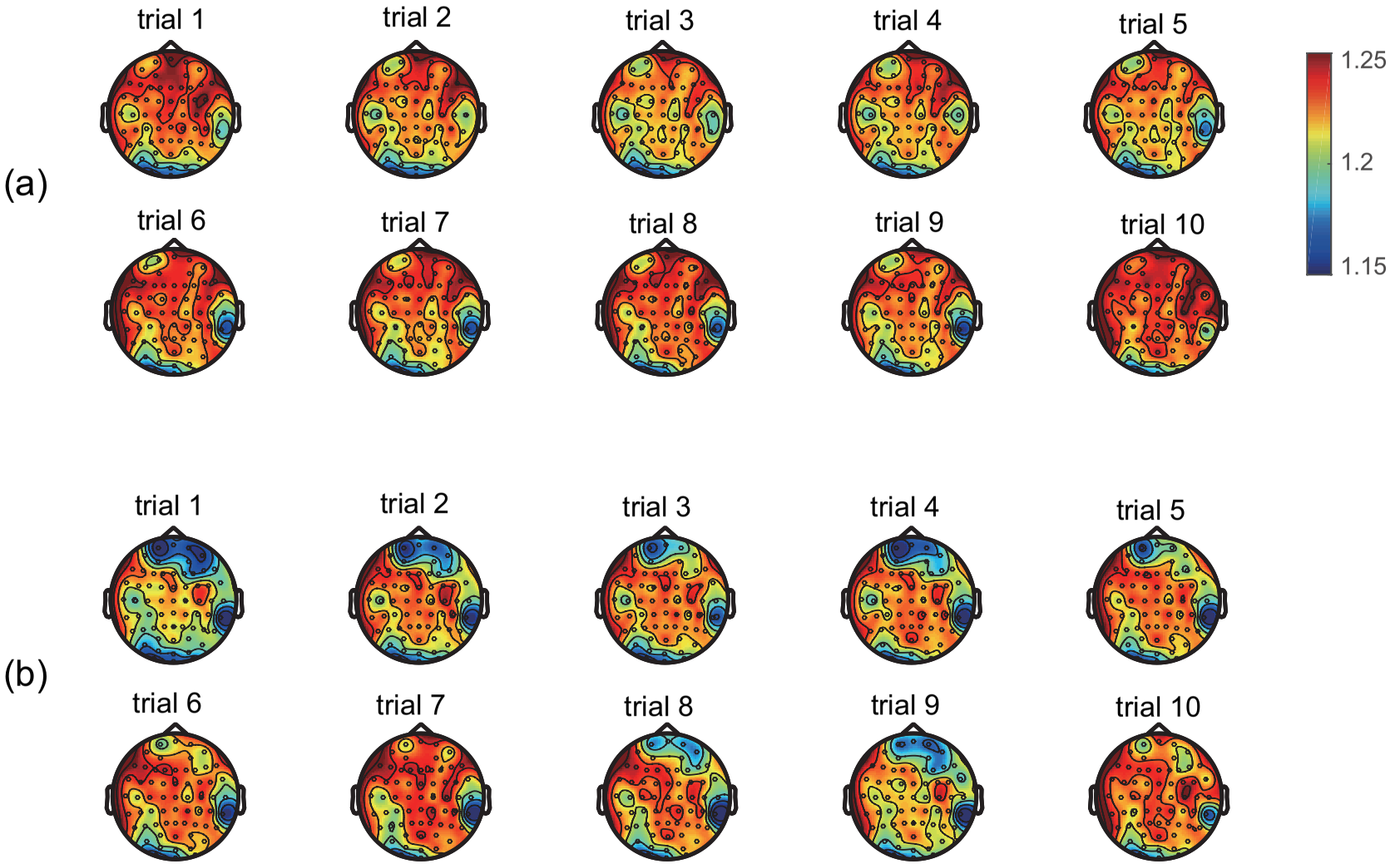

Figure D.13. Two-dimensional topographic maps among 10 trials on the human brain of subject 1, where the color indicates TSD values ranged from 1.15 to 1.25. TSD values plotted on each map denote averages over TSDs calculated from the eyes-open period (0 to 35 s) for (a) or from the eyes-closed period (35 to 70 s) for (b).

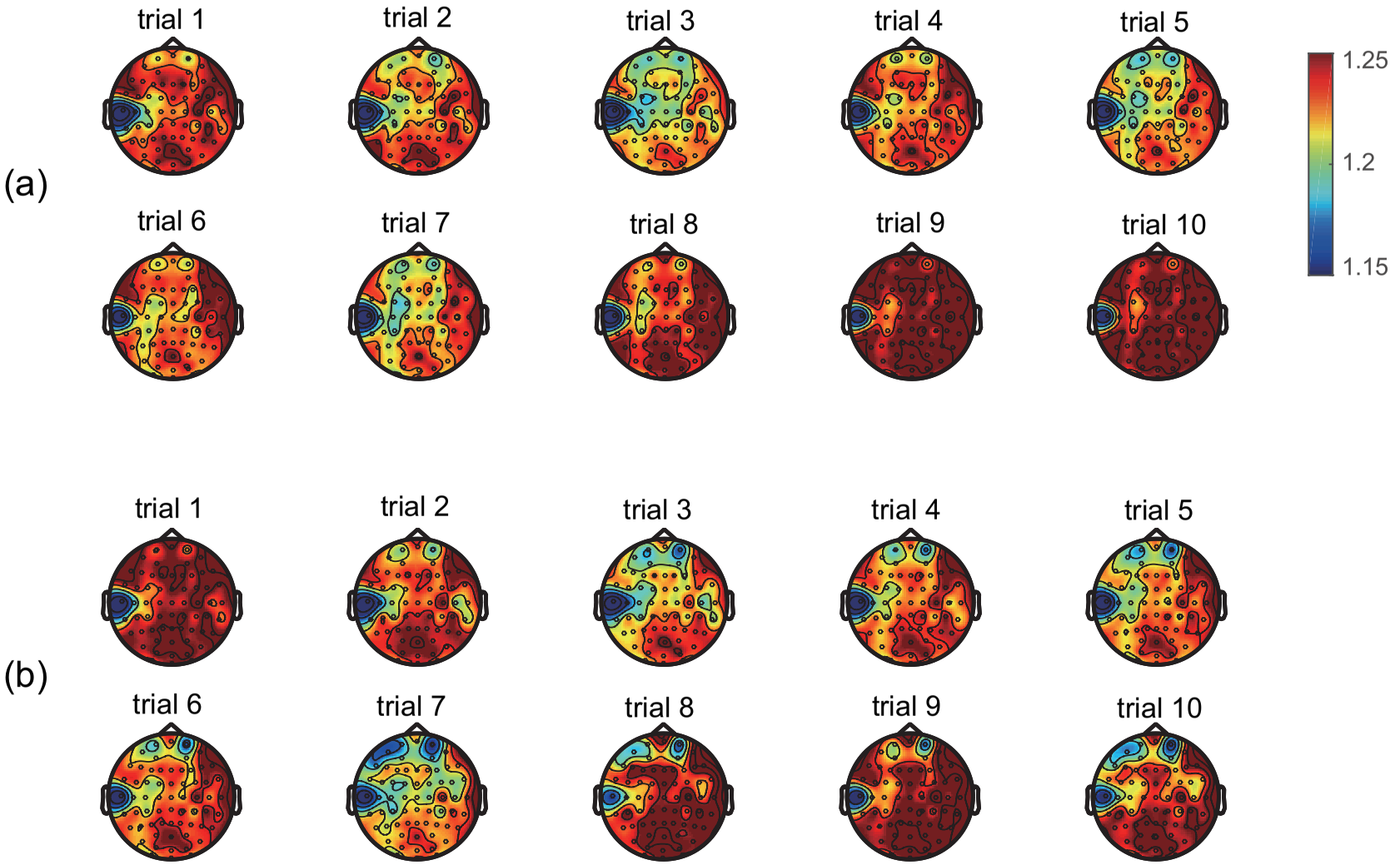

Figure D.14. Two-dimensional topographic maps among 10 trials on the human brain of subject 2, where the color indicates TSD values ranged from 1.15 to 1.25. TSD values plotted on each map denote averages over TSDs calculated from the eyes-open period (0 to 35 s) for (a) or from the eyes-closed period (35 to 70 s) for (b).

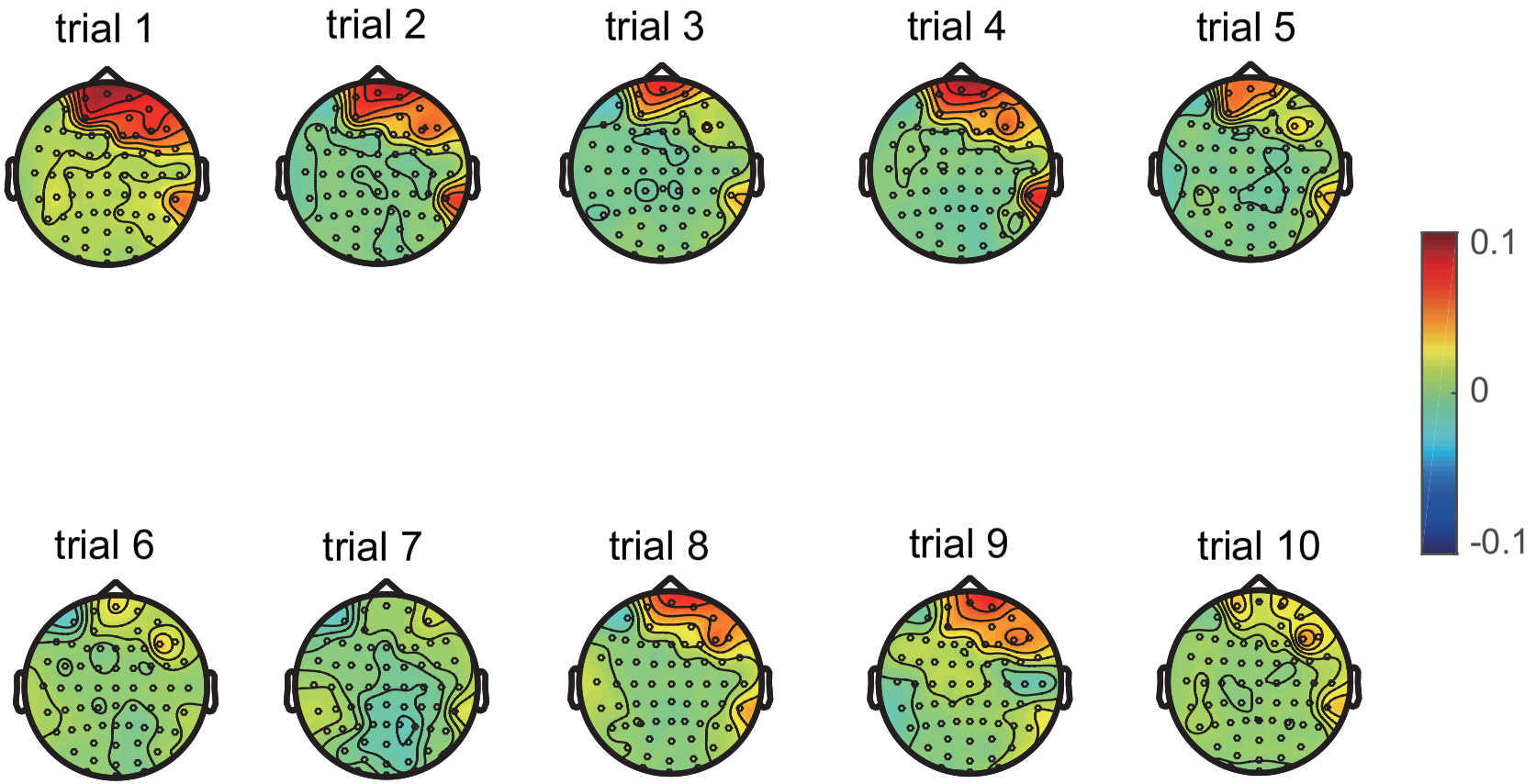

Figure D.15. Two-dimensional topographic maps among 10 trials on the human brain of subject 1, where each map reflects the difference between TSD values calculated from the eyes-open period and those calculated from the eyes-closed period.

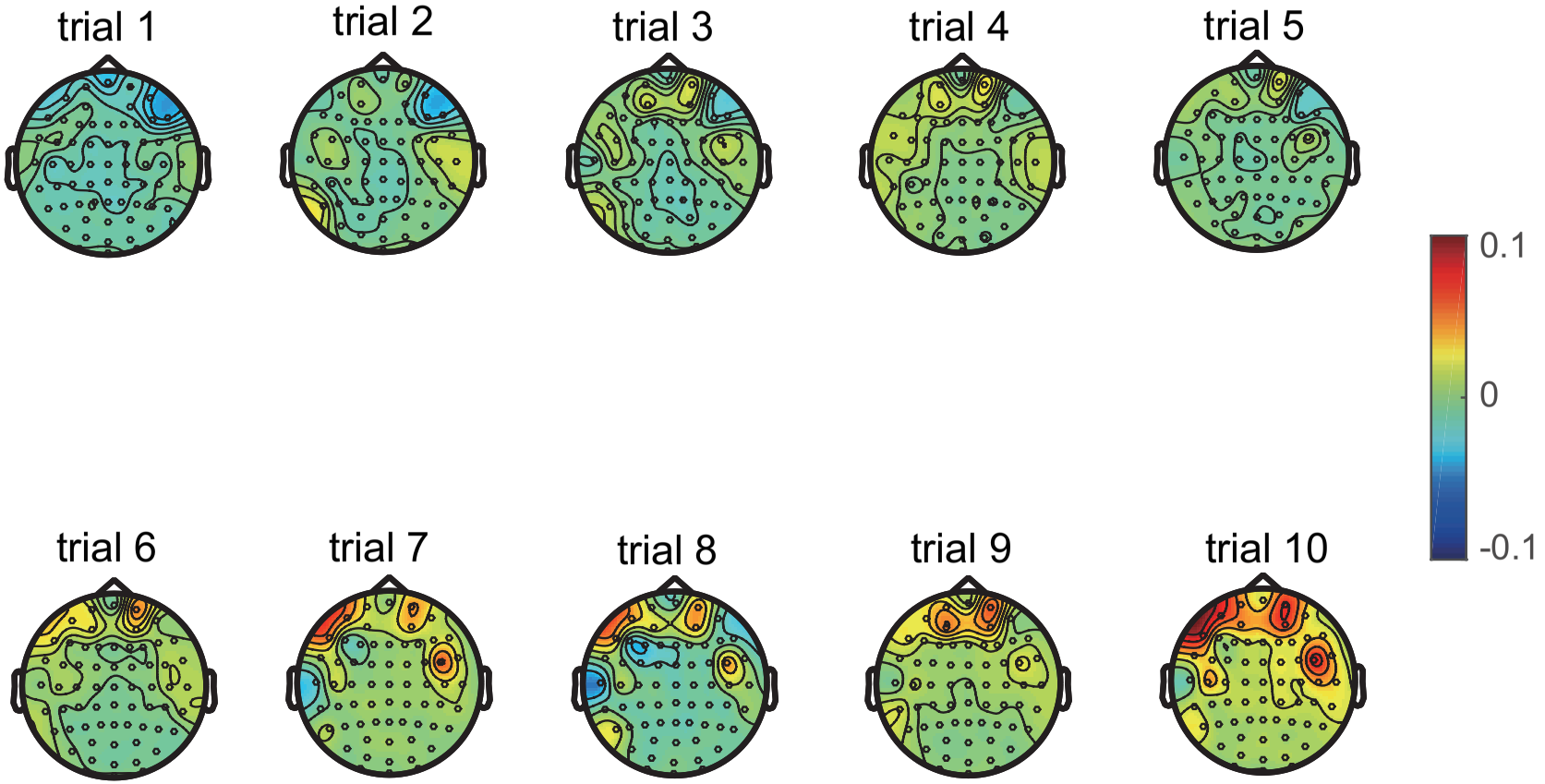

Figure D.16. Two-dimensional topographic maps among 10 trials on the human brain of subject 2, where each map reflects the difference between TSD values calculated from the eyes-open period and those calculated from the eyes-closed period.

Appendix E

Overviews of phase-amplitude cross-frequency coupling phenomena

In this appendix, attractors generating phase-amplitude cross-frequency coupling phenomena are shown in detail. In particular, two regimes, called oscillatory state with two frequency components in two-dimensional torus (OS2T) and that with two frequency components in closed curve (OS2C) are depicted, where these states appear on an eight-dimensional discrete-time stochastic neural network model with dynamic synapses [Eqs. (3.1) to (3.5)], via the uniform connections [Eq. (3.21) and Eq. (3.22)] within the excitatory/inhibitory network and between the excitatory and inhibitory networks. First, projections of such two kinds of 8-dimensional attractors on the two-dimensional planes, among all pairs of variables, are shown [see Figs. E.1 and E.2], where these attractors can be observed as the forms of a 2-dimensional torus in a map (MT2) and a one-dimensional torus in a map (MT1), respectively, and the attractors actually appear on a discrete-time dynamical system converted from the original stochastic model by use of the mean field approximation. Next, the time courses of variable $m_0^{\mathrm{I}}(t)$, reflecting the specific feature of cross-frequency coupling phenomena, are shown [see Fig E.3], for both cases of the OT2T and OS2C states, where the values of parameter J_0^{IE}, separating between the OS2T and OS2C states, were determined so as to make such two states approach the bifurcation point, called cyclic saddle-node bifurcation of 1-dimensional torus in map (MT1SNC).

By observing all the 2-dimensional projections, we can clearly understand which variables contribute to generating the MT2 [Fig. E.1] or MT1 [Fig. E.2]. Regarding projections of the MT2, it has been revealed that variables $m_0^{\mathrm{I}}(t)$, $X_0^{\mathrm{I}}(t)$, $U_0^{\mathrm{I}}(t)$, and $A_0^{\mathrm{I}}(t)$, building the inhibitory subnetwork (I), are associated with the generation of the MT2, because each projection composed of such variables is filled with a trajectory, whereas other projections composed of variables building the excitatory subnetwork (E) only show closed curves. As well as projections of the MT2, those of the MT1, especially associated with subnetwork I, show the closed curves undergoing the effect of the MT1SNC bifurcation on the MT2 so that the property of the closed curves was qualitatively different from that of the general closed curve. In addition, other projections of the MT1, associated with subnetwork E,

show a very similar trajectory with those of the MT2, and thus it has been clarified that subnetwork I strongly connects to the generation of cross-frequency coupling phenomena, but note that the interaction between subnetworks E and I is also essential to generate the MT2 and MT1.

To make the OS2T and OS2C states approach the MT1SNC bifurcation, the bisection method was used, and accordingly a set of the values $J_0^{\mathrm{IE}} = 3.1$ and $J_0^{\mathrm{IE}} = 3.2$ corresponding to the MT2 and MT1, respectively, tells us the difference between the OS2T and OS2C states clearly [Fig. E.3], where these values were actually chosen on the way to convergence of the bisection method, because the purpose here is to understand the effect of the MT1SNC bifurcation on the cross-frequency coupling phenomena in detail, not to search the bifurcation point.

By observing the two regimes of $m_0^{\mathrm{I}}(t)$ reflecting cross-frequency coupling phenomena [see Fig. E.3], we can assess how the information coding is performed within oscillatory time courses. First, it has been found clearly that both the OS2T and OS2C states include slow and fast oscillatory components; this suggests that cross-frequency coupling phenomena can encode two kinds of information simultaneously as a single oscillation. Next, it has been revealed that there exists a qualitative difference between the OS2T and OS2C states, that is, whether the same oscillatory phenomenon appears repeatedly in a specific phase of the slow oscillatory component; this suggests that the choice between the two states is adaptively conducted depending on the complexity of information to be transferred, in order that the bran encodes information effectively, where relatively simpler information will be transferred on the OS2C state, otherwise on the OT2T state.

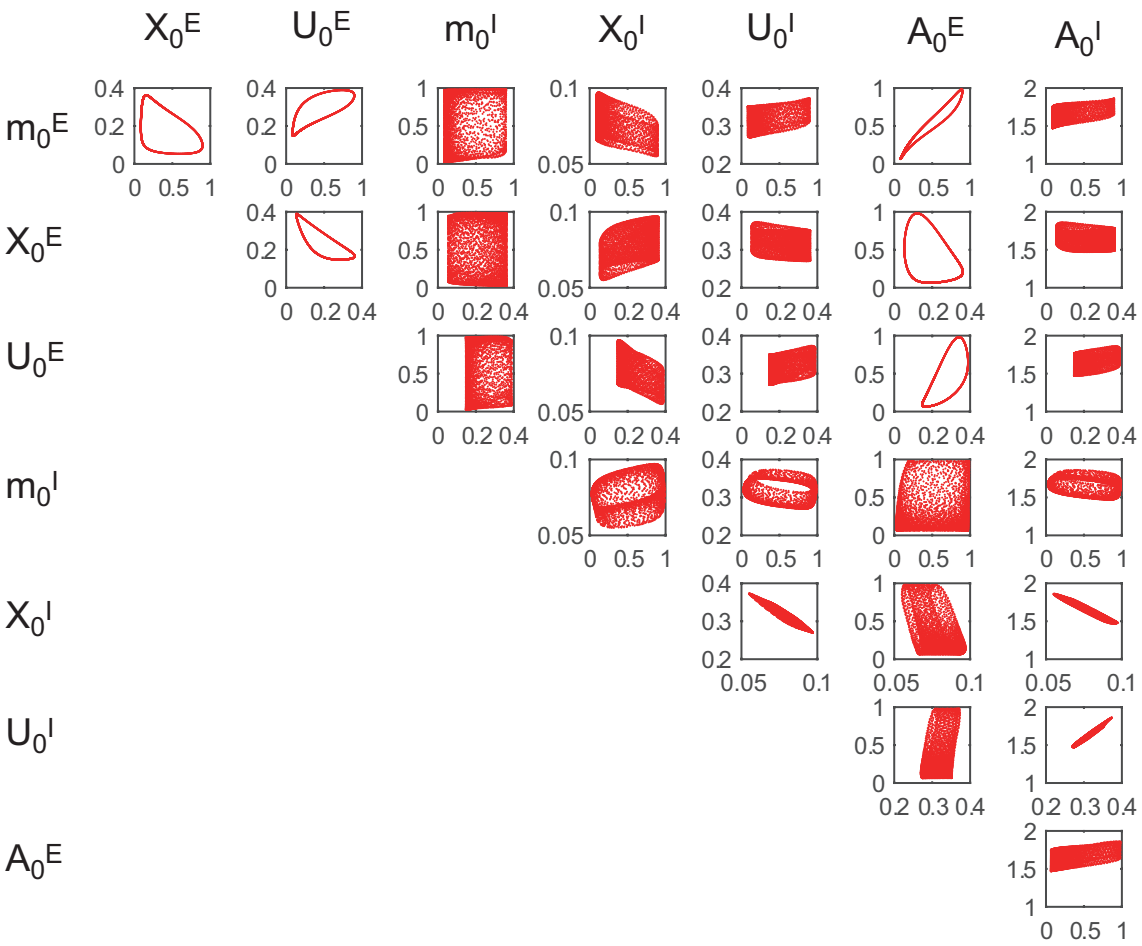

Figure E.1. Projections of an eight-dimensional neural network model generating the OS2T state on two-dimensional planes, among all the pairs of variables.

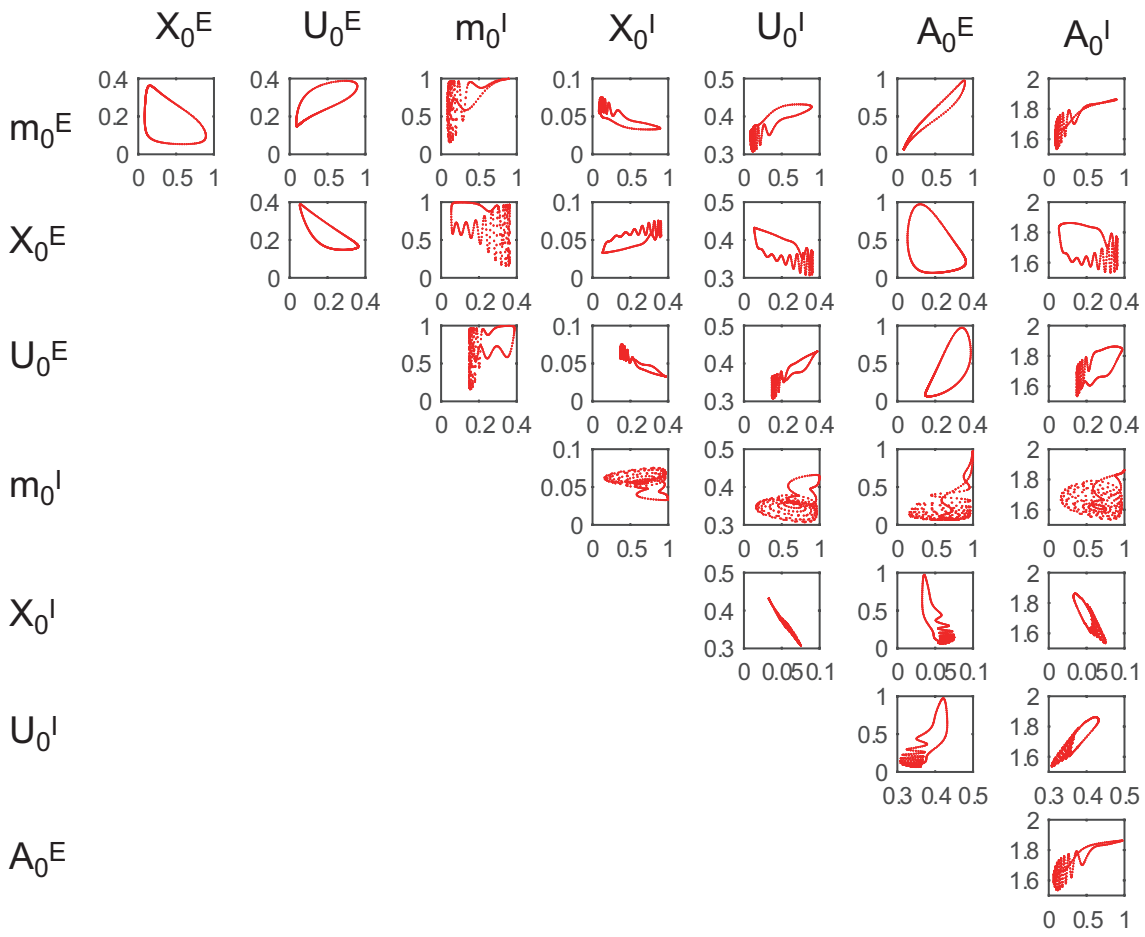

Figure E.2. Projections of an eight-dimensional neural network model generating the OS2C state on two-dimensional planes, among all the pairs of variables.

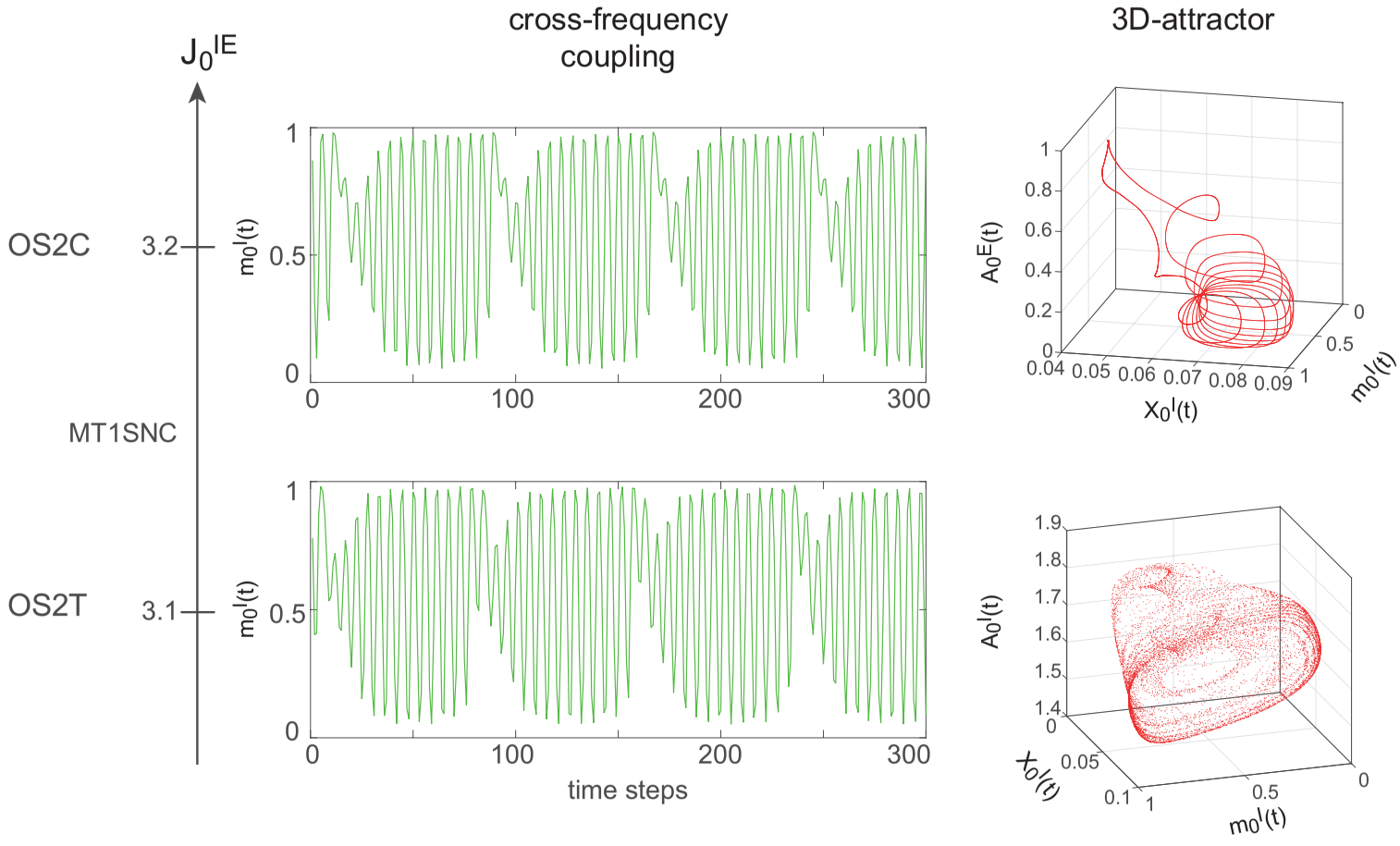

Figure E.3. A qualitative difference between the OS2T and OS2C states forming phase-amplitude cross-frequency coupling phenomena. The difference based on the time course $m_0^{\mathrm{I}}(t)$ is whether a specific phase of the oscillation is repeated or not, while that based on the state space is whether the attractor is the MT1 or MT2. Thus, Information coding would differ between the OS2T and OS2C states separated by the MT1SNC bifurcation.